6. Weather and Climate

Temperature, humidity, wind, and precipitation are the most commonly measured meteorological parameters. Collectively, they are what most of us think of when we refer to climate. By monitoring them at Emerald Lake, comparisons can be made to other alpine watersheds where data may be available. Meteorological measurements in alpine locations are sparse [Barry and Van Wie, 1974], thus such comparisons can be only general in nature. More importantly, by monitoring meteorological parameters at several locations in the watershed, spatial similarities and variations can be evaluated that will allow understanding of the distribution of meteorological and energy transfer parameters.

TABLE 6.1: Micro-Meteorological Instrument Sites in Emerald Lake Watershed

Site	Elevation (m)	Location UTM, Zone 11	Location Geodetic
1. Tower	2802	4,051,460 N 350,165 E	36°35′55″ N 118°40′30″ W
2. Inlet	2813	4,051,250 N 350,250 E	36°35′48″ N 118°40′27″ W
3. Pond	2962	4,050,975 N 350,520 E	36°35′39″ N 118°40′16″ W
4. Ridge	3085	4,051,325 N 350,830 E	36°35′51″ N 118°40′03″ W

Micro-meteorological monitoring in the Emerald Lake watershed is probably the most detailed in any alpine watershed in North America. Four sites are located on the topographic map presented in the previous chapter. Table 6.1 gives the elevation and coordinates of each site. Air temperature was monitored continuously at all four sites, humidity at the tower, inlet and ridge, wind speed at the inlet and the ridge, and snow and soil temperature at the inlet, pond and ridge during the 1986 snow season. The measurements were usually recorded at a time interval of 15 minutes, and were based on the average of 3 to 12 30-second samples. They were processed and integrated to one hour averages, at a consistent time step so that all sites and parameters could easily be compared.

Snow surface temperature, snow depth, and snow density were measured manually at regular intervals at several sites in the watershed. Snowfall was measured on snowboards at two or more sites, as soon after a deposition event as possible. Snow water equivalent (SWE) and temperature profiles were measured in monthly snow pits at several locations throughout the snow season. Less detailed surveys of SWE were made at a hundred or more sites four time during spring melt. All of these data were carefully evaluated to determine their reliability under a variety of conditions, relying on duplication of some measurements to help eliminate bad or spurious values. Particular care is given to data collected during snowmelt and runoff. The data presented represent our best estimate of each parameter.

Climatic conditions and local micro-climatic variation control the timing and magnitude of meltwater generation over the watershed. Snowmelt is initiated when the snowcover receives more energy than it loses over a period of time. Initially energy is utilized to increase the temperature of the snowcover to the melting temperature (0.0°C). Once this has been achieved additional input of energy will cause melt. Variations in measured meteorological parameters over time can be used to indicate when and at what rate energy transfer and melt will occur. This is a complicated process requiring not only detailed meteorological data, but information on the physical and thermal properties of the snowcover. Because these data are seldom available, most efforts to predict snowmelt and runoff have been based on the use of one or more easily measured meteorological parameters as an index to snowmelt that can be used to develop a regression against measured streamflow.

One of the first descriptions of this approach was presented by Horton [1915] who suggested that air temperature could be used as an index to the overall climate and therefore snowmelt. Collins [1934] defined the "degree-day" as a 24–hour period during which the average air temperature is 1.0°C above the melting temperature of ice (0.0 °C), and suggested that this parameter could be used as an index to overall energy exchange and snowmelt. Early investigations of the mechanisms and thermodynamics of snowmelt by Church [1941] and Wilson [1941b] recognized the complexity of the process, but recommended the statistical index approach for predicting snowmelt because of the difficulty in acquiring data for more deterministic methods. Light and Kohler [1943] developed and tested a statistical approach for forecasting seasonal snowmelt runoff using snow depth measured at selected sites as the index, and Linsley [1943] presented a method for forecasting daily snowmelt runoff using air temperature as the index. These early studies formed the foundation for virtually all of today's operational snowmelt runoff forecasting efforts. Anderson and Crawford [1964] showed that this type of model could be adapted to run on a digital computer, and the work of Anderson [1973] and Burnash et al. [1973] followed, defining operational snowmelt runoff forecasting for the most of the U.S. These models or variations on them are still in use today, as seen in the work of Tangborn [1980]. The most promising advancement was presented by Martinec [1975] who included spatial information on snow covered area (SCA) from satellite remote sensing data in the model regression equation. This technique was further tested by Rango and Martinec [1979]. Martinec [1980] conceded that there were limitations to using SCA in a temperature-index snowmelt model, but concluded that because it provided information on the depletion of snow volume from a drainage basin it was an improvement over air temperature alone [Martinec, 1982], and that it could also be used to estimate snow accumulation rates [Martinec, 1984] and depletion rates [Rango and Martinec, 1982].

All of these models are based on the premise that because climate and energy exchange could not be monitored adequately, a physically based snowmelt runoff model was not possible. More easily measured indices had to be established, and because the relationship between these indices and snowmelt runoff was statistical rather than physical, the consistency of the data was much more important than the absolute accuracy or precision. Rango and Martinec [1979] showed that remote sensing data could enhance the utility of meteorological data in a snowmelt model, and that such models could, under some circumstances, provide an acceptable level of accuracy for snowmelt runoff forecasting [Rango and Martinec, 1981]. A comparison of operational snowmelt models from around the world by the World Meteorological Organization found that inclusion of remote sensing data improved accuracy in most cases [WMO, 1975, 1982], and Martinec [1985] found the same when comparing several models in use in the western U.S. The use of remote sensing data is limited by their coarse resolution [Rango et al., 1983], cost, and, to a certain extent, limited availability for some remote areas. Rango and Martinec [1986] point out, however, for most remote areas the limitation is not remote sensing data, but the lack of air temperature data.

Miller [1950] showed that air temperature was a good index to snowmelt in environments where solar radiation and wind were not the significant factors in energy transfer (for example in forested areas), a finding which excluded most of the alpine snow zone. The U. S. Army Corps of Engineers, in their volume Snow Hydrology [USACE, 1956], suggested that in the high-elevation, open snow zone the most accurate way to forecast snowmelt was to monitor climate and energy transfer. At that time, however, they did not feel that this was possible at a remote site. In an alpine watershed, deterministic or energy-balance snowmelt models can provided better results, but climate data are difficult to acquire. Both Charbonneau et al. [1981] and Rango and Martinec [1986] stress the need for improved climate monitoring in alpine areas.

This chapter presents a detailed discussion of our efforts to monitor climate at just such a site. Climatic variables were monitored at several locations in the Emerald Lake watershed during the 1986 snow season. For these data to be used comparatively, an evaluation of noise and errors was made. To use them to calculate energy exchange at the snow surface over a watershed requires an understanding of the uncertainty of measured parameters at a point, that can be taken into account when extrapolating point measurements over the watershed.

Even the most common meteorological parameters are difficult to measure continuously at a remote site, because both the instrumentation and recording equipment exhibit varying degrees of instability depending on conditions. At a remote alpine site, it is not possible to attend instrumentation at more than weekly intervals during most of the year, and during winter safety considerations may increase this interval to several weeks. Instruments or recording systems did fail on several occasions during the 1986 snow season. Four instrument sites were maintained, so that multiple measurements of critical parameters would be made. These data have been synthesized into a continuous record of all parameters at two representative sites: the ridge and a lake site. Missing data were synthesized from a combination of the current diurnal pattern, from nearby measurements of the same parameter, and from manually made field measurements. Data records began on November 1, 1985 and continue for either the duration of snowcover, August 1, 1986, or September 30, 1986, depending on which was most appropriate.

Data processing or adjustments that alter the magnitudes of the raw data are discussed in detail in the following sections. Careful attention has been paid to both the precision and accuracy of these data, but their absolute uncertainty is not known at this time. A number of investigators have evaluated the inherent uncertainty in similar instrumentation and recording systems [Anderson, 1976; Marks et al., 1986] but the absolute uncertainty cannot be known without conducting specific experiments, probably in a laboratory.

6.1. Data Recording and Instrumentation

Meteorological data were recorded on the EzLogger recording system manufactured by OmniData, Inc. This system was selected because it provided the flexibility to manage and process data from different types of instruments at multiple locations in the watershed. The system was made up of modular, programmable field units that were light-weight (≈1kg), and could be easily transported to a remote site. Recording was on solid state EPROM's (erasable, programmable, read-only memory) that were stable during the variations of temperature and humidity found at an alpine site like Emerald Lake. The system had minimal power requirements, 8 D-Cell batteries for approximately 6 weeks of operation. The field units could be programmed to convert the raw voltage output to meteorological units so that field technicians could easily evaluate instrument performance. Recorded data could be transferred directly to a computer reducing, but not eliminating, data processing time.

The EzLogger data recorder is a 12-bit system with 12 analog, 2 event counter, 1 frequency input channels, and 4 digital input/output channels. The analog channels could be assigned 5V, 1V, 100mV, or 10mV full-scale range, independent of sign. This allowed the recording of both negative and positive input voltages on the same channel, but reduced the sensitivity of these channels to 11-bits, or 0.05% of full-scale. This was adequate for all meteorological instrumentation. One constant excitation voltage (5V) and one variable excitation voltage (0-10V) could be assigned to any of the analog input channels. Analog channels could be sampled at 1, 5, 15, 30 minute, and 1 hour intervals, with options of averaging, totalizing, or recording the maximum and minimum readings. Sample time varied from 1 to 10 seconds, depending on how the channel was defined. Data could be recorded at the same intervals as sampling, but was usually done at a multiple of the sample intervals. The sampling interval selected was constant for the frequency and all analog channels. Up to five data-recording intervals could be selected for the 15 channels.

The event counter channels were used for tipping-buckets connected to snowmelt lysimeters and totalizing anemometers, the frequency channel for anemometers. Both of these channels accumulate counts during an interval defined by the data-recording interval. The frequency channel can also sample the frequency for a fixed interval and average these over the data-recording period.

The number of channels used, sampling frequency, voltage excitation requirements, and data-recording frequency determined the rates of battery power and data storage consumption. The system performed well with one exception. Data loss occurred in the presence of a strong static charge that is common in high-elevation environments. During these conditions, several records could be lost. To combat this all channels were set to a 5-minute sampling interval, and a 15-minute recording interval. This effectively solved the problem, but resulted in very large data rates and more frequent battery and EPROM changes, and complicated the data processing. The recorded data of all analog channels represent the average of three samples of over a 15-minute period. Data from the totalizing channel represent the total number of "events" (tips or revolutions of the anemometer) that occurred during the 15-minute period. Data from the frequency channel can represent the average frequency over the 15-minute period, or the total number of revolutions during the recording period.

Meteorological instrumentation had to be robust, have low power requirements, and be compatible with the data-recording system described above. All instrumentation was duplicated at least once in the watershed to insure data redundancy, and to improve our understanding of parameter uncertainty and spatial variance. Table 6.2 presents the characteristics of the instrument types and models used in this study. An estimate is also made of the recorded data quality as affected by the data-recording system, the limitations of the type of instrument used. The "noise equivalent change" $NE\Delta$ is the magnitude of parameter change required to cause a change in the recorded data. Linearity reflects instrument characteristics, and is based on the precision of the function used to convert instrument voltage to parameter units. Precision of the recorded data is estimated from the combined effects of $NE\Delta$, linearity, and instrument stability. In general, $NE\Delta$ should be substantially smaller than linearity, and estimated precision will be larger than linearity. $NE\Delta$ is computed from the full-scale range of the channel, converted to parameter units. Linearity and precision were computed for the mean parameter value during the snow season.

Incident solar radiation was measured by Precision Spectral Pyranometers, and incident thermal radiation by Pyrgeometers manufactured by The Eppley Laboratory, Inc. These instruments were re-calibrated by the National Bureau of Standards just prior to the 1986 snow season. The pyranometers have a cosine response within ±1% from 0–70° from nadir. The pyrgeometers have a perfect cosine response from a diffusing source like the atmosphere. The global solar pyranometers (285–2800nm) measured irradiance in excess of $1200\,Wm^{-2}$ at times. This produced an output voltage that exceeded 10mV by 1 to 3 mV, forcing the use of the 100mV range on the data recorder. The reduced sensitivity of the larger full-scale range resulted in the large $NE\Delta$ value for these data. Data linearity and precision are also affected, but not to such a great extent.

Air temperature probes were designed and constructed using thermistors manufactured by Yellow Springs Instruments, Inc. These thermistors were individually tested and calibrated to a temperature range more typical of the southern Sierra Nevada, improving both the linearity and the precision of temperature data from them. The broad calibration range of the Vaisala and Physchem sensors resulted in lower precision of the data recorded. The Weathertronics Hygro-Thermograph was used as a back-up for the digitally recorded air temperature and humidity instrumentation, but data from this instrument were not used in the analysis.

Most of the recorded air temperature data were of acceptable quality during windy or low sun periods. During calm conditions, however, radiation shielding was a problem for all instruments. A fabricated radiation shield made of four 10cm square aluminum plates, painted with highly reflective white paint, proved to be inadequate in the thin atmosphere and high radiant intensities common in a high-altitude environment. Under calm conditions radiant heating or cooling of the sensor would occur. A mechanically aspirated radiation shield would have solved the problem, but the required power could not have been supplied. A radiation shield manufactured by Met One (Model 071/5290) was self aspirating, and corrected the problem in all but the most calm conditions.

Humidity measurements were problematic during most of the 1986 snow season. Of the variety of instruments used, most were ineffective. The General Eastern dew point sensor is a precision laboratory instrument designed to measure the condensation temperature on a cooled mirror. While this is the most accurate and direct method of humidity measurement, this instrument was not robust enough for field use and required far more electrical power than could be supplied even with solar panels. The General Eastern instrument was operated in a heated building several km from and 600 m below the watershed during the latter part of the 1986 water year. These data were not used in the analysis.

The Physchem sensor estimated the relative humidity of the air by the change in resistance in a LiCl cell. This instrument was not designed for operation during the dry, cold conditions which are common in an alpine watershed. The precision of the instrument was poor at low humidity (<300 Pa) and once the LiCl cell was saturated with water or ice (common during blowing snow-deposition events) it could not be re-calibrated in the field. Very few data from this instrument were of useful quality. The Vaisala instrument was much more robust, was reliable across the full range of humidities, and did not suffer the calibration and hysterisis problems associated with the Physchem sensor. Data from this instrument were of acceptable quality, but were not available until mid-July, 1986. As for air temperature, the Weathertronics Hygro-Thermograph is included in Table 6.2 only to put the precision of the other instruments in perspective. The poor precision of this instrument was unacceptable.

While air temperature does not directly affect the estimate of relative humidity by the instruments discussed above, the quality of the air temperature are critical in the calculation of vapor pressure from relative humidity:

$$e_a = e_{a,sat} \times \frac{RH}{100} \tag{14}$$

where:

e_a = vapor pressure of the air (Pa),
$e_{a,sat}$ = saturation vapor pressure at T_a (Pa),
RH = relative humidity.

Over- or under-estimates of T_a will affect the calculation of e_a. Proper radiation shielding is essential for measuring both air temperature and humidity.

Soil and snow temperature probes were designed and constructed using the Yellow Springs thermistors. These sensors were also individually calibrated over a narrow range of temperatures, to improve data linearity and precision. The thermistors were potted in thermal epoxy (Delta Bond 152) in the center of a machined 2 cm copper rod (1 cm diameter). The copper sensor protruded from a sealed PVC case that enclosed the electrical connections. This design minimized thermal conduction along the wires and case, and ensured thermal contact with the sensor and the soil or snow. Data from snow temperature sensors was used only when sufficient snowcover existed to eliminate solar heating.

Problems with wind measurement occurred because the instrument used did not match the data-recording system. The Met One anemometer was a low-threshold totalizing instrument, with lexan cups designed to eliminate riming. When connected to the event counter channel, it was limited to a maximum count of 99,999. Initially, with the sampling interval was set to 15 minutes, the maximum recordable wind speed was just over 9 m s^{-1}. By reducing the sampling interval to 5 minutes, this maximum was increased to just over 27 m s^{-1}, but even this limit was surpassed during wind events. The frequency channel was also used to sample the frequency of this wind sensor and average these samples over the recording period. This further improved the range of the sensor, but not the precision of the data. The R. M. Young instrument eliminated most of this problem by allowing utilization of an analog channel on the data recorder. This allowed sampling and averaging of the current generated by the sensor.

6.2. Air Temperature

The most common meteorological data collected anywhere are of air temperature. Figure 6.1 shows daily mean and daily maximum and minimum air temperature from November, 1985, through September, 1986, at the ridge and lake sites. Ideally these measurements should be made at a specified height above the snow surface, shielded from the effects of radiation or conduction from sources other than the atmosphere. In practice, this is seldom the case. Some radiant heating or cooling of the instrument shelter is inevitable, but in most locations this produces only a minor effect. At an alpine site, such as Emerald Lake, the atmosphere is thin (70 kPa or less), with low turbidity, and solar insolation is very high. During the day, the temperature of the sensor can be higher than that of the air. On clear nights, incident thermal radiation will be small, and radiant cooling can lower the temperature of the sensor below that of the air. The best passive radiation shields available will fail under these conditions. The problem is exacerbated during the day because of the high reflectivity of the snow and surrounding terrain, causing the air temperature sensor to receive solar energy from all sides. These effects are difficult to detect in the data, as they show up only as temperature extremes. This problem is maximized when wind speeds are low and mixing of the air is small. A solution would be to mechanically aspirate the temperature sensors, but this consumes power and is not possible at most remote sites. Careful evaluation of both wind and air temperature allows us to note those times when a problem may have occurred, but we cannot know the magnitude of the measurement error without another independent measurement at the same time.

Figure 6.2 illustrates the problem, showing the correspondence of extreme high and low temperatures with low wind speeds. While it is difficult to isolate the effects of radiation, it is clear from this figure that both extreme high and low temperatures occurred during periods of light winds. Comparison of daily maxima and minima with data from other alpine sites in the Sierra Nevada and with spot measurements made in the watershed showed that the range of continuously measured daily air temperature was unrealistically large. Spot measurements of air temperature made during the snow season with a sling psychrometer never exceeded 15°C. To reduce the amplitude of the diurnal variation of air temperature, the raw data were smoothed with a power function of their absolute differences from 0.0°C:

$$T_a = \mid T_{a,raw} \mid^{n_{Ta}} \times \mathrm{sign}(T_{a,raw}) \tag{15}$$

where:

T_a = smoothed air temperature (°C),
$T_{a,raw}$ = measured air temperature (°C),
n_{Ta} = air temperature smoothing exponent (0.92).

The value 0.92 was used for the exponent n_{Ta} because it best fit spot measurements. This function brings larger magnitude temperatures down to a more realistic value, (either positive or negative) but has little effect on temperatures closer to 0.0°C. This approach is effective, but not ideal. It is hoped that in future years better radiation shields will eliminate or substantially reduce this problem.

Fortunately for energy exchange calculations, this problem does not cause significant errors, because at low wind speeds turbulent energy exchanges are also minimized, as will be discussed in a following chapter. The success of temperature-index snowmelt models at forested or protected sites is due to both the correlation of measured air temperature and radiant energy flux, and the fact that most measurements of air temperature are affected by the intensity of radiant flux at low wind speeds.

Snow surface temperature is difficult to measure mechanically [Davis and Marks, 1980; Davis et al., 1984]. Though more accurate, radiative temperature measurement requires complicated instrumentation, and the hygrometric method developed by Andreas [1986] requires frequent adjustment of the instrumentation. Neither of these methods can be used at this time for continuous monitoring at a remote site. Although we made numerous spot measurements of surface temperature, it usually must be estimated from other more easily measured meteorologic parameters. Work at the

Mammoth Mt. snow study plot [Davis et al., 1984] shows that the snow surface temperature tends to follow the air temperature. This occurs because the insulating characteristics of the snowcover allow the surface layer to come into temperature equilibrium with the atmosphere even though this may create large temperature differences between the surface and lower layers. Snow has a very low thermal conductivity $K_{s,l}$ ($\approx 0.01\,\mathrm{J\,m^{-1}\,K^{-1}\,s^{-1}}$) and is therefore a good insulator [Yen, 1965]. $K_{s,l}$ will vary with snow density ρ_s, and will increase if diffusion is taken into account [Anderson, 1976], but it will always be small. Bilello et al. [1970] got similar results for data from the upper 10 cm of the snowcover at Ft. Greely, Alaska.

Estimating snow surface temperature in the Sierra Nevada is aided by the fact that both snow and air temperatures are relatively warm. Snow surface temperatures were approximated as a function of the difference between the current air temperature and the surface temperature (measured or calculated) at the last time step:

$$T_{s(i)} = T_{s(i-1)} + (T_{a(i)} - T_{s(i-1)})\,a_{T_s} \tag{16}$$

where:

- T_s = snow surface temperature (°C or K),
- T_a = air temperature (°C or K),
- i = time index (usually 1 hour),
- a_{T_s} = snow surface temperature change factor (0.1).

Snow surface temperature is constrained to be ≤ 0.0°C, and once air temperatures remain above this temperature for any length of time, the snow surface temperature becomes constant. The value 0.1 was used for the snow surface temperature change factor a_{T_s} because that produced a result that approximated measured values. Figure 6.3 shows daily mean calculated snow surface temperatures for the 1986 snow season at the ridge and lake sites. This figure is a damped expression of the air temperature at these sites (Equation 16) constrained to be 0.0°C or less. While some cold temperatures are predicted in the early winter, by February – when most of the snowfall occurred – surface temperatures are only slightly below 0.0°C, fluctuating diurnally. By early April, they are constant at that temperature at both sites. Measured values from snowpits fit reasonably well with these calculated values for periods from February on.

Table 6.3 summarizes air and surface temperature at the ridge and lake sites for the 1986 snow season. Monthly average temperatures have little physical significance, but they allow us to evaluate longer-term variation of a parameter which is subject to so much stochastic short-term variation that it can be difficult to see differences between the sites. As indicated in Figures 6.1 and 6.3, and shown clearly in Table 6.3, the ridge is cooler than the lake site and has a larger diurnal variation. December was the coldest month at the ridge. While February was coldest at the lake, it differed little from the other winter months. At both sites, April was the month when the diurnal amplitude was maximized, which is expected as this is usually the month when net energy exchange begins the transition from negative to positive. It is noteworthy that the large diurnal amplitude occurred only in April and May at the ridge site, but began in March and persisted until June at the lake site.

Monthly differences between the sites indicate a large negative lapse rate in winter, decreasing in spring. By May the lapse rate appears to be inverted. The large winter lapse rate is probably caused by radiant cooling at night, and the inverted lapse rate in spring by solar heating of the air temperature sensor at the ridge. The yearly averages have even less physical significance than monthly averages, but they summarize the differences between the sites for the 1986 snow season, and give probably the best estimate of annual temperature lapse rates. If a standard temperature lapse rate of $-6.5\,\mathrm{K\,km^{-1}}$ were applied to the 275 m difference in the elevation of the two sites, a difference of −1.65K would be expected. The annual difference shown in the table would suggest that a standard lapse rate is too large for this site, and that a lapse rate of $-4.0\,\mathrm{K\,km^{-1}}$ would be more appropriate.

6.3. Humidity

Humidity, or the water vapor content of the air, is another commonly measured meteorological parameter monitored in the Emerald Lake watershed. This parameter is more difficult to monitor than air temperature, as it cannot be measured directly outside the laboratory. Many techniques are used to estimate humidity, but the most common are by changes in the flexibility of a hair, or filament, or changes in the electrical capacitance or conductance of a porous medium of a composition that has a known electrical response to changes in moisture content (e.g. LiCl). These methods usually estimate the relative humidity, or the ratio of the actual water vapor concentration to the saturation concentration at that temperature. A much more accurate method to measure humidity is to directly measure the dew point or condensation temperature of the air by cooling or heating a surface until condensation occurs. Unfortunately, this requires more power than is likely to be available at a remote site, as both heating and cooling and mechanical aspiration of the sensor are required.

Several methods of monitoring humidity have been used at Emerald Lake. A condensation mirror-type dew point sensor was installed near the lake with a solar power system in fall of 1985, but this instrument consumed too much power and its circuitry was too sensitive to fluctuating temperature conditions to be operated in this environment. It was replaced with a hair hygrometer and several capacitance-type relative humidity sensors. The hygrometer is poorly adapted to operation in an alpine environment, because of the very dry conditions and large diurnal temperature fluctuations. It has a slow response and recovery time, is not adaptable to automated data collection, and gives unreliable results during winter conditions.

The capacitance-type instruments offer the best chance for continuously monitoring humidity at a remote site. These sensors are also affected by the radiant heating and cooling, though to a lesser degree than is air temperature. More critical is the fact that most sensors are not calibrated for conditions found at dry, cold alpine sites. The sensors used, selected because of their low power requirements, were found to be sensitive to ambient temperatures around the triple-point of water (0.0°C), when frost could form on the sensor, and to temperatures lower than −15°C. They frequently produced unrealistic diurnal fluctuations in the recorded humidity data. Comparing these data to measurements made on a very accurate condensation mirror device at another instrumented site at Mammoth Mt. [Davis and Marks, 1980; Davis et al., 1984] convinced us that many of the values recorded at Emerald Lake were not correct.

Figure 6.4 shows the daily mean, and the daily maximum and minimum vapor pressure for the ridge and lake sites sites for the 1986 snow season. These data are from a combination of measured and calculated humidities. Estimated humidities are calculated from thermal radiation, which is more easily measured than humidity. The calculation is based on the assumption that thermal radiation under clear skies is a function of the vapor pressure and air temperature [Brunt, 1932; Brutsaert, 1975]. Treating the atmosphere as a grey body, the thermal irradiance at a point is:

$$I_{lw} = \varepsilon_a \, \sigma \, T_a^{\,4} \tag{17}$$

where:

I_{lw} = thermal irradiance ($\mathrm{Wm^{-2}}$),
ε_a = atmospheric emissivity,
σ = Stefan-Boltzmann constant (5.6697×10^{-8} $\mathrm{Wm^{-2}K^{-4}}$),
T_a = air temperature (K).

If I_{lw} and T_a are measured, atmospheric emissivity is:

$$\varepsilon_a = \frac{I_{lw}}{\sigma T_a^{\,4}} \tag{18}$$

Brutsaert [1975] showed that near sea level, atmospheric emissivity could be related to near surface vapor pressure e_a (in mb), and the absolute air temperature by:

$$\varepsilon_a = 1.24 \left[\frac{e_a}{T_a} \right]^{1/7} \tag{19}$$

where the coefficients 1.24 and 1/7 were empirically derived. Marks and Dozier [1979] showed that this could be extended to mountainous terrain by assuming a standard temperature lapse rate to estimate a sea level air temperature T_0, a constant relative humidity to estimate a sea level humidity e_0, and the relative atmospheric thickness A_{th}, at the point in question:

$$A_{th} = \frac{P_a}{P_0} \tag{20}$$

$$\varepsilon_a = \left\{ 1.24 \left[\frac{e_0}{T_0} \right]^{1/7} \right\} A_{th} \tag{21}$$

where P_0 and P_a are air pressure at sea level and point in question.

This equation can be inverted, solving for sea level vapor pressure e_0, relative humidity RH, and near surface vapor pressure e_a:

$$e_0 = \left[\frac{\varepsilon_a}{A_{th}\, 1.24} \right]^7 T_0 \tag{22}$$

$$RH = \frac{e_0}{e_{0,sat}} \tag{23}$$

$$e_a = RH \; e_{a,sat} \tag{24}$$

where $e_{0,sat}$ and $e_{a,sat}$ are saturation vapor pressure at T_0 and T_a.

Assuming that measured air temperatures were reliable, and that clear skies tended to persist during times when measured humidity were missing or unreliable, this approach was used to estimate vapor pressure. It gives some low vapor pressures at times, but in general produces a diurnal range and a daily mean which are consistent with measured dew point temperatures at similar sites in the Sierra Nevada. It will tend to over- or under-estimate vapor pressures during wind-free periods when the measured air temperature is incorrect, and will over-predict vapor pressure during cloudy periods. It is, however, the most reliable estimate of vapor pressure during much of the 1986 snow season at Emerald Lake.

Because the snow is made up of ice, water, and air, it is assumed the air fraction is always saturated, and that the snow surface vapor pressure is the saturation vapor pressure at the snow surface temperature. Snow surface vapor pressure is constrained to be less than or equal to the saturation vapor pressure at 0.0°C (610.71 Pa). Periods of saturation of the air occur either during very cold periods, when saturation is difficult to detect, or during precipitation events. Periods of condensation (when the vapor pressure of the air exceeded the vapor pressure at the snow surface) are infrequent at either site, but occur more often at the ridge than at the lake, because the snow surface there is more exposed to radiant cooling. Figure 6.5 presents the hourly surface vapor pressure gradient ($e_a - e_s$) for the ridge and lake sites for the period of November to September, 1986. The infrequent positive values indicate condensation on the snow surface.

There is little difference between the atmospheric humidity traces at the ridge and lake sites, except during summer when the lake was ice free and relatively warm. At that time, humidity near the lake tended to be higher with a smaller diurnal variation than at the ridge. Table 6.4 presents a summary of humidity for the air and the snow surface for the 1986 snow season. Average monthly values for the daily mean, maximum, and minimum are shown for both sites. Again, long term averages have little physical meaning but can be used to show changes in time and between sites. It would appear that the ridge site is slightly less humid than the lake site, with a slightly smaller diurnal range. However, measurement or recording uncertainty is around 40 to 50 Pa, so these differences cannot be distinguished from measurement noise. These data suggest that there is no humidity difference between the sites, and that vapor pressure varied little over the watershed during most of the snow season.

6.4. Wind

Wind speed was routinely monitored at Emerald Lake. Wind direction was deemed so site-specific that it was decided that the effort to adequately monitor this parameter was beyond the scope of this project. Wind is highly variable in both time and space and is difficult to characterize by sampling in either of these dimensions. Some averaging or integration of the measurement is required in almost all cases. A totalizing anemometer, or a count of the number of turns of the anemometer during a specified time period, is a solution to the problem of temporal sampling that was initially applied at both sites with mixed results. Initially, at the ridge site, a recording interval of 1 hour was specified because of difficult access and limited recording capabilities. Wind speed was recorded as the average of four 15-minute totals utilizing an event-counter channel. Unfortunately, this channel was limited to a maximum recordable wind speed of $9.0\,\mathrm{m\,s^{-1}}$ during the 15-minute totalizing period, inadequate at either site. At the lake site, a 15-minute recording interval was used, because easier access would allow more frequent changing of the recording medium. At this site, wind speed was recorded as the average of three 5-minute totals, allowing a maximum recordable wind speed of $27.0\,\mathrm{m\,s^{-1}}$ during a 5-minute totalizing period. This proved adequate most of the time at the lake site.

The problem at the ridge site was realized in early December, 1985, and the ridge data recorder was moved to a recording and sampling interval similar to that at the lake site. By mid winter, however, the ridge site was regularly exceeding the maximum value of $27.0\,\mathrm{m\,s^{-1}}$. Limits of both the recording and data storage media prohibited a more frequent recording or averaging intervals. The only solution to the problem was to abandon the totalizing anemometers, and replace them with current generators. This allowed us to utilize frequency channels on the data recorder. The output from these channels was then sampled and averaged in a manner similar to the air temperature and humidity data. This change was implemented in early July at both sites.

Figure 6.6 presents the daily mean, and the daily maximum and minimum wind speed at the ridge and lake sites for the 1986 snow season at Emerald Lake. The problems with maxima at the ridge site are clearly shown, as are other changes to the recording and averaging during the year. While the absolute accuracy of these data is in question, it is clear that the ridge site receives more wind than does the lake site at all times of the year. These data represent the best estimate of wind speed at the two sites during the 1986 snow season.

Table 6.5 presents a summary of wind speed at both sites. In this case, longer term averages may be more meaningful than the shorter term data. Early season similarities between sites is an artifact of problems with the recording and averaging intervals discussed above. During most of the rest of the year, wind speed at the ridge site was nearly twice that at the lake site.

6.5. Snow and Soil Temperatures

Soil temperatures at 50 cm below the surface and temperature at the soil-snow interface were monitored at several sites in the Emerald Lake watershed. Snow temperature at 30 cm above the soil surface was monitored at the ridge site. Figure 6.7 presents daily averages of these data during the 1986 snow season for the lake and ridge sites. These data begin in early November, 1985, when the seasonal snowcover was first established. The end of the data set is arbitrary at both sites, as the instrumentation was excavated for maintenance once the snowcover was less than a meter in thickness. This was done because differential thermal properties between copper thermistor casings and the surrounding soil caused a melt induced cavity around the sensors, eliminating contact with the snow.

What is clear from Figure 6.7 is that temperature differences between the soil, the snow-soil interface, and the lower snowcover were very small during most of the 1986 snow season. During the spring melt season, these temperature gradients were essentially zero. At both the lake and ridge sites, the interface temperature went to 0.0°C by late November and remained there for the duration of the snow season. Soil temperature was slightly warmer at the lake site in the early winter, but by April, there was almost no difference between the sites. The warmer temperatures at the lake site was probably due to poorly drained, meadow type soils found there. The soil at the ridge site is well drained gravel and sand and can be expected to hold little or no water. The soil temperature at the lake site becomes 0.0°C in May, when the flushing of melt water at that temperature would be expected to dominate the soil temperature profile. This does not occur at the ridge site because better drainage would be expected to limit the effect of melt water on the soil temperature.

Snow temperature just above the snow/soil interface was monitored only at the ridge site. By late November, this temperature had stabilized to just less than −1.0°C and then slowly warmed to 0.0°C by mid-March. From that time on, there was effectively no temperature gradient between the snowcover and the interface and little or no gradient between the snowcover and the soil. It is reasonable to assume that this also occurred at the lake site. Because all indications are that the lake site was slightly warmer than the ridge site during the 1986 snow season, it might be expected that the early December snow temperature at the lake site was slightly warmer than at the ridge site, and the isothermal condition was reached sooner. While "isothermal" technically indicates only a uniform temperature, in snow hydrology it is generally used to indicate a uniform temperature at the melting point of ice. Snow pit data show that snow temperatures just above the soil interface were 1 to 2K colder at the lake site until late March. This effect is the result of reduced solar insolation during winter at the lake site and the insulating effects of a deep snowcover, allowing these lower temperatures to persist.

Though there are slight differences between the two sites during fall and winter, these are gone by early spring, and the sites are identical during snowmelt. This should be the case for the entire watershed. The thermal regimes of the soil and lower snowcover would be expected to be similar during melt everywhere in the watershed. Most of the difference between sites would be in the initiation of the isothermal condition.

6.6. References

Anderson, E. A., National Weather Service river forecast system-- snow accumulation and ablation model, *Tech. Mem.*

NWS HYDRO-17, 217 pp., NOAA, Silver Spring, MD, 1973.

Anderson, E. A., A point energy and mass balance model of a snow cover, *NWS Tech. Rep. 19*, 150 pp., NOAA, Washington, DC, 1976.

Anderson, E. A. and N. Crawford, The synthesis of continuous snowmelt runoff hydrographs on a digital computer, *Tech. Rep. 36*, 103 pp., Dept. Civil Engrg., Stanford Univ., Stanford, CA, 1964.

Andreas, E. L., A new method of measuring the snow-surface temperature, *Cold Regions Sci. Technol.*, *12*, 139-156, 1986.

Barry, R. G. and C. C. Van Wie, Topo- and microclimatology in alpine areas, in *Arctic and Alpine Environments*, edited by J. D. Ives and R. G. Barry, pp. 73-84, Methuen, London, 1974.

Bilello, M. A., R. E. Bates, and J. Riley, Physical characteristics of the snow cover, Ft. Greeley, Alaska, 1966-67, *Tech. Rep. 230*, U.S. Army Cold Regions Res. Engrg. Lab., Hanover, NH, 1970.

Brunt, D., Notes on radiation in the atmosphere, *J. Royal Meteorol. Soc.*, *58*, 389-420, 1932.

Brutsaert, W., On a derivable formula for long-wave radiation from clear skies, *Water Resour. Res.*, *11*, 742-744, 1975.

Burnash, R., R. Ferral, and R. McGuire, A generalized streamflow simulation system, *Tech. Rep.*, 204 pp., Joint Fed.-State River Forecase Ctr., Sacramento, CA, 1973.

Charbonneau, R., J. P. Lardeau, and C. Obled, Problems of modeling a high mountainous drainage basin with predominant snow yields, *Hydrol. Sci. Bulletin*, *26*, 345-361, 1981.

Church, J. E., The melting of snow, *Proc. Central Snow Conf.*, *1*, 21-32, 1941.

Collins, E. H., Relationship of degree-days above freezing to runoff, *Eos, Trans. Amer. Geophys. Union*, *15*, 624-629, 1934.

Davis, R. E., J. Dozier, and D. Marks, Micrometeorological measurements and instrumentation in support of remote sensing observations of an alpine snow cover, *Proc. Western Snow Conf.*, *51*, 161-164, 1984.

Davis, R. E. and D. Marks, Undisturbed measurement of the energy and mass balance of a deep alpine snowcover, *Proc. Western Snow Conf.*, *48*, 62-67, 1980.

Horton, R., The melting of snow, *Monthly Weath. Rev.*, *43*, 599-605, 1915.

Light, P. and M. Kohler, Forecasting seasonal runoff by statistical methods, *Eos, Trans. Amer. Geophys. Union*, *24, part II*, 719-736, 1943.

Linsley, R. K., A simple procedure for the day-to-day forecasting of runoff from snowmelt, *Eos, Trans. Amer. Geophys. Union*, *24, part I*, 62-67, 1943.

Marks, D. and J. Dozier, A clear-sky longwave radiation model for remote alpine areas, *Arch. Meteorol. Geophys. Bioklim., Ser. B*, *27*, 159-187, 1979.

Marks, D., R. Kattelmann, J. Dozier, and R. E. Davis, Monitoring snowcover properties and processes in a small alpine watershed, in *Proceedings of Sixth International Northern Research Basins Symposium / Workshop*, edited by H. S. Santeford, pp. 259-275, Mich. Technol. Univ., Houghton, MI, 1986.

Martinec, J., New methods in snowmelt-runoff studies in representative basins, in *The Hydrological Characteristics of River Basins*, IAHS-AIHS Publ. 117, pp. 99-107, Intl. Assoc. Hydrol. Sci., Wallingford, UK, 1975.

Martinec, J., Limitations in hydrological interpretations of snow coverage, *Nordic Hydrol.*, *11*, 209-220, 1980.

Martinec, J., Runoff modeling from snow covered area, *IEEE Trans. Geosci. Remote Sens.*, *GE-20*, 259-262, 1982.

Martinec, J., Modelling the snow accumulation and snowmelt runoff, *Mitt. deutscher Verb. Wasserwirt. Kulturbau*, *7*, 59-76, 1984.

Martinec, J., Snowmelt runoff models for operational forecasts *Nordic Hydrol.*, *16*, 129-136, 1985.

Miller, S. A., Some snow-melt runoff characteristics, *Eos, Trans. Amer. Geophys. Union*, *31*, 741-745, 1950.

Rango, A. and J. Martinec, Application of a snowmelt-runoff model using Landsat data, *Nordic Hydrol.*, *10*, 225-238, 1979.

Rango, A. and J. Martinec, Accuracy of snowmelt runoff simulation, *Nordic Hydrol.*, *12*, 265-274, 1981.

Rango, A. and J. Martinec, Snow accumulation derived from modified depletion curves of snow coverage, in *Hydrological Aspects of Alpine and High Mountain Areas*, edited by J. W. Glen, IAHS-AIHS Publ. 138, pp. 83-90, Intl. Assoc. Hydrol. Sci., Wallingford, UK, 1982.

Rango, A. and J. Martinec, The need for improved snow-cover monitoring techniques, in *Hydrologic Applications of Space Technology*, edited by A. I. Johnson, IAHS-AISH Publ. 160, pp. 173-179, Intl. Assoc. Hydrol. Sci., Wallingford, UK, 1986.

Rango, A., J. Martinec, J. Foster, and D. Marks, Resolution in operational remote sensing of snow cover, in *Hydrological Applications of Remote Sensing and Remote Data Transmission*, edited by B. E. Goodison, IAHS-AIHS Publ. 145, pp. 371-382, Intl. Assoc. Hydrol. Sci., Wallingford, UK, 1983.

Tangborn, W. V., A model to forecast short-term snowmelt runoff using synoptic observations of streamflow, temperature, and precipitation, *Water Resour. Res.*, *16*, 778-786, 1980.

U.S. Army Corps of Engineers, *Snow Hydrology*, Rep. PB-151660, 437 pp., USACE, Portland, OR, 1956.

Wilson, W. T., An outline of the thermodynamics of snow-melt, *Eos, Trans. Amer. Geophys. Union*, *22*, 182-195, 1941.

World Meteorological Organization, Intercomparison of conceptual models used in operational hydrological forecasting, in *Operational Hydrology*, Rep. 7, WMO-429, pp. 98-162, 1975.

World Meteorological Organization, WMO project for the intercomparison of conceptual models of snowmelt runoff, in *Hydrological Aspects of Alpine and High-Mountain Areas*, edited by J. W. Glen, IAHS-AIHS Publ. 138, pp. 193-202, Intl. Assoc. Hydrol. Sci., Wallingford, UK, 1982.

Yen, Y.-C., Heat transfer characteristics of naturally compacted snow, *Tech. Rep. 166*, 9 pp., U.S. Army Cold Regions Res. Engrg. Lab., Hanover, NH, 1965.

TABLE 6.2. Recorded Parameters and Instrumentation
Emerald Lake Watershed, 1986 Water Year

Recorded Data	Instrument	Model	$NE\Delta$	Linearity	Precision
Radiation:		I_{sol}, I_{nir}, I_{lw} Measured at Tower, Ridge			
Wavelength Range			($W m^{-2}$)	($W m^{-2}$)	($W m^{-2}$)
285–2800 nm	Pyranometer	Eppley PSP, WG7	5.0	±7	±10
700–2800 nm	Pyranometer	Eppley PSP, RG8	0.5	±3.5	±5
4–50 μm	Pyrgeometer	Eppley PIR, Silicon	0.5	±5	±10
Air Temperature:		T_a Measured at Tower, Inlet, Pond, Ridge			
Effective Range			(°C)	(°C)	(°C)
–25 to 25 °C	Thermistor	YSI 44104	0.04	±0.12	±0.25
–40 to 80 °C	Thermistor	Physchem TH15	0.04	±0.25	±0.5
–40 to 60 °C	Thermistor	Vaisala HMP113Y	0.04	±0.3	±0.5
–20 to 40 °C	Thermograph	Weathertronics	0.5	±1.0	±2.0
Humidity:		RH, e_a Measured at Tower, Inlet, Ridge			
Range					
0 to 101 kPa	Condensation Mirror	General Eastern 1200 DPS	0.25Pa	±1.0Pa	±5.0Pa
20 to 90 %	LiCl	Physchem TH15	0.05%	±5%	±10%
12 to 4115 Pa	Resistance		0.3Pa	±30Pa	±60Pa
0 100 %	Electrical	Vaisala HMP113Y	0.05%	±2%	±4%
0 to 4242 Pa	Capacitance		0.3Pa	±12Pa	±25Pa
0 to 90 %	Hygrograph	Weathertronics	0.5%	±5%	±15%
0 to 4115 Pa			3Pa	±30Pa	±100Pa
Snow & Soil Temperature:		T_s, $T_{g,0}$, T_g Measured at Inlet, Pond, Ridge			
Effective Range			(°C)	(°C)	(°C)
–25 to 10 °C	Thermistor	YSI 44104	0.04	±0.12	±0.25
Wind Speed:		u Measured at Inlet, Ridge			
Effective Range			($m s^{-1}$)	($m s^{-1}$)	($m s^{-1}$)
0.5 to 27.2 $m s^{-1}$	Cup Anemometer	Met One 014L	±0.25	±0.5	±1.0
0.4 to 50 $m s^{-1}$	Cup Anemometer	RM Young 12005	±0.02	±0.5	±0.6

TABLE 6.3. Air and Snow Surface Temperature (T_a, T_s) Monthly Averages (°C), Emerald Lake Watershed, 1986 Water Year

Month	T_a	$T_{a\ max}$ †	$T_{a\ min}$ †	Range	T_s
Ridge Site					
Nov	-1.71	2.43	-4.66	7.09	-2.76
Dec	-5.41	-4.25	-6.52	2.27	-5.42
Jan	-1.21	5.40	-4.46	9.86	-1.93
Feb	-2.15	2.02	-4.73	6.75	-3.07
Mar	-1.06	2.12	-3.07	5.19	-1.89
Apr	1.24	9.65	-4.50	14.15	-1.19
May	5.56	11.66	0.84	10.82	-0.51
Jun	9.01	12.78	5.87	6.91	0.00
Jul	8.66	11.54	6.13	5.41	0.00
Aug	10.13	12.97	7.78	5.19	0.00
Sep	3.83	7.89	0.83	7.06	-0.43
Lake Site					
Nov	-0.81	2.98	-3.66	6.64	-2.15
Dec	-0.36	3.06	-2.85	5.91	-1.70
Jan	1.05	4.39	-1.62	6.01	-0.41
Feb	-1.54	2.66	-4.25	6.91	-2.79
Mar	0.91	6.17	-2.51	8.68	-1.34
Apr	1.46	8.15	-2.91	11.06	-0.93
May	4.54	9.60	0.77	8.83	-0.25
Jun	8.38	12.41	5.29	7.12	0.00
Jul	8.72	11.79	6.28	5.51	0.00
Aug	10.28	12.86	8.20	4.66	0.00
Sep	4.19	7.36	1.82	5.54	-0.29

† $T_{a\ max}$ and $T_{a\ min}$ are the monthly averages of the daily maximum and minimum air temperature.

TABLE 6.4. Air and Snow Surface Vapor Pressure (e_a, e_s) Monthly Averages (Pa), Emerald Lake Watershed, 1986 Water Year

Month	e_a	$e_{a\ max}$ †	$e_{a\ min}$ †	Range	e_s
Ridge Site					
Nov	320	384	249	135	497
Dec	292	354	236	118	391
Jan	331	381	268	112	524
Feb	314	381	261	120	482
Mar	366	416	320	96	528
Apr	351	413	303	110	558
May	362	419	325	95	588
Jun	361	415	326	89	611
Jul	380	430	342	88	611
Aug	303	388	241	147	611
Sep	273	353	214	138	591
Lake Site					
Nov	340	397	286	111	522
Dec	292	354	238	116	544
Jan	322	390	255	136	591
Feb	305	388	229	159	495
Mar	330	395	276	118	553
Apr	344	406	294	112	569
May	372	424	334	90	599
Jun	355	403	323	79	611
Jul	372	417	339	78	611
Aug	379	414	353	61	611
Sep	367	416	328	88	597

† $e_{a\ max}$ and $e_{a\ min}$ are the monthly average of the daily maximum and minimum vapor pressure.

TABLE 6.5. Wind Speed (u)
Monthly Averages ($m\,s^{-1}$), Emerald Lake Watershed, 1986 Water Year

Month	u	u_{max}†	u_{min}†	Range
Ridge Site				
Nov	6.8	8.9	3.7	5.2
Dec	5.7	11.8	2.2	9.6
Jan	7.2	13.9	2.7	11.3
Feb	7.4	14.1	2.8	11.3
Mar	8.9	16.9	2.8	14.0
Apr	9.3	16.8	2.6	14.3
May	6.7	13.9	2.0	11.9
Jun	6.2	14.0	1.3	12.6
Jul	6.0	11.6	1.5	10.1
Aug	6.5	13.5	0.8	12.8
Sep	6.7	13.8	1.4	12.4
Lake Site				
Nov	4.4	7.3	1.8	5.5
Dec	6.5	9.4	3.8	5.7
Jan	5.4	9.0	2.6	6.4
Feb	4.3	8.8	1.3	7.5
Mar	4.5	8.2	1.5	6.7
Apr	4.6	8.5	1.3	7.2
May	4.6	7.3	2.2	5.1
Jun	5.4	8.3	2.0	6.3
Jul	3.6	6.1	0.9	5.2
Aug	3.3	5.8	0.7	5.2
Sep	3.2	6.5	0.7	5.9

† u_{max} and u_{min} are the monthly averages of the daily maximum and minimum wind speed.

Figure 6.1. Daily (24 hour) mean air temperature (T_a) (top), daily maximum hourly average air temperature (T_{a_max}) (middle) and daily minimum hourly average air temperature (T_{a_min}) (bottom) for the ridge and lake sites, Emerald Lake watershed, 1986 water year.

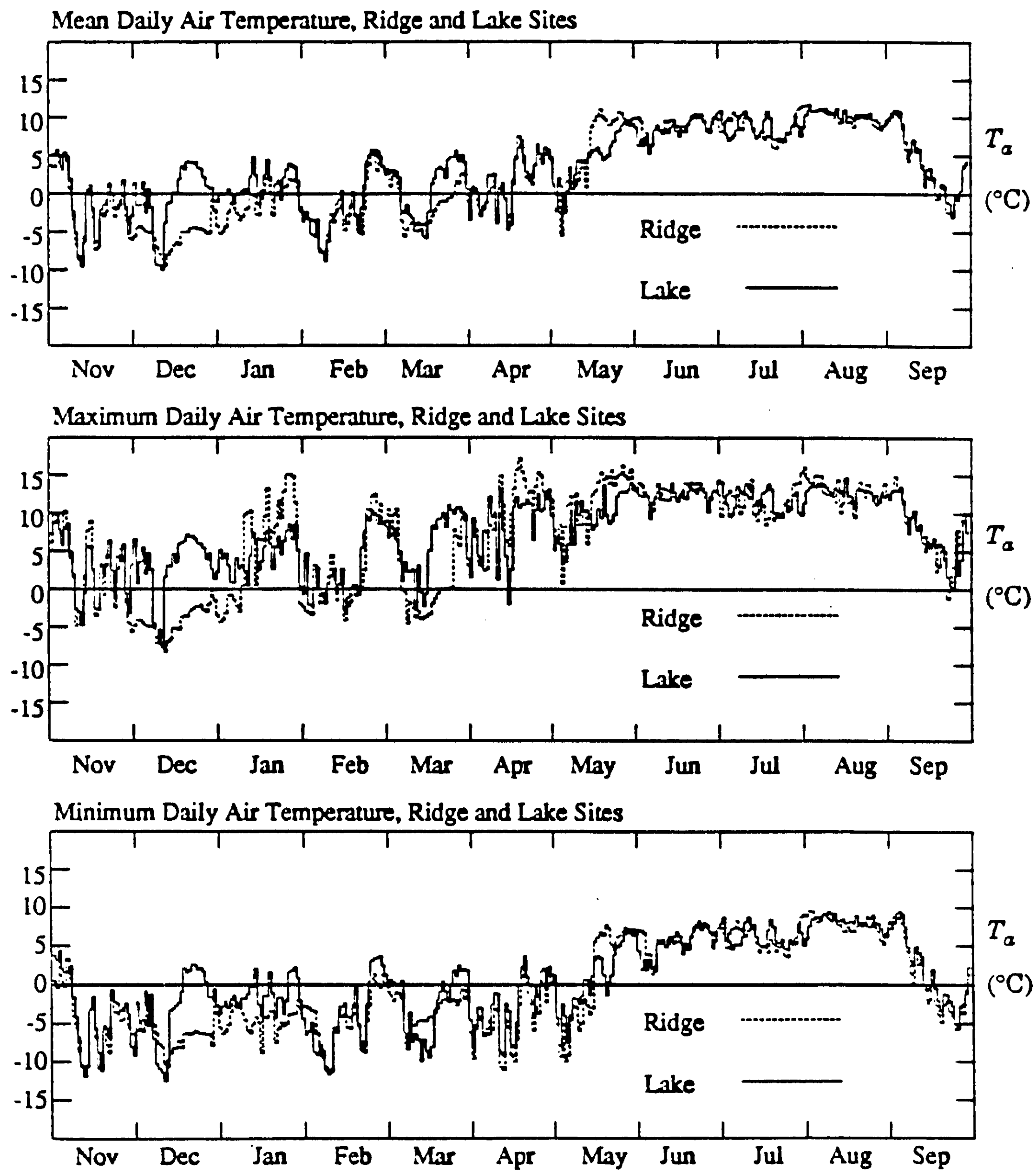

Figure 6.2. Wind speed (u) vs. air temperature (T_a) at the ridge and lake sites, Emerald Lake watershed, 1986 water year. Based on air temperature values prior to filtering with Equation 1.

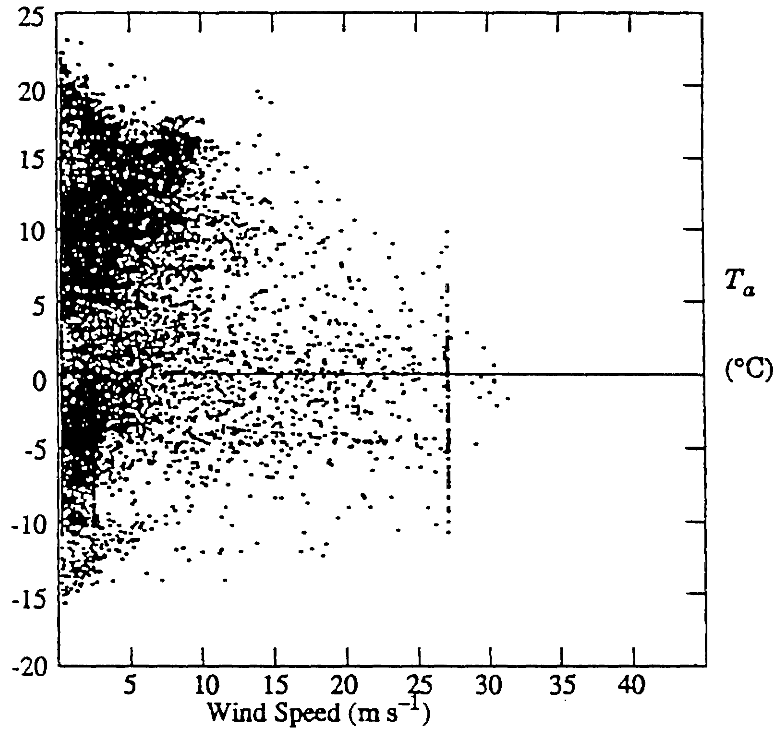

Figure 6.3. Daily (24 hour) mean snow surface temperature (T_s) for the ridge and lake sites, Emerald Lake watershed, 1986 water year. Values are based on hourly averages calculated from Equation 2.

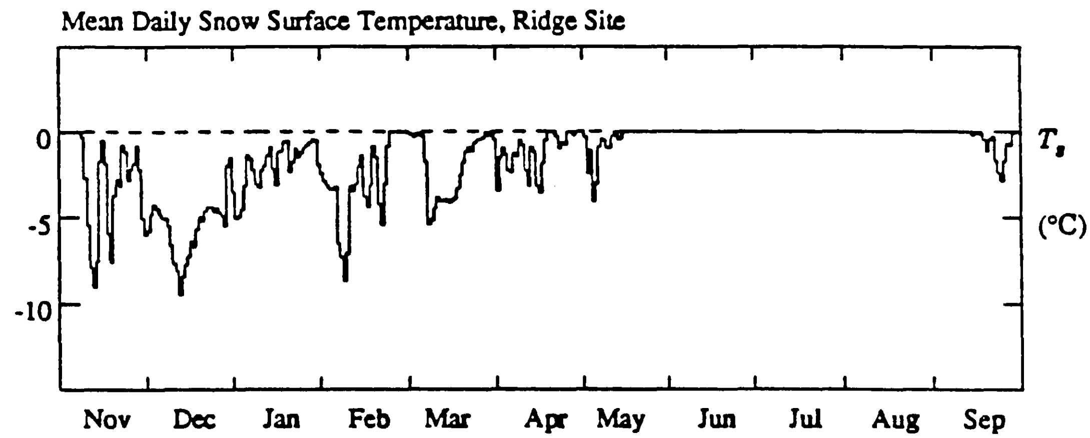

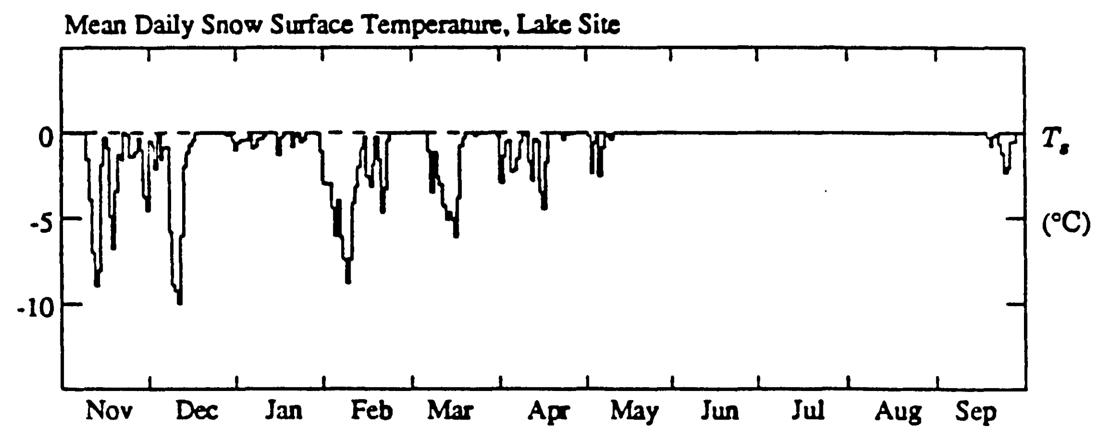

Figure 6.4. Daily (24 hour) mean vapor pressure (e_a) (top), daily maximum hourly average vapor pressure (e_{a_max}) (middle), and daily minimum hourly average vapor pressure (e_{a_min}) (bottom) for the ridge and lake sites, Emerald Lake watershed, 1986 water year.

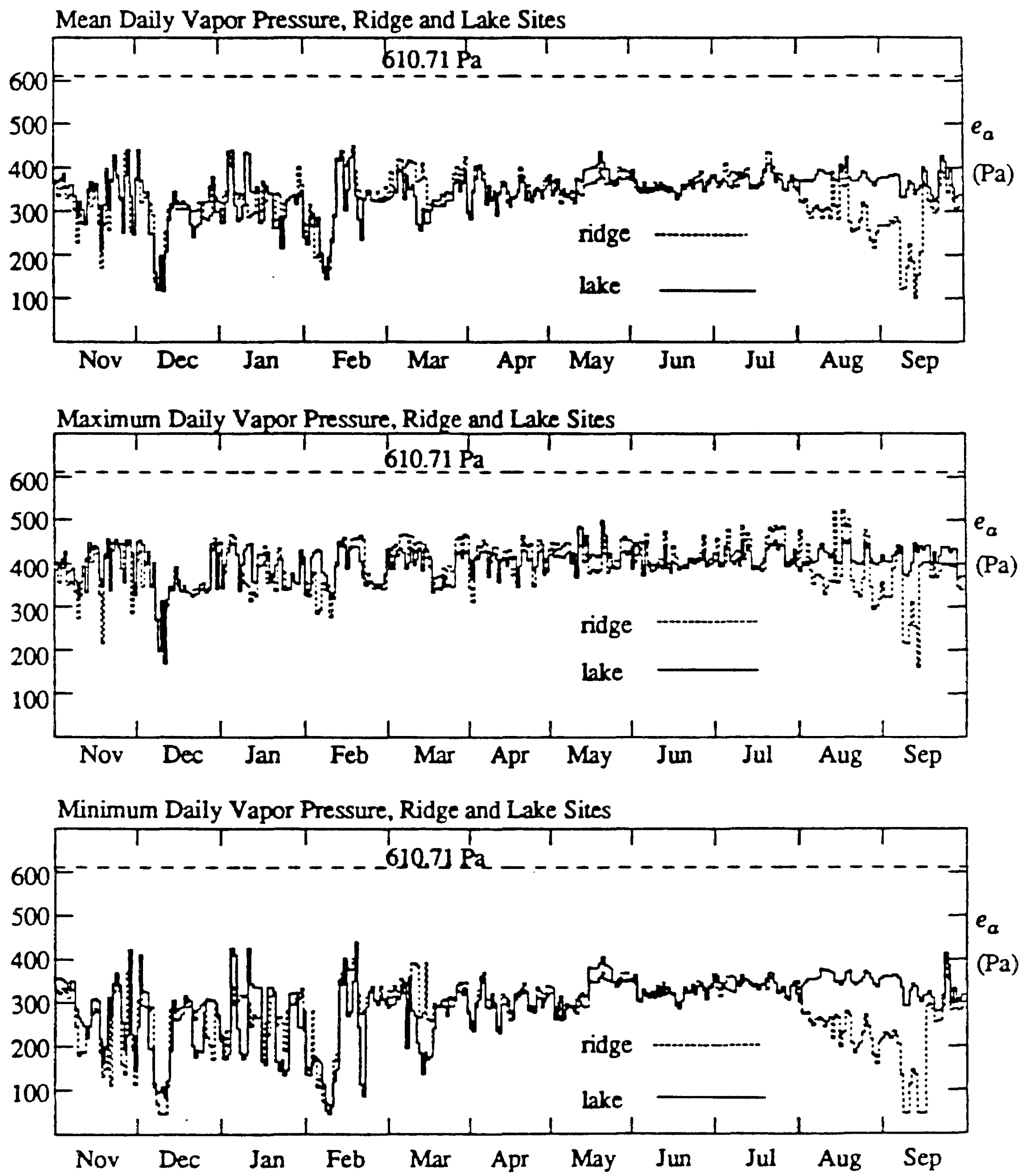

Figure 6.5. Hourly average snow surface vapor pressure gradient ($e_a - e_s$) for the ridge and lake sites, Emerald Lake watershed, 1986 water year. Snow surface vapor pressure e_s is assumed to be the saturation vapor pressure at T_s. Positive values indicate condensation on the snow surface.

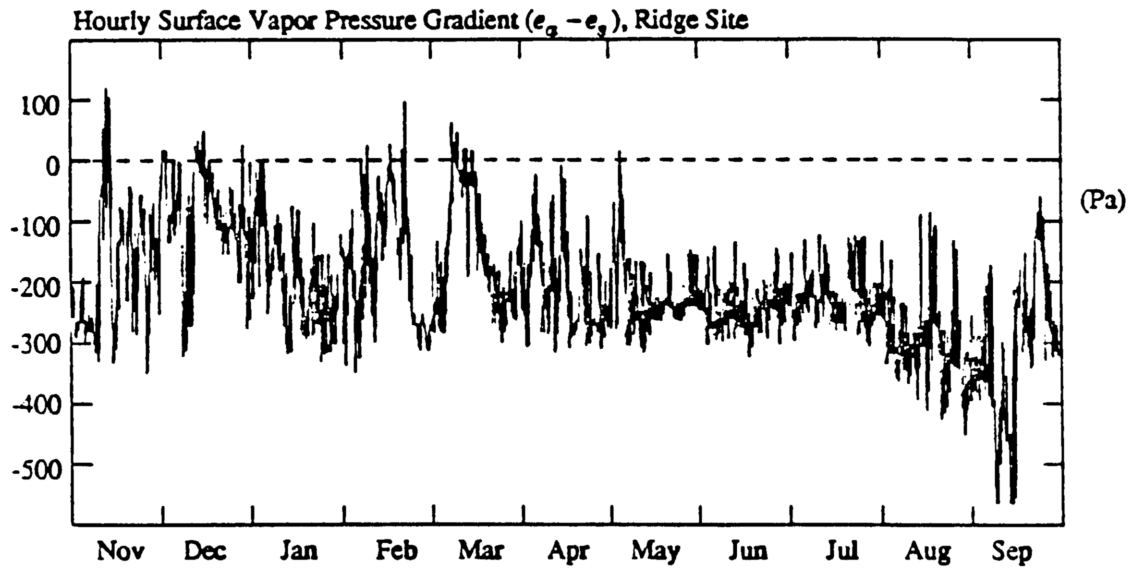

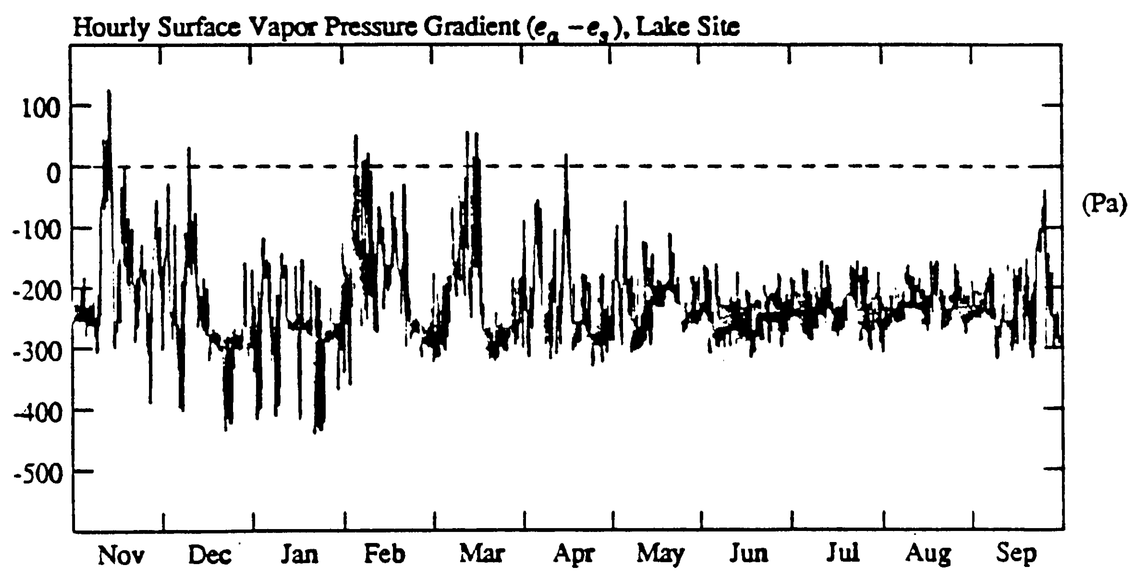

Figure 6.6. Daily (24 hour) mean wind speed (u) (top), daily maximum hourly average wind speed (u_{max}) (middle), daily minimum hourly average wind speed (u_{min}) (bottom) for the ridge and lake sites, Emerald Lake watershed, 1 water year.

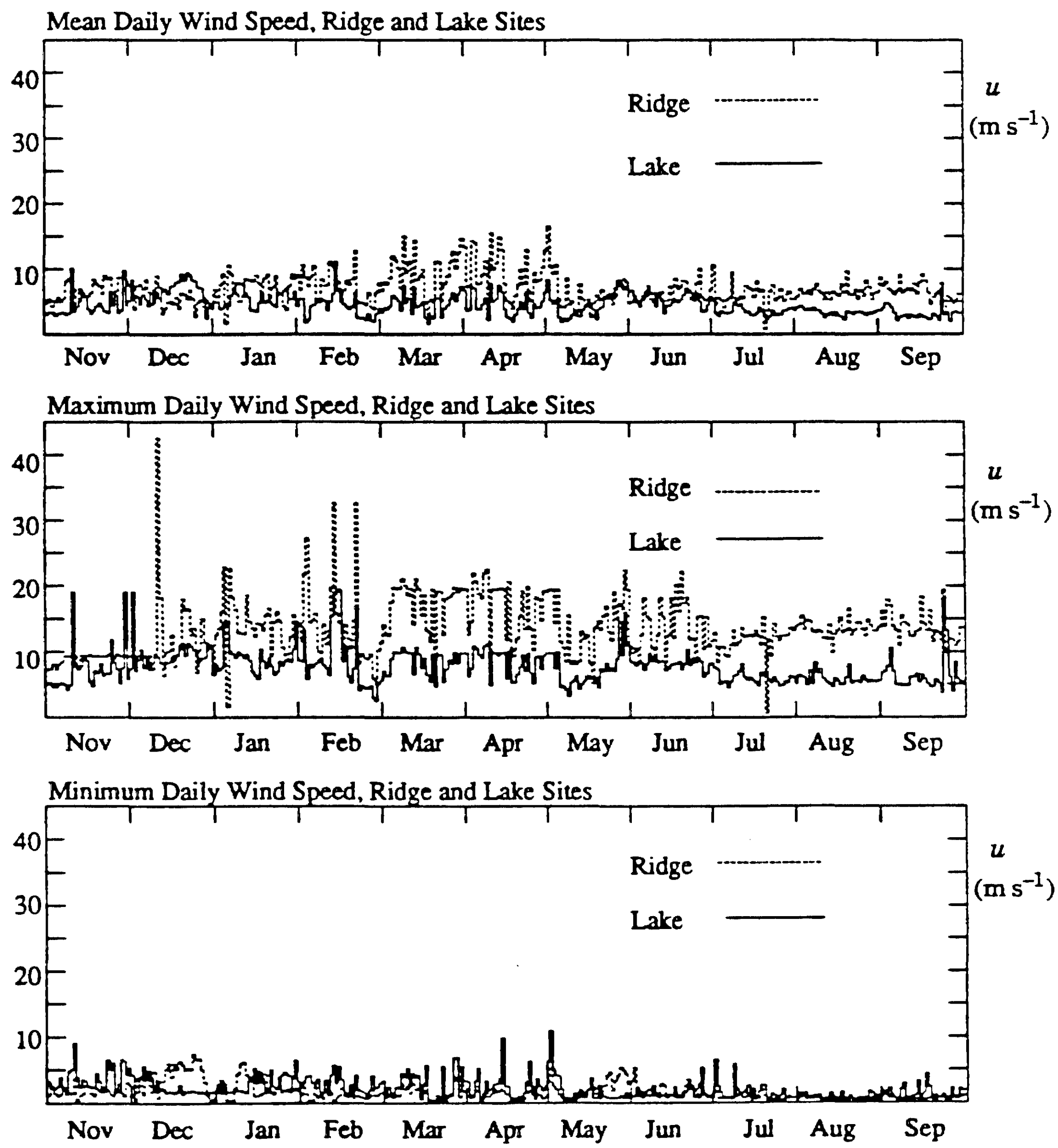

Figure 6.7. Daily (24 hour) mean temperatures for the soil 50 cm below the surface (T_g), at the snow/soil interface ($T_{g,0}$), and snow temperature +30 cm above the soil surface ($T_{s,l}$) (ridge site only), for the ridge and lake sites, Emerald Lake watershed, 1986 water year. Values based on averages of 24 to 96 measurements, per day, at one or two locations.

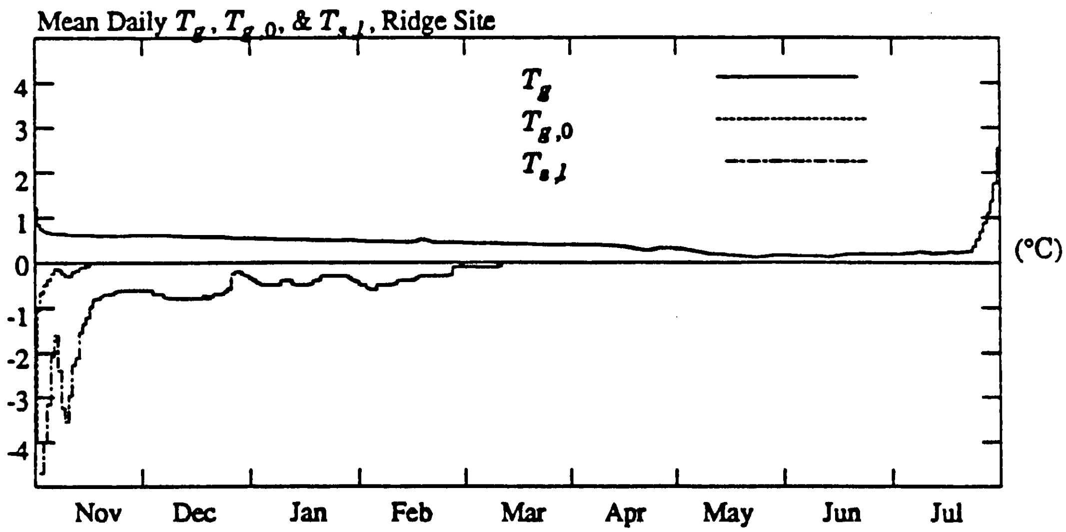

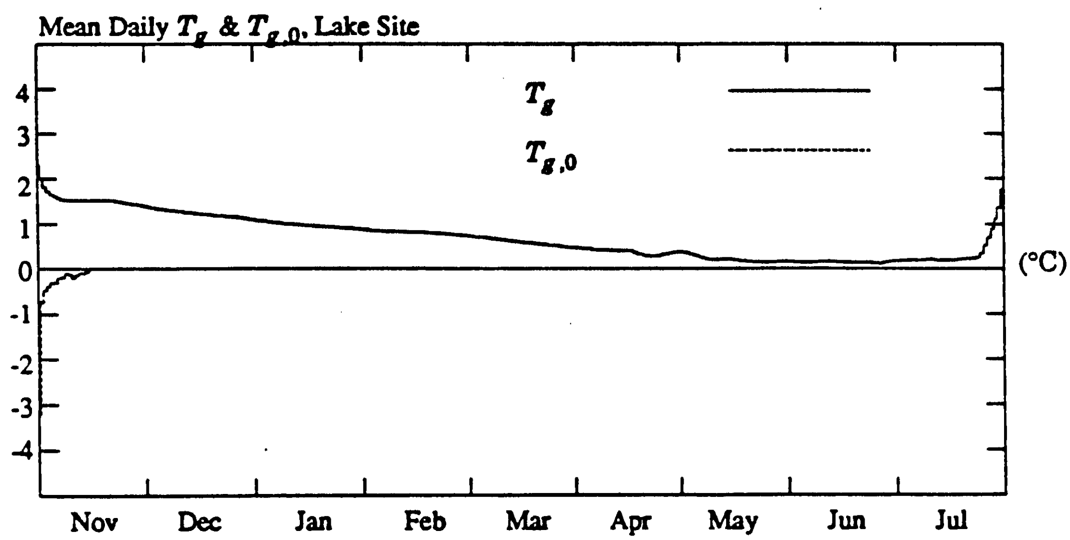

7. Rapid Calculation of Terrain Parameters from Digital Elevation Data

Examination of watershed processes in alpine terrain requires consideration of topographic effects on solar radiation and runoff. Unfortunately digital elevation grids consist of many points; therefore it is crucial that algorithms not only be accurate, but computationally efficient. For the Integrated Watershed Study we have developed many such algorithms, and they are briefly reviewed in this chapter.

7.1. Use of Digital Elevation Models in Radiation Calculations

In all but very gentle terrain, significant variation in the surface climate and in remote sensing images results from local topographic effects. The major contributors to this variation are solar and longwave (thermal) irradiance, although there are also important topographic variations in wind speed and soil moisture. The topographic effects on solar irradiance are mainly variation in illumination angle and shadowing from local horizons. In the thermal part of the electromagnetic spectrum, the emission from surrounding slopes usually causes valley bottoms to receive more thermal irradiance than unobstructed areas. Problems in calculating radiation over mountainous areas have been addressed by many papers that have appeared in the last two decades [Garnier and Ohmura, 1968; Williams et al., 1972; Brazel and Outcalt, 1973; Unsworth, 1975; Dozier and Outcalt, 1979; Klucher, 1979; Marks and Dozier, 1979; Dozier, 1980; Arnfield, 1982; Dave and Bernstein, 1982; Olyphant, 1984; Anderson, 1985; Biber, 1986; Olyphant, 1986; Proy, 1986].

Most radiation calculations over terrain are made with the aid of digital elevation grids, whereby elevation data are represented by a matrix. In the U.S., these are available as "Digital Elevation Models" (DEMs) from the U.S. Geological Survey [Elassal and Caruso, 1983]. The 1:250,000 quadrangles for the entire U.S. are available at 63.5 m grid resolution (0.01 inch at map scale), and the 1:24,000 quadrangles are available at 30 m grid resolution.

The rationale for addressing the problem of rapid calculation of the necessary terrain parameters stems from the large size of the DEMs used in some current applications. The earlier investigations cited above used either coarse grid spacings or small areas, with the resulting grids containing only 10^2–10^3 points. Even in these applications [Dozier and Outcalt, 1979; Anderson, 1985] computer time for generation of terrain parameters accounted for a significant part of the total computer resources used. In our own current application, investigation of the snow surface radiation balance in the southern Sierra Nevada, we often use terrain grids of 10^5–10^6 points.

It is possible to reduce the computation time required for calculation of some terrain parameters through the use of better algorithms, lookup tables to replace calculations, and integer instead of floating-point arithmetic. In this chapter we describe rapid methods for calculation of:

(1) slope and azimuth
(2) illumination angle
(3) horizons
(4) view factors for radiation from sky and terrain.

This list includes all necessary variables used in radiation models. The drainage basin algorithm used to prepare some of the figures is described in detail elsewhere [Marks et al., 1984]. We also hope that the techniques described can be extended or generalized to other calculations with DEMs [e.g. Zecharias and Brutsaert, 1985; Band, 1986; O'Loughlin, 1986].

7.2. Data Representation

We avoid the use of floating-point numbers in storing large data sets, such as satellite images, digital elevation models, and any parameters derived from them, even though the values represented are real rather than integer quantities. The reasons for this are reduction of the size of the data set and portability between machines with different internal floating-point representation.

The common strategy adopted here is data representation by "linear quantization." $Q_L(x,N)$ is the N-bit linear quantization of a real number x, whereby an unsigned N-bit integer in the range $[0, 2^N-1]$ is linearly mapped to the range $[x_{\min}, x_{\max}]$.

$$Q_L(x,N) = \left\lfloor (2^N-1)\,\frac{x - x_{\min}}{x_{\max}-x_{\min}} + U_r \right\rfloor \tag{25}$$

Its inverse is

$$x = (x_{\max}-x_{\min})\,\frac{Q_L(x,N)}{2^N-1} + x_{\min} \tag{26}$$

The "floor" notation in equation (25) means that we take the largest integer not greater than the quantity within. Conventional rounding of the data would be to set $U_r = 0.5$. However, under the circumstance where the original x's are integers and $|x_{\max}-x_{\min}| < 2^N-1$, rounding in this way can introduce artifacts into the data and the presence of "empty bins" in the resulting histogram [Bernstein et al., 1984]. A better procedure in such cases is to set U_r to a uniformly distributed random number in the range $[0,1]$.

We need store only the quantized integer values and the floating-point pair $[x_{\min}, x_{\max}]$. Normally $x_{\max} > x_{\min}$, but the definitions given above do not require this, and we sometimes reverse the quantization.

7.3. Boundary Conditions for Radiation Models

The radiative transfer equation [Chandrasekhar, 1960] for plane-parallel atmospheres is usually expressed as

$$\cos\theta\,\frac{dL(\tau,\theta,\phi)}{d\tau} = -L(\tau,\theta,\phi) + J(\tau,\theta,\phi) \tag{27}$$

where L is radiance at optical depth τ in direction θ,ϕ, and ϕ is the azimuth and θ the angle from zenith. J is the source function; it results from scattering of both direct and diffuse radiation or, at thermal wavelengths, emission.

Solution of equation (27) requires that we specify upper and lower boundary conditions. At the top of the atmosphere the boundary condition is simple, $L\downarrow(0)=0$. At the bottom of the atmosphere over rugged terrain, however, the boundary condition is more complicated. In the solar spectrum irradiance has three sources: (1) direct irradiance from the sun, (2) diffuse irradiance from the sky, where a portion of the overlying hemisphere is obscured by terrain, and (3) direct and diffuse irradiance on nearby terrain that is reflected toward the point whose boundary condition we want to specify. In the thermal portion of the spectrum the solar contribution is absent, the diffuse irradiance results from atmospheric emission, and the contribution from the surrounding terrain is from emission instead of reflection. For remote sensing interpretation, the upwelling radiation normal to a slope S must be normalized to a horizontal plane by multiplication by $\cos S$.

The direct irradiance on a slope is

$$E_s = \cos\theta_s \, E_0 e^{-\tau_0/\cos\theta_0} \tag{28}$$

E_0 is the exoatmospheric solar irradiance perpendicular to the sun's rays; τ_0 is the optical depth of the atmosphere; θ_0 is the solar illumination angle on a horizontal surface; and θ_s is the solar illumination angle on the slope, given by:

$$\cos\theta_s = \cos S \cos\theta_0 + \sin S \sin\theta_0 \cos(\phi_0 - A) \tag{29}$$

S is the slope angle, A is the slope's aziumth, and ϕ_0 is the solar azimuth. Azimuths are usually measured from south, with positive angles east of south (counterclockwise). The effect of earth and atmosphere curvature on the path length is less than 1% for $\theta_0 \le 72°$; for larger solar zenith angles *Kasten's* [1966] empirical equations for the optical path length can be used.

Diffuse irradiance from the sky, either scattered or emitted, is

$$E_d = \pi V_d \overline{L_d} \tag{30}$$

$\overline{L_d}$ is the mean downward radiance on an unobstructed horizontal surface, so $\pi \overline{L_d}$ is the diffuse irradiance. The "sky view factor" V_d is the ratio of the diffuse sky irradiance at a point to that on an unobstructed horizontal surface, i.e. $0 < V_d \le 1$. It accounts for the slope and orientation of the point, the portion of the overlying hemisphere that is visible to the point, and the anisotropy of the diffuse irradiance. We define $\eta_d(\theta,\phi)$ as an anisotropy factor such that $\eta_d(\theta,\phi)\overline{L_d} = L(\theta,\phi)$. Therefore η_d is normalized such that its hemispheric integral projected onto a horizontal surface is π, i.e.

$$\int_0^{2\pi}\int_0^{\pi/2} \eta_d(\theta,\phi) \sin\theta \cos\theta \, d\theta \, d\phi = \pi \tag{31}$$

V_d on a slope S with azimuth A is found by projecting each element of η_d onto the slope and integrating over the unobstructed hemisphere, i.e. from the zenith downward to the local horizon, through angle H_ϕ, for each direction ϕ. For an unobstructed horizontal surface $H_\phi = \pi/2$ (see Figure 7.1). The horizon can result either from "self-shadowing" by the slope itself or from adjacent ridges. In the isotropic case where $\eta_d = 1$, the inner integral in equation (32a) below, for a given azimuth, can be evaluated analytically, leading to the approximation in (32b).

$$V_d = \frac{1}{\pi} \int_0^{2\pi}\int_0^{H_\phi} \eta_d(\theta,\phi) \sin\theta \times \tag{32a}$$

$$[\cos\theta \cos S + \sin\theta \sin S \cos(\phi - A)] \, d\theta \, d\phi$$

$$\approx \frac{1}{2\pi} \int_0^{2\pi} \cos S \sin^2 H_\phi - \sin S \cos(\phi - A) \times \tag{32b}$$

$$(\sin H_\phi \cos H_\phi - H_\phi) \, d\phi$$

Contribution from the surrounding terrain is

$$E_t = \pi C_t \overline{L_t} \tag{33}$$

$\pi \overline{L_t}$ is the average irradiance reflected or emitted from the surrounding terrain. The terrain configuration factor C_t includes both the anisotropy of the radiation and the geometric effects between the point and each point in surrounding terrain with which it is mutually visible. The contribution of each of these terrain elements to the configuration factor could be computed [Siegel and Howell, 1981], but this is a formidable computational problem. Instead we use the following approximation:

$$C_t = \frac{1}{\pi} \int_0^{2\pi}\int_{H_\phi}^{\psi_\phi} \eta_\upsilon(\theta,\phi) \sin\theta \times \tag{34a}$$

$$[\cos\theta \cos S + \sin\theta \sin S \cos(\phi - A)] \, d\theta \, d\phi$$

$$\approx \frac{1 + \cos S}{2} - V_d \tag{34b}$$

η_υ accounts for the anisotropy of the reflected or emitted radiance from the surrounding terrain, including geometric effects. The limits of integration for the inner integral are from the horizon downward to where a ray is parallel to the slope:

$$\psi_\phi = \arctan\left[\frac{-1}{\tan S \cos(\phi - A)}\right] \tag{35}$$

In the upslope direction $\cos(\phi - A)$ is negative, so $\psi_\phi < \pi/2$. In the downslope direction $\cos(\phi - A)$ is positive, so $\psi_\phi > \pi/2$. Across the slope $\psi_\phi = \pi/2$.

Rigorous calculation of C_t is difficult because it is necessary to consider every terrain facet that is visible from a point in order to calculate η_t. In contrast to the sky radiation, the isotropic assumption is unrealistic, because considerable anisotropy results from geometric effects even if the surrounding terrain is a Lambertian reflector or a blackbody emitter. We therefore note that V_d for an infinitely long slope is $(1 + \cos S)/2$, which leads to the approximation in (34b).

7.4. Algorithms for Rapid Calculation

The terrain grid is oriented as in Figure 7.2. Spacing between grid points is Δh in both the x and y directions, although the algorithms presented here could be modified for rectangular spacing if desired. Elevations z are stored as N-bit linear quantizations $Q_L(z, N)$ in the range $[z_{min}, z_{max}]$. The grid is oriented with the rows from west to east and the columns from north to south, so that x increases southward and y increases eastward.

The algorithms are formally described using the C programming language [Kernighan and Ritchie, 1978; Harbison and Steele, 1984]. The code should also be understandable by anyone familiar with Pascal or Algol, and the reader has the security of knowing that the algorithms have been successfully run in the forms that they appear in the chapter. Some of the more esoteric features of C, such as use of register variables and some arcane but speedy pointer operations, have been omitted for simplicity. The function `POW2(n)` returns 2^n and is usually implemented as a macro for positive n:

```
#define POW2(n) (1 << (n))
```

The constant `PI` is assumed to be defined. Otherwise it can be calculated as

```
PI = 4 * atan(1.)
```

7.4.1. Slope and Azimuth

The sine of the slope angle S with range $[0,1]$, is represented by an M-bit linearly quantized value $Q_L(\sin S,M)$. We use the sine instead of the cosine, because the greatest precision is then for the lowest slopes. Azimuth (or aspect) A is represented by $Q_L(A,M)$ in the range $[-\pi,\pi(1-2^{1-M})]$. $A=0$ is toward the south, and positive azimuths are toward the east; note that $-\pi$ and π are the same azimuth.

The fundamental equations are given below. The signs of the numerator and denominator allow A to be uniquely specified over $[-\pi,\pi]$.

$$\tan S \equiv |\nabla z| = \left[(\partial z/\partial x)^2+(\partial z/\partial y)^2\right]^{1/2} \tag{36}$$

$$\tan A = \frac{-\partial z/\partial y}{-\partial z/\partial x} \tag{37}$$

$\partial z/\partial x$ and $\partial z/\partial y$ are calculated by finite differences. At point i,j:

$$\frac{\partial z}{\partial x} = \frac{z_{i+1,j}-z_{i-1,j}}{2\Delta h} \tag{38a}$$

$$\frac{\partial z}{\partial y} = \frac{z_{i,j+1}-z_{i,j-1}}{2\Delta h} \tag{38b}$$

The elevations are stored in the terrain grid as N-bit linearly quantized integers. Let

$$X = Q_L(z_{i+1,j},N)-Q_L(z_{i-1,j},N)$$
$$Y = Q_L(z_{i,j+1},N)-Q_L(z_{i,j-1},N)$$
$$Z = z_{\max}-z_{\min}$$

Then

$$\frac{\partial z}{\partial x} = \frac{XZ}{\Delta h\,(2^{N+1}-2)} \tag{39a}$$

$$\frac{\partial z}{\partial y} = \frac{YZ}{\Delta h\,(2^{N+1}-2)} \tag{39b}$$

Only the X and Y values vary over the grid; other terms are constant. Note that from (36)

$$\sin S = \left[\frac{|\nabla z|^2}{1+|\nabla z|^2}\right]^{1/2} \tag{40}$$

Therefore, from equation (39a,b), if $Q_L(\sin S,M)$ were a real quantity instead of an integer, it would be given by:

$$Q_L(\sin S,M) = (2^M-1)Z \times \left[\frac{X^2+Y^2}{(X^2+Y^2)Z^2+4(\Delta h)^2(2^N-1)^2}\right]^{1/2} \tag{41}$$

We can invert this and solve for X^2+Y^2.

$$X^2+Y^2 = \frac{4(\Delta h)^2 Q_L^2(\sin S,M)(2^N-1)^2}{[(2^M-1)^2-Q_L^2(\sin S,M)]Z^2} \tag{42}$$

This can be evaluated for each half-integer value of $Q_L(\sin S,M)$ in the range $[0.5, 2^M-1.5]$ to form a lookup table of length 2^M. The solutions are the minimum values of X^2+Y^2 that would round up to each value of $Q_L(\sin S,M)$. Because the number of bits N used to store the elevations is usually greater than or equal to M, the number of bits used to store $\sin S$, no artifacts are introduced into the resulting values by simple rounding instead of random rounding.

Function 1 shows how the lookup table is formed prior to computing slopes and azimuths over a digital elevation grid. For each elevation grid point the differences are calculated and squared; then the linearly quantized slope value is found by searching the table. Function 2 shows a binary search algorithm, which is guaranteed to converge within M iterations for a lookup table of length 2^M.

For azimuths, we note that after substitution of the linearly quantized representations, equation (37) reduces to

$$\tan A = \frac{-Y}{-X} \tag{43}$$

Depending on the signs of the numerator and denominator, the value of A falls into one of the four quadrants:

sign X	sign Y: $-$	sign Y: 0	sign Y: +
$-$	$[0,\pi/2]$	0	$[-\pi/2,0]$
0	$\pi/2$	undef	$-\pi/2$
+	$[\pi/2,\pi]$	$-\pi$	$[-\pi,-\pi/2]$

Thus the lookup table of length 2^M can be subdivided into four tables of length 2^{M-2} each. The entries into these tables are the absolute value $|2^{P-N-1}Y/X|$ and the signs of the numerator and denominator. The multiplication by 2^{P-N-1} prevents truncation effects in the integer division. P is the number of bits in the integer representation of the sum X^2+Y^2; normally $P \geq 2N$.

Function 3 shows how the azimuth lookup table is created, and Function 4 shows how it is searched.

7.4.2. Illumination Angle

The most important variable controlling the incident radiation on a slope in mountainous terrain is the local solar illumination angle. If the sun is not hidden by a local horizon (a problem addressed in the next section) the local illumination angle θ_s on a slope S with azimuth A is given by

$$\cos\theta_s = \cos\theta_0\cos S + \sin\theta_0\sin S\,\cos(\phi_0-A) \tag{44}$$

where θ_0 is the illumination angle on a horizontal surface, and ϕ_0 is the azimuth of illumination.

As in the previous section, the quantities $\sin S$ and A are stored as M-bit linear quantizations. We achieve speed in the calculation of $Q_L(\cos\theta_s, M)$ by the following steps.

1. We ignore variations in latitude and longitude over the terrain grid, or at least over portions of it. Therefore θ_0 and ϕ_0 are constants.

2. Because S and A are stored as linear quantizations, there are only 2^M possible values for $\cos S$, $\sin S$, and $\cos(\phi_0 - A)$. We therefore build lookup tables to avoid computing trigonometric functions at each point (Function 5).

3. Moreover, although there are 2^{2M} possible S, A pairs, not all combinations occur in a typical terrain grid. Therefore the algorithm can keep track of which S, A pairs have already been encountered (Function 6).

7.4.3. Horizons

The cosine of the angle from the zenith to the horizon in a given azimuth ϕ is represented by an M-bit linear quantization in the range [0,1]. The algorithm described in this section was previously published [Dozier et al., 1981], but we have implemented a few changes to make it clearer.

By rotating a grid in direction ϕ we reduce the horizon problem to its one-dimensional equivalent. Along each row of the rotated grid (Figure 7.3) we want to calculate the horizon angle in the forward (we could choose backward) direction for each point; then we rotate the solution back to the original orientation. We showed that this can be solved in "order N" iterations, where N is the number of points in the profile. All other methods for solving this problem [Williams et al., 1972; Dozier and Outcalt, 1979] are apparently order N^2, so computing times for larger elevations grids become enormous. The fast solution is achieved by casting the problem in a somewhat ill-posed way. Instead of directly finding the horizon angle, we instead find the point that forms the horizon.

This has an additional advantage. While the angles to the horizons will change with vertical exaggeration of the terrain grid, the coordinates of the points that form the horizons do not. When computing orthographic views of satellite images registered to elevation grids, the same horizon algorithm can be used to decide *a priori* which points in the image are visible [Dubayah and Dozier, 1986]. By storing the points that form the horizons, one can easily generate different vertical exaggerations of the same grid.

For a grid row, an elevation function z is defined on the points $j = 0, 1, \ldots, N-1$. Since the points are evenly spaced, the abscissa is specified by $j\,\Delta h$. The horizon function h in the forward direction satisfies, for all $0 \le i < N$:

1. $i \le h_i$. Hence $h_{N-1} = N-1$.

2. If $z_i \ge z_j$ for all $i < j < N$, then $h_i = i$. That is, if the elevation is greater than or equal to any other point in the forward direction, we say it is its own horizon.

3. If k is the largest value greater than i and less than N such that $z_k > z_i$ and

$$z_j \le z_i + (z_k - z_i) \left| \frac{j-i}{k-i} \right|$$

for all $i < j < N$, $j \ne k$, then $h_i = k$. That is, if two points in the forward direction are equally suitable as horizon candidates, the farthest is chosen.

A simple algorithm for determining the horizon functions for each point would be to compute the slope from each i to each $j > i$ and choose the maxima. Unfortunately the number of comparisons in such an algorithm is order N^2; if the number of points in the profile were doubled, the number of comparisons is quadrupled. Speed is achieved by comparing the slope from i to j with the slope from j to h_j. If the slope from i to j is greater than from j to h_j, then all points forward of j are not visible from i and therefore $h_i = j$. Alternatively, if the slope from j to h_j is greater than the slope from i to j then all points between j and h_j need not be checked, because point h_j is visible from i.

Function 7 shows the one-dimensional horizon algorithm. Once the coordinates of the horizon points are found, the angles to the horizon are easily calculated.

7.4.4. Sky View Factor

The sky view factor V_d (equation 32b) accounts for the portion of the overlying hemisphere that is visible to a grid point. To calculate it one needs to know the slope S and azimuth A of the point, plus the horizon angle H_ϕ in a discrete set of directions ϕ. Usually 16 directions around the circle are enough. Because there are only 2^M possible values for S, A, or H_ϕ, the values of the trigonometric functions in equation (32b) can be stored in tables. Function 8 shows the algorithm.

7.5. Conclusion

The fast algorithms presented here save considerable time in calculating terrain parameters for watershed analysis.

7.6. Code Listings

Following are the code listings for the functions referenced in this chapter.

Function 1. Create Slope Lookup Table

```
slopetbl(m, n, delhsq, zdsq, stbl)
        int             m;              /* # bits for sine slope        */
        int             n;              /* # bits for elevation         */
        double          delhsq;         /* square of grid spacing       */
        double          zdsq;           /* square of elevation range    */
        long           *stbl;           /* slope lookup table           */
{
        int             b;              /* B(sinS, m)                   */
        int             tm;             /* POW2(m)                      */
        double          bm;             /* (B - 1/2) squared            */
        double          tm2;            /* (tm - 1) squared             */
        double          kl;             /* (tm2 * delhsq)/zdsq          */
        double          tn;             /* POW2(n) - 1                  */

 /*
  * these values are constant in loop
  */
        tm = POW2(m);
        tn = POW2(n) - 1;
        tm2 = (tm - 1) * (tm - 1);
        kl = 4 * delhsq * tn * tn / zdsq;
 /*
  * first element of table
  */
        stbl[0] = 0;
 /*
  * loop for every integer from 1 to POW2(m) - 1
  */
        for (b = 1; b < tm; ++b) {
 /*
  * minimum value that would round up to b
  */
                bm = b - 0.5;
                bm *= bm;
                stbl[b] = (long) ((bm * kl) / (tm2 - bm));
        }
}
```

Function 2. Search Slope Lookup Table Given $X^2 + Y^2$

```
int
slsrch(m, sumsq, stbl)
        int             m;              /* # bits in slope lookup table  */
        long            sumsq;          /* X squared + Y squared         */
        long           *stbl;           /* lookup table                  */
{
        int             b;              /* B(sinS, m)                    */
        int             i;
        int             j;
/*
 * beginning and end of lookup table
 */
        b = i = 0;
        j = POW2(m) - 1;
 /*
  * set to maximum if off end of table
  */
        if (sumsq >= stbl[j]) {
                b = j;
        }
 /*
  * otherwise binary search table for spanning values around sumsq
  */
        else {
                while (sumsq > stbl[i]) {
                        b = (i + j) / 2;
                        if (sumsq >= stbl[b])
                                i = b + 1;
                        else
                                j = b - 1;
                }
        }
        return (b);
}
```

Function 3. Create Azimuth Lookup Table

```
extern double   tan();

azmtbl(m, n, p, atbl)
        int             m;          /* # bits for azimuth           */
        int             n;          /* # bits for elevation         */
        int             p;          /* # bits in long int           */
        long            *atbl;          /* azimuth lookup table     */
{
        int             b;          /* B(A, m)              */
        int             blim;           /* POW2(m-2)                */
        double          tn;         /* POW2(p-n-1)                  */
        double          tp;         /* 1/POW2(m-1)                  */
        double          k1;         /* tp * PI              */
        double          k2;         /* k1 * 0.5 + PI        */

 /*
  * constant values in loop
  */
        tp = 1.0 / (double) POW2(m - 1);
        assert(p >= 2 * n);
        tn = (double) POW2(p - n - 1);
        k1 = tp * PI;
        k2 = k1 * 0.5 + PI;
 /*
  * run loop from 1 to POW2(m-2)
  */
        blim = POW2(m - 2);
        atbl[0] = 0;
        for (b = 1; b <= blim; ++b) {
                atbl[b] = (long) (tn * tan(k1 * b - k2));
        }
}
```

Function 4. Search Azimuth Lookup Table Given X and Y

```
int
azmsrch(m, n, p, xd, yd, atbl)
	int		m;		/* # bits for azimuth		*/
	int		n;		/* # bits for elevation		*/
	int		p;		/* # bits in long int		*/
	int		xd;		/* X difference			*/
	int		yd;		/* Y difference			*/
	long		*atbl;		/* from function azmtbl()	*/
{
	int		b;		/* B(A, m)			*/
	int		i;
	int		j;
	int		halfr;		/* half range index, POW2(m-1)	*/
	int		quartr;		/* quarter range, POW2(m-2)	*/
	long		tn;		/* POW2(p-n-1)			*/
	long		r;		/* abs(tn * yd / xd)		*/

	halfr = POW2(m - 1);
	quartr = POW2(m - 2);
	assert(p >= 2 * n);
	tn = POW2(p - n - 1);
 /*
  * general case, neither X- nor Y-difference zero
  */
	if (xd * yd != 0) {
		r = (xd * yd < 0) ? -tn * yd / xd : tn * yd / xd;
		b = i = 0;
		j = quartr;
		if (r >= atbl[j])
			b = j;
 /*
  * binary search of azimuth table
  */
		else {
			while (r > atbl[i]) {
				b = (i + j) / 2;
				if (r >= atbl[b])
					i = b + 1;
				else
					j = b - 1;
			}
		}
 /*
  * b holds correct value if both xd,yd positive, i.e. azimuth is
  * toward NW quad; adjust otherwise
  */
		if (xd < 0)
			b = (yd < 0) ?
				b + halfr	/* SE quad */
				: halfr - b;	/* SW quad */
		else if (yd < 0)
			b += halfr + quartr;	/* NE quad */
	}
 /*
  * X-difference zero; b is set to 'south' arbitrarily if point is flat
  */
	else if (xd == 0) {
		b = halfr;
		if (yd < 0)
			b += quartr;	/* east */
		else if (yd > 0)
			b -= quartr;	/* west */
```

```
        }
 /*
  * Y-difference zero
  */
        else if (yd == 0) {
                b = (xd > 0) ?
                        0               /* north */
                        : halfr;        /* south */
        }
        return (b);
}
```

Function 5. Create Table for Necessary Trigonometric Functions

```
extern double   cos();
extern double   sqrt();

trigtbl(nslope, nazm, phi, sintbl, costbl, cosdtbl)
        int             nslope;         /* number bits in slope         */
        int             nazm;           /* number bits in azimuth       */
        float           phi;            /* solar illumination aziumth   */
        float          *sintbl;         /* all possible values of sinS  */
        float          *costbl;         /* all possible values of cosS  */
        float          *cosdtbl;        /* all values of cos(phi-A)     */
{
        unsigned        j;              /* counter, slope/azm value     */
        float           n;              /* maximum value of j           */
 /*
  * Sines and cosines of each possible slope. (Loop runs backwards from
  * n to zero)
  */
        j = POW2(nslope) - 1;
        n = j;
        ++j;
        do {
                --j;
                sintbl[j] = (float) j / n;
                costbl[j] = sqrt((1 - sintbl[j]) * (1 + sintbl[j]));
        } while (j != 0);
 /*
  * Cosine differences for each possible azimuth.
  */
        j = POW2(nazm);
        n = j;
        ++j;
        do {
                --j;
                cosdtbl[j] = cos(phi + PI * (1 - 2 * (float) j / n));
        } while (j != 0);
}
```

Function 6. Vector of Cosines of Local Illumination Angle

```
cosines(nvals, nbits, sinS, azm, ctheta, stheta, sintbl, costbl, cosdtbl,
                already, shade, cz)
        int             nvals;          /* length of vectors sinS & azm  */
        int             nbits;          /* number of bits in cz          */
        unsigned       *sinS;           /* slope values (integer)        */
        unsigned       *azm;            /* azimuth values (integer)      */
        float           ctheta;         /* cosine of solar zenith angle  */
        float           stheta;         /* sine of solar zenith angle    */
        float          *sintbl;         /* computed by trigtbl           */
        float          *costbl;         /* computed by trigtbl           */
        float          *cosdtbl;        /* computed by trigtbl           */
        int           **already;        /* value already computed?       */
        unsigned      **shade;          /* store for already computed    */
        unsigned       *cz;             /* cosines of local sun angles   */
{
        int             j;              /* loop counter                  */
        int             s;              /* slope index                   */
        int             a;              /* azimuth index                 */
        float           mu;             /* cosine local illum angle      */
        float           n;              /* maximum value                 */

        n = POW2(nbits) - 1;

        for (j = 0; j < nvals; ++j) {
                s = sinS[j];
                a = azm[j];
 /*
  * Compute cosine of local illumination angle, using lookup tables,
  * but only if we haven't already found value for this combination of
  * slope and azimuth.
  */
                if (!already[s][a]) {
                        mu = ctheta * costbl[s] +
                                stheta * sintbl[s] * cosdtbl[a];
                        if (mu <= 0)
                                shade[s][a] = 0;
                        else
                                shade[s][a] = mu * n + 0.5;
                        already[s][a] = 1;
                }

                cz[j] = shade[s][a];
        }
}
```

Function 7. Horizon in Forward Direction for Equi-Spaced Elevation Vector

```
#define slope(i, j, z)  \
        ( ((z[j]) <= (z[i]))? 0 : ((z[j])-(z[i])) / ((float)((j)-(i))) )

horlf(n, z, h)
        int             n;              /* length of vectors    */
        float           z[];            /* elevation function   */
        int             h[];            /* horizon function     */
{
        float           sihj;           /* slope i to h[j]      */
        float           sij;            /* slope i to j         */
        int             i;              /* point index          */
        int             j;              /* point index          */
        int             k;              /* h[j]                 */

 /*
  * End point is its own horizon
  */
        h[n - 1] = n - 1;
 /*
  * Loop from next-to-end backward to beginning
  */
        for (i = n - 2; i >= 0; --i) {
 /*
  * Start with adjacent point in forward direction; loop until slope
  * from i to j is greater than or equal to the slope from j to its
  * horizon.
  */
                k = i + 1;
                do {
                        j = k;
                        k = h[j];
                        sij = slope(i, j, z);
                        sihj = slope(i, k, z);
                } while (sij < sihj);

                if (sij > sihj)         /* j is i's horizon     */
                        h[i] = j;
                else if (sij == 0)      /* i is its own horizon */
                        h[i] = i;
                else                    /* h[j] is i's horizon  */
                        h[i] = k;
        }
}
```

Function 8. Sky View Factor V_d

```
int
viewd(m, nh, s, a, h, htbl, sintbl, costbl, cosdtbl)
        int             m;              /* # bits for view factor        */
        int             nh;             /* # horizon azimuths            */
        int             s;              /* sinS                          */
        int             a;              /* A                             */
        int             *h;             /* horizon vector                */
        double          *htbl;          /* all values of horizon angle   */
        double          *sintbl;        /* all values sinS or sinH_phi   */
        double          *costbl;        /* all values cosS or cosH_phi   */
        double          *cosdtbl;       /* all values of cos(phi-A)      */

{
        int             b;              /* linear quant value of vd      */
        double          cp;             /* cos(phi-A)                    */
        double          cs;             /* cosS                          */
        int             j;              /* index                         */
        int             k;              /* index                         */
        double          n;              /* POW2(m) - 1                   */
        double          ss;             /* sinS                          */
        double          v;              /* view factor vd                */

 /*
  * constants in loop
  */
        cp = cosdtbl[a];
        cs = costbl[s];
        ss = sintbl[s];
 /*
  * sum over all horizon directions
  */
        v = 0;
        for (j = 0; j < nh; ++j) {
                k = h[j];
                v += cs * sintbl[k] * sintbl[k] -
                        ss * cp * (sintbl[k] * costbl[k] - htbl[k]);
        }
 /*
  * convert to linear quantization
  */
        n = POW2(m) - 1;
        b = v * n / (2 * nh) + 0.5;
        return (b);
}
```

7.7. References

Anderson, E. C., A numerical model for the estimation of solar radiation on rugged terrain, Ph.D. Thesis, Ohio State Univ., Columbus, OH, 1985.

Arnfield, A. J., Estimation of diffuse irradiance on sloping, obstructed surfaces: an error analysis, *Arch. Meteorol. Geophys. Bioklim., Ser. B, 30*, 303-320, 1982.

Band, L. E., Topographic partition of watersheds with digital elevation models, *Water Resour. Res., 22*, 15-24, 1986.

Bernstein, R., J. B. Lotspiech, H. J. Myers, H. G. Kolsky, and R. D. Lees, Analysis and processing of Landsat-4 sensor data using advanced image processing techniques and technologies, *IEEE Trans. Geosci. Remote Sens., GE-22*, 192-221, 1984.

Biber, A., Höhenabhängigkeit der globalstrahlung im alpenraum, Diploma Thesis, 138 pp., Geogr. Inst. ETH, Zürich, 1986.

Brazel, A. J. and S. I. Outcalt, The observation and simulation of diurnal surface thermal contrast in an Alaskan alpine pass, *Arch. Meteorol. Geophys. Bioklim., Ser. B, 21*, 157-174, 1973.

Chandrasekhar, S., *Radiative Transfer*, 393 pp., Dover, New York, 1960.

Dave, J. V. and R. Bernstein, Effect of terrain orientation and solar position on satellite-level luminance observations, *Remote Sens. Environ., 12*, 331-348, 1982.

Dozier, J., A clear-sky spectral solar radiation model for snow-covered mountainous terrain, *Water Resour. Res., 16*, 709-718, 1980.

Dozier, J., J. Bruno, and P. Downey, A faster solution to the horizon problem, *Comput. Geosci., 7*, 145-151, 1981.

Dozier, J. and S. I. Outcalt, An approach toward energy balance simulation over rugged terrain, *Geogr. Anal., 11*, 65-85, 1979.

Dubayah, R. and J. Dozier, Orthographic terrain views using data derived from digital elevation models, *Photogram. Engrg. Remote Sens., 52*, 509-518, 1986.

Elassal, A. A. and V. M. Caruso, Digital elevation models, *Circ. 895-B*, 40 pp., U.S. Geol. Survey, Alexandria, VA, 1983.

Garnier, B. J. and A. Ohmura, A method of calculating the direct shortwave radiation income of slopes, *J. Appl. Meteorol., 7*, 796-800, 1968.

Harbison, S. P. and G. L. Steele, Jr., *C: a Reference Manual*, 352 pp., Prentice-Hall, Englewood Cliffs, NJ, 1984.

Kasten, F., A new table and approximation formula for the relative optical air mass, *Arch. Meteorol. Geophys. Bioklim., Ser. B, 14*, 206-233, 1966.

Kernighan, B. W. and D. M. Ritchie, *The C Programming Language*, 228 pp., Prentice-Hall, Englewood Cliffs, NJ, 1978.

Klucher, T. M., Evaluation of models to predict insolation on tilted surfaces, *Solar Energy, 4*, 14-19, 1979.

Marks, D. and J. Dozier, A clear-sky longwave radiation model for remote alpine areas, *Arch. Meteorol. Geophys. Bioklim., Ser. B, 27*, 159-187, 1979.

Marks, D., J. Dozier, and J. Frew, Automated basin delineation from digital elevation data, *Geo-Process., 2*, 299-311, 1984.

O'Loughlin, E. M., Prediction of surface saturation zones in natural catchments by topographic analysis, *Water Resour. Res., 22*, 794-804, 1986.

Olyphant, G. A., Insolation topoclimates and potential ablation in alpine snow accumulation basins: Front Range, Colorado, *Water Resour. Res., 20*, 491-498, 1984.

Olyphant, G. A., Longwave radiation in mountainous areas and its influence on the energy balance of alpine snowfields, *Water Resour. Res., 22*, 62-66, 1986.

Proy, C., Integration du relief au traitement d'images de tele detection, Ph.D. Thesis, 173 pp., Inst. Natl. Polytech. de Toulouse, 1986.

Siegel, R. and J. R. Howell, *Thermal Radiation Heat Transfer*, 2nd ed., 862 pp., McGraw-Hill, New York, 1981.

Unsworth, M. H., Long-wave radiation at the ground. II. Geometry of interception by slopes, solids and obstructed planes, *Quart. J. Royal Meteorol. Soc., 101*, 25-34, 1975.

Williams, L. D., R. G. Barry, and J. T. Andrews, Application of computed global radiation for areas of high relief, *J. Appl. Meteorol., 11*, 526-533, 1972.

Zecharias, Y. B. and W. Brutsaert, Ground surface slope as a basin scale parameter, *Water Resour. Res., 21*, 1895-1902, 1985.

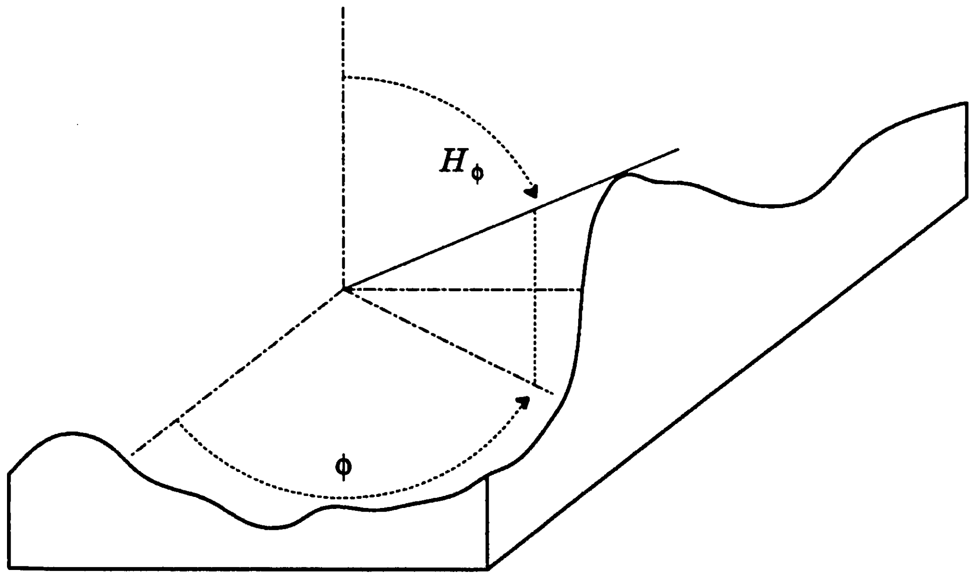

Figure 7.1. Horizon angle H_ϕ for direction ϕ.

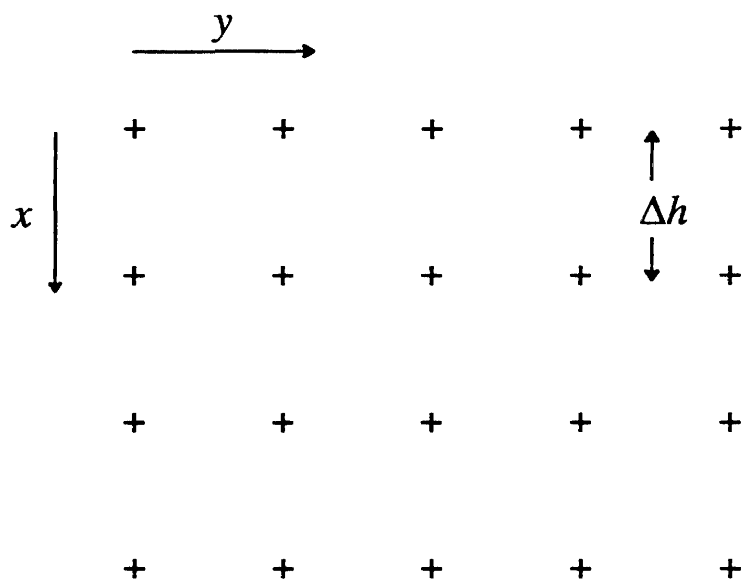

Figure 7.2. Orientation of digital elevation model, showing direction of x and y coordinates and spacing Δh

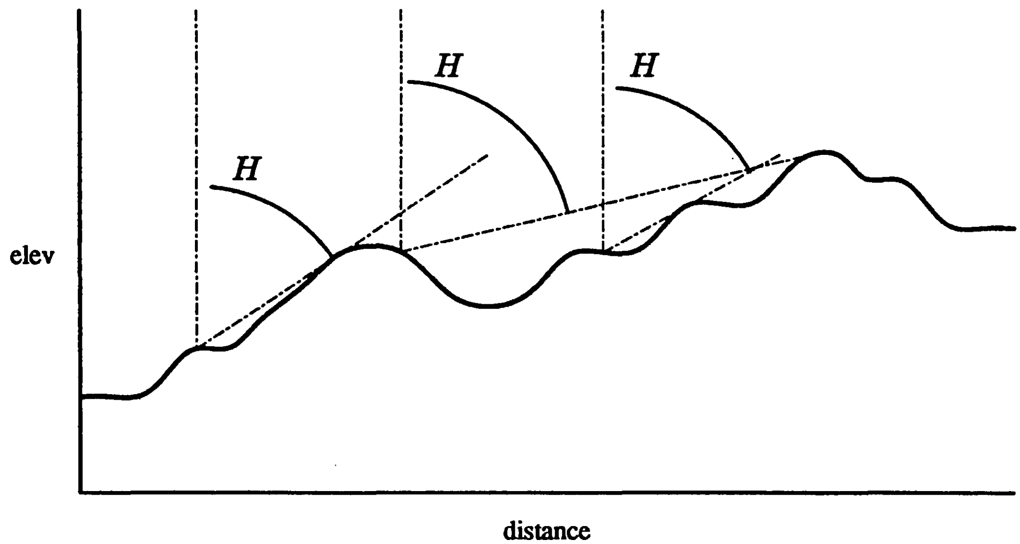

Figure 7.3. A single horizon profile showing the horizon angle H in the forward direction for three points.

8. Snow Accumulation and Distribution

8.1. Introduction

One of the principal properties of concern in snow hydrology is snow water equivalence (SWE), the depth of water at a point that would result if the snow were melted. SWE may be estimated by multiplying the depth by the mean density so

$$\mathrm{SWE} = \frac{\int_0^z \rho_s(z')dz'}{\rho_w}, \qquad (45)$$

where:

ρ_s = density of snow layer (kg m^{-3}),
ρ_w = density of water (kg m^{-3}),
z' = depth of snow layer (m),
z = depth of snowpack (m),

and mean density is defined as

$$\bar{\rho} = \rho_w \frac{\mathrm{SWE}}{z}. \qquad (46)$$

With the use of both established and recently-developed techniques, SWE measurements at a given location are not difficult to obtain. Accurate methods, using precision equipment to measure density, exist in many forms, ranging from those involving excavation and sampling pits [Perla and Martinelli, 1978] to the isotope-profiling gauge [Kattelmann et al., 1983]. The persistent question is: how do we accurately estimate the total volume of water stored in the snowpack over an entire drainage basin? Snowpack properties may vary greatly over small distances. Numerous studies have been conducted in prairies or regions of mild relief, and snowpack variation in these places is relatively well understood. Spatial and temporal variations of snow cover in alpine regions are not well understood. The differences in factors contributing to variation in SWE over gentle terrain (slope, aspect, elevation, vegetation type, surface roughness, energy exchange, etc.) are exaggerated in alpine areas. The result is a heterogeneous snowpack that changes markedly in space and time.

Logistical problems have limited research in alpine areas. Field personnel must cope with difficult access, cold temperatures, inclement weather, and avalanches. Equipment must operate at cold temperatures and through repeated freeze-thaw cycles. A few instrumented alpine sites with excellent data records for a several square meters exist [Martinec, 1970; Davis and Marks, 1980; Davis et al., 1984], but they offer little information about the spatial variability of the measured parameters. In the alpine environment, extrapolation of point data over short distances may not be reliable.

Energy-balance snowmelt models perform adequately at a well-instrumented site, but their use in hydrologic forecasting requires calculation over a drainage basin. Spatial characteristics of the basin and meteorological data can be included as an input, but spatial characteristics of the snowpack are also necessary. We usually lack such information.

Clearly, there is a need for a sampling method that can capture snowpack variability and characterize it over an area, that has reasonable time and manpower requirements, and yet accurately assesses the snowpack. A brute force approach of massive, high-resolution sampling is seldom practical, given constraints of safety and money. We have been able to assemble teams for large surveys as part of this study as the necessary manpower was available. Snow depth and density measurements were obtained in four intensive snow surveys during the 1986 melt season, providing a large spatial sample of point measurements that could be used in model development and testing.

8.2. Previous Work on Snow Distribution

Investigations on snow accumulation and distribution in the last two decades have focused on elevation, vegetation, and topography (Table 8.1). Meiman [1968] summarizes many of the earlier studies. Although much of the work has been done in regions of low elevation and minimum relief, many of the results appear to apply to alpine areas. Even in regions with gentle terrain and low altitude, snow accumulation increases with elevation [Logan, 1973; Steppuhn and Dyck, 1974; Storr and Golding, 1974; Dickison and Daugharty, 1979; Dingman et al., 1979]. Rhea and Grant [1974] point out that the orographic effect is not simply due to change in elevation of an air mass, but also to the rate of change, which is a function of the land-surface slope and the speed of the air parcel. Woo [1973] argues that elevation affects net snow accumulation because melting levels move up and down resulting in alternating accumulation and ablation at a point. Some points will remain above the melting elevation while others are more frequently below. Dingman et al. [1979] found a relationship between SWE and elevation, but poor correlation between density and elevation. Both relationships improved into the season as variance in density decreased. Meiman [1968] found that while elevation and aspect are important, year-to-year variability, and within-year variability in atmospheric conditions may be more important. Aspect is identified as important primarily because of melt influence. Meiman indicates that there is a large variance in the elevation/SWE relationship between different physiographic areas and there are important spatial and temporal differences within homogeneous areas. This means simple relationships are not consistent between regions and in homogeneous areas the relationships may change over short distances and over time.

Many studies have examined the relationship between snow accumulation and terrain features and vegetation. Steppuhn and Dyck [1974] observed recurring distributions of depth, mean density and SWE for similar topography, vegetation, and land use, on three different scales: regional, local, and micro. The regional scale includes climatic effects; the local scale includes topography and vegetation; the micro scale is of the order of a few meters and includes surface roughness and soil temperature, among others. Slope was the most important parameter at the local scale. Adams [1976] discovered that snow distribution and retention in Ontario could best be described by seven different vegetation types. Granberg [1979] noted that terrain roughness on all scales (small vegetation to large topographic features) affects snow accumulation. This effect diminishes as accumulation reduces the roughness at a particular scale. Dickison and Daugharty [1979] found both elevation and forest type to have a significant relationship with snow depth in an eastern Canadian basin with small relief. Terrain type plays a more important role than elevation in the high arctic basins [Woo and Heron, 1979]. With the exception of Rhea and Grant [1974], none of the above studies were conducted in alpine areas.

Elevation has also been shown to be important in subalpine and alpine regions. Glaciologists have used estimates of SWE between discrete elevation bands for glacier mass balance studies [Andrews, 1975]. Engelen [1973], Caine [1975], and Young [1974] all report a positive linear relationship between elevation and SWE. Rhea and Grant [1974] found this relationship to be true for long-term seasonal means, but only for points on the same ridge. Grant and Rhea [1974] and Dexter [1986] studied the effect of elevation on the density of new snow in Colorado. Grant and Rhea found that other factors (upper wind direction, wind speed, air temperature) may be just as important as elevation. Dexter found no systematic relationship between new snow density and aspect or elevation, but did find that site exposure affects bulk snowpack density.

Most of the studies in alpine areas are regional examinations, rather than studies of specific basins, but several notable exceptions exist. Alford [1973] studied cirque glaciers in Colorado and examined the effect that elevation and cirque orientation had on the winter and summer mass balance. He found that elevation was insignificant over the ranges studied, but that a large portion of the winter and summer balances could be explained by the orientation of the cirque because of two directionally dependent factors: wind redistribution of snow and incoming solar radiation. Alford noted a "striking qualitative similarity" between maps of ablation patterns and solar irradiance on the glaciers. Field observations also indicated that redistribution by wind was a critical factor in spatial distribution patterns. In suggesting further work, Alford speculates that better results may be obtained by partitioning the glaciers or cirques into subunits and examining them on a finer scale, and he recognized that a major portion of this endeavor would be the optimal division of the original unit into smaller units.

Young [1974, 1975], working on the Peyto Glacier, Alberta, found elevation, local relief, and slope angle to be important factors in regressions against snow depth. Using a DEM with 100-m spacing, local relief was calculated as the height in meters of a central point, above or below the best-fit regression plane of its four nearest neighbors. Slope angle and local relief were the most important predictor variables in the stratified random sample test, but elevation caused the regression equation to over predict snow depth at high elevations in the nonstratified sample. This appears to be the first study to use a DEM to calculate terrain characteristics for snow accumulation studies.

Haston et al. [1985], working in the same basin as our study, explained snow distribution using elevation, and "southness" ($\sin S \cos A$) and "westness" ($\cos S \cos A$) as measures of slope (S) and aspect (A). Her results showed a poor relationship between elevation and snow accumulation, as most of the basin is above timberline, but the slope angle and aspect parameters provided useful relationships. However, lack of a DEM on which to register survey data precluded conclusive results from this study.

It can be seen from the above mentioned studies that few were conducted in rugged alpine areas. Rather, references are made to the inadequacy of attempts to characterize the extreme SWE variability found in these regions [Bernier, 1986].

8.3. Measurement of Snow-Water Equivalence

Measuring the snow-water equivalence on a snow board or on the ground is fundamental to any estimate of snow deposition volume. Methods using precision equipment to measure snow density from excavation and sampling in snowpits are described by Perla and Martinelli [1978]. Depth measurement is straightforward at a point. Virtually all techniques require determination of the mass of an extracted sample of snow volume from the snowcover, though there are a variety of methods to do this.

SWE was initially sampled on snowboards or in snowpits using a sharpened PVC tube. Depth of each of several samples was noted, and all samples were carefully weighed. Density and SWE were then calculated from the average depth and mass of the samples. This method showed a large variance between pairs of samples, especially when snow densities were low, or when ice lenses or frozen layers were present. The method was abandoned in early winter except for snowboard samples of deposition events less than 20 cm. For larger deposition events or for snow pit measurements, the method used to measure SWE at a point involved use of a 1000 cm^{-3} density cutter designed specifically for use in the Sierra Nevada. Table 8.2 presents the expected data range, instrumentation and estimated data precision of physical snow measurements. The precision of the density cutter is based on a comparison of 54 pairs of density profiles made throughout the Sierra Nevada that showed a mean density difference between profiles of 3.2%, with a standard deviation of 3.1%. Snow depths in this comparison ranged from 20 cm to 6.0 m, and densities from 65 to 650 $kg\,m^{-3}$.

8.4. Factors Affecting Snow Distribution

In order to understand the variable distribution of the snow cover, it is necessary to understand the processes controlling distribution. Properties of the snowpack (e.g., depth, density, temperature, chemistry) vary in space and time. Snow depth and density are controlled by both accumulation and ablation. On a large scale, these processes are controlled by meteorological patterns and major terrain features, and on a small scale by redistribution, new snow properties and micrometeorology. Accumulation consists of two processes: snowfall itself and redistribution of the original snowfall by wind transport or by sloughing and avalanching in areas with sufficient slope. Ablation occurs by melting, sublimation, and deflation.

Variability in both depth and density must be considered in evaluations of snow distribution. Density measurements involve excavating snowpits and sampling the pit wall, which is labor intensive and time consuming. Conversely, depth measurements simply involve probing, and a large number of samples may be taken in the time required to dig a single pit. Depth varies more than density in alpine areas, so the major source of variation in SWE is variation in depth, especially during melt season. Fortunately, this makes field sampling feasible since many easily obtainable depth measurements can be combined with a smaller number of density profiles. A good sampling scheme requires that the number of depth and density measurements be proportional to the parameter variances [Goodison et al., 1981]. Prior to the onset of melt, density exhibits considerable spatial variability, and measurements throughout the entire drainage area are needed to characterize this variability. SWE estimates are then computed from depth measurements, using an interpolated value for density. Ripening of the snowpack before runoff leads to more homogeneity, with less variation in grain size or density because large grains grow at the expense of smaller ones [Colbeck, 1982, 1983; Marsh, 1987]. Once the snowpack is ripe, fewer samples are necessary to characterize the density variation [Hasholt, 1973; Logan, 1973; Adams, 1976].

It is difficult to predict the date at which the snowpack will become ripe, and the entire basin does not ripen simultaneously. It is also difficult to determine the date of peak accumulation. Because an estimate of peak SWE is desirable for prediction of total expected runoff, it is necessary to periodically survey the entire watershed during the winter and spring to ascertain the "cold content" of the pack (the amount of heat needed to raise its temperature to 0° C) and the variability in density and depth over the basin. Waiting to survey until the basin is thought to be ripe may result in missing peak accumulation.

Accumulation

Snowfall. There are several reasons for irregular snowfall in alpine environments. Regional climate and latitude affect snowfall, but are not important at the scale of most alpine basins. In large basins, where elevations differ by several thousand meters and distances within the basin are on the order of kilometers, local basin climate may vary to some degree [Alford, 1973]. Air temperature and vapor pressure control snow crystal morphology [LaChapelle, 1969; Perla and Martinelli, 1978] and therefore control new snow density. Wind affects the amount of fragmentation crystals undergo during and after deposition, and heavy fragmentation leads to high density of new snow. Elevation is considered the single most important factor in snow cover distribution by most of the studies cited in Table 8.2, but the relationship is not independent of climate or slope. Orographic effects depend on slope and wind speed, rather than elevation. Rhea and Grant [1974] found a positive relationship between the topographic slope of the 20 km upwind fetch and long-term, average precipitation. Snowfall also depends on the number of upstream barriers able to deplete the moisture supply of the air mass.

Redistribution. Redistribution accounts for a large portion of the spatial heterogeneity of basin snow cover in alpine regions. Even if snowfall were the same over an area, the final deposition pattern would be highly irregular, because snow is typically moved by wind and redeposited during and after the precipitation event. The low density of the deposited snow, and large surface area of many flakes compared to their mass, allows transport over irregular terrain and large areas. Variation in storm patterns and wind direction further complicate the problem.

Recently, much work has been done on blowing snow, because of its economic effects [reviewed by Schmidt, 1982a]. Snow may be transported by wind-induced creep, saltation or entrainment into the air mass [Mellor, 1965; Radok, 1977; Schmidt, 1980]. Blowing snow is a two-phase process where ice crystals represent the solid phase and air represents the fluid. It becomes a three-phase process when solids sublimate to vapor during transport. Saturation is reached when the air cannot carry more solid load. This state is seldom reached in rugged topography because barriers are spaced too closely and effectively trap solid load. Estimates for the fetch necessary to reach saturation are between 200 and 500 m.

In order for snow on the ground to become entrained, electrostatic forces, surface tension and ice bonds must be overcome. Only exceptional winds are capable of entrainment in maritime climates where well-bonded surfaces develop rapidly. Because of saltation, however, the impact of crystals hitting the surface may dislodge other crystals and allow them to be redistributed where the surface is not too well-bonded and there is a source of impact crystals from snow collected in trees, surface hoar or newly precipitated snow [Martinelli and Ozment, 1985].

Dyunin and Kotlyakov [1980] differentiate between storm types and their depositional characteristics. Upper snow storms are those in which snow falls without further transport. Deflation snowstorms do not contribute new precipitation but move previously deposited snow by saltation. Suspension snow storms are similar to deflation storms, but the previously deposited snow is entrained into the airmass by turbulent diffusion. Deflation storms are capable of drift and cornice formation on lee slopes and ridges, while upper storms have the ability to transport large volumes of snow into belts on lee slopes.

Like other sediments [cf. Bagnold, 1966] snow tends to accumulate in areas where air decelerates or flow is divergent, and it tends to erode in areas of acceleration or convergent flow. Föhn [1980], Schmidt [1984], and Schmidt et al. [1984], found maximum drift flux on an alpine ridge to be on the upwind side within a few meters of the crest, with scoured areas on windward slopes and deposition on lee slopes. Small disturbances in airflow lead to drift formation. Deflation hollows form adjacent to objects such as trees or boulders while immense drifts lie nearby. Largely due to the works of Mellor [1965], Schmidt [1980, 1982b, 1984], Schmidt et al. [1984], Tabler [1985], and Anno [1985, 1986], snow drift over simple uniform barriers is well understood. Where terrain irregularities and wind patterns are consistent in time, drifts and scoured areas tend to repeat in form and location, year after year. However, the problem is considerably more difficult and remains largely unresolved for complicated three-dimensional terrain found in alpine areas. Drifts may shift between storms as the storm track changes. Over a season, consistent patterns still often emerge. This appears to be the case at Emerald Lake.

Avalanches. Considerable volumes of snow may be moved by avalanches in a watershed. Regions in upper parts of basins accumulate snow in avalanche starting zones and when released, the snow is transported downslope to a resting point. Additional snow in the track or runout zone may be entrained and redeposited by the moving mass. Snow may repeatedly slough from slopes that are sufficiently steep, or at low temperatures where metamorphic bonding processes are slow. Avalanching and sloughing have been shown to be important in the nourishment and mass balance of glaciers [Tushinsky, 1975]. Alford [1973] identified cirque glaciers in Colorado nourished almost entirely by avalanches, although most were due to a combination of avalanching and drifting snow.

Avalanching does not change the total mass of snow in a drainage basin, but it is hydrologically important to correctly estimate the volume in these deposits because they may contain large amounts water. Zalikhanov [1975] found that 30 to 64% of the alpine snow cover in the Caucasus may be transported to valley bottoms by avalanches. The retarded melt rate due to increased depth in the deposits may be offset by the increase in energy available to melt the snow at lower elevations. Iveronova [1966] and Sosedov and Seversky [1966], working in the Zailiysky Alatau of Russia, showed that displacement of snow to valley bottoms retarded melt and attenuated peak runoff. Martinec and de Quervain [1975] found that accelerated melt and increased runoff in the early season from avalanche deposits attenuated the peak seasonal discharges in the Dischmatal, Switzerland.

Accumulation and Redistribution at Emerald Lake

Accumulation at Emerald Lake during the 1986 water year has already been discussed in a previous section of this report, however, a discussion of redistribution is in order. There is visible evidence for snow redistribution in the Emerald Lake watershed. Large cornices form on the uppermost ridges and generally face into the basin. These may be formed during southeasterly storms (the basin faces north) or may be the result of considerable erosion and scouring of the hillslopes outside the basin. Other large storms in the basin are northwesterly and travel up the basin, leaving large upslope drifts on the pronounced benches. These drifts account for a significant amount of deposition and are ubiquitous in this particular watershed, both in years of high and low precipitation. Most redistribution occurs during or immediately following the precipitation event.

Most storms are associated with air temperatures near the melting point. At these high temperatures metamorphic processes (sintering) are rapid and result in a strong well-bonded surface. Snow deposited in the few trees in the basin quickly melts and surface hoar is an anomaly here, thus, the only likely source for impact crystals is newly precipitated snow. During and immediately following a storm, the loose snow may be easily moved and even disaggregate the old snow surface, incorporating dislodged crystals into the redistribution. Once the surface develops, little snow movement takes place even in high winds and the majority of snow loss under these conditions is from sublimation.

Many of the snow patches that persist for the longest period into the melt season in the Emerald Lake watershed are avalanche deposits or snowbanks found at the foot of steep cliffs fed by sloughing from above. The February storm mentioned above produced excessive accumulation over a short period of time and led to a large avalanche cycle which moved a large portion of snow from mid-elevation in the basin to the lake surface. Depths of drifts and avalanche deposits during the 1985/1986 season sometimes exceeded 10 m, and sloughing from steep rock faces produced many depths exceeding 8 m.

With the exception of the cornices and drifts described above, the snow cover smooths the Emerald Lake basin features. This happens on a small scale, including talus and small boulders, and on a larger scale, including gullies, depressions and large boulders. All but the very largest boulders were obscured completely during the 1985/1986 winter.

Ablation

A common method to evaluate ablation, snowmelt and energy exchange is through the energy balance equation. Snowpack ablation is controlled by energy exchanges at the air/snow and snow/ground interfaces. Energy inputs may come from solar and emitted atmospheric radiation R, sensible heat exchange H, latent heat exchange LE, heat flux from the underlying substrate G and advective heat transfer M. This relationship has been studied extensively for snow [de La Casinière, 1974; Anderson, 1976; Price and Dunne, 1976; Granger and Male, 1978; Obled and Harder, 1979; Male and Granger, 1981] and is usually summarized in the following equation where ΔQ is the net energy exchange.

$$\Delta Q = R + H + LE + G + M \qquad (47)$$

If ΔQ is less than zero the snowpack is losing energy. A positive ΔQ raises the temperature of the snowpack or produces melt if the temperature is already at 0°C. Chapters 9 and 10 discuss calculation of the snowpack energy exchange in the Emerald Lake basin.

Of the available energy sources, it is well documented that in most cases solar and longwave radiation (R) dominate [Zuzel and Cox, 1975]. Turbulent transfer processes (LE and H) are important in snowmelt in some conditions, but are usually of the opposite sign. Values for these exchanges are difficult to derive and the processes driving them, such as wind, are highly stochastic. Even with sophisticated instrumentation it is difficult to accurately estimate their contribution to melt. Advective heat transfer (M) is small, especially at the high elevations of the southern Sierra Nevada. Energy exchange through the ground/snow interface (G) is important in some cases, such as areas with higher than normal geothermal exchange, but this energy is usually negligible in comparison to surface exchanges [Davis, 1980].

Heat flux from the ground may control accumulation at the onset of winter by melting snow as it falls on the surface. This is dependent on the thermal and optical properties of the substrate. Areas capable of absorbing and storing significant amount of energy will melt snow. These are typically areas with a low albedo and high heat capacity. The effect may carry into the winter on features too steep to accumulate snow. The energy absorbed may be re-emitted as longwave radiation and melt out depressions around the features. Olyphant [1986a] found that radiation re-emitted from exposed rock faces reduced net longwave losses by 37% to 63% in Colorado.

More importantly, radiation affects accumulation through melt at the surface. If the melt only percolates into the snowpack and refreezes, then depth and density have changed but SWE has not. Once meltwater reaches an ice lens or the ground, however, it may move horizontally and the SWE at that point will change. Radiation thus influences the spatial element of accumulation as it may effectively remove SWE from discrete parts of the basin where the energy budget is sufficient.

Melt water production can take place only once the pack is locally isothermal at 0°C. It is important to note that it is not necessary for the entire pack to be ripe in order to produce melt, because of the thermal diffusivity and conductivity of snow. Further, it is important to note that production of surface melt does not necessarily lead to runoff. Surface melt may take place and percolate down into an unripe portion and refreeze where the energy necessary to maintain the liquid phase is no longer sufficient. At this point the latent heat of fusion is released and the pack temperature is raised a corresponding amount. This is thought to be a principal method of ice lens formation. Ice lenses may also be formed when liquid water encounters a layer of reduced permeability, a buried surface lens, wind slab, etc., and tends to pond and spread out horizontally on the incongruity. Refreezing may then take place, leaving an ice lens. This is a common scenario in the Sierra and other maritime snow environments and is a principal method of ripening or removing the cold content. In maritime environments this occurs throughout the season, while in continental snowpacks it is primarily a springtime phenomenon.

In predicting areas of melt for a given set of conditions it is necessary to examine a number of factors. Besides the basic energy balance equation components, it is necessary to look at the different physiographic characteristics of the point in question. Factors such as slope, aspect, latitude and horizon must be taken into account, especially in rugged terrain. In locations where radiation inputs are relatively low (high latitude), melt and rainfall tend to have a uniform effect on the snow cover [Adams, 1976]. In areas where the radiation budget is both important and variable (lower latitudes and high elevations with rough topography) it has the effect of increasing the variability in snowpack parameters. Some areas may go several months in the winter without receiving direct solar radiation. Adjacent areas may receive large amounts of direct radiation and experience variable melt throughout the winter season. Many of the studies in snowmelt have been carried out in prairie or arctic environments where terrain features are homogeneous [Pysklywec et al., 1968; de La Casinière, 1974; Granger and Male, 1978; McKay and Thurtell, 1978; Woo and Heron, 1979]. In these cases is it adequate to apply a single value of irradiance to the entire study area. Other studies have applied energy budgets to different topographical units within a single basin [Price and Dunne, 1976; Obled and Harder, 1979]. Recently the problem of applying these results to rugged terrain has received more attention [Dozier and Outcalt, 1979; Marks and Dozier, 1979; Dozier, 1980; Olyphant, 1984, 1986b].

8.5. Field Methods

An exhaustive field measurement program was undertaken to measure SWE in the Emerald Lake basin. The program resulted in excavation of numerous pits and hundreds of depth measurements over the basin which served two purposes: measurements could be used as an input to the accumulation model and could be used to validate the results.

Random sample survey points were selected on a 25 meter grid overlain on the 5 meter resolution DEM grid. A stratified random sample is preferred for statistical reasons [Cochran, 1977] and for increased efficiency in the field, and has been applied to snow surveys [Young, 1974; Leaf and Kovner, 1972; Steppuhn and Dyck, 1974; Adams, 1976; Woo and Marsh, 1978]. In this study, however, the survey data were used in our classification, and stratifying the basin before the surveys were completed would have defeated the purpose.

Four surveys were completed starting at the peak accumulation in the basin and following at approximately one month intervals thereafter. The first survey covered only about one fifth of the watershed due to the extreme avalanche danger over much of the area at that time, but the other three surveys encompassed the entire basin. Some of the generated points fell on locations that were either too difficult for the survey teams to reach or were located on rock outcrops or cliffs. These points were discarded if they appeared to have any snow on them since accurate estimate from afar was not possible, but the point was retained and a depth of zero recorded if it could be positively determined that the point was located on rock. About 100 points were sampled in the first survey and 180 points for each survey thereafter. Locations of the points were transferred to a set of orthographically corrected aerial photographs.

The field teams used these orthographic photographs, topographic maps, close-up photos and compasses to locate the points in the field. The photographs were of extremely high quality and resolution and they were overlain with a 5 m interval contour map before printing. Combined with the many distinguishable features in the basin, these enabled precise location of points. At each location the survey team recorded aspect, slope angle, and snow depth at the point as well as depths 4 m away in the four cardinal directions. The five depths were then averaged to minimize local variation of depth, caused by underlying boulders. Slope angle and aspect were obtained using compasses, and depths were found using interlocking aluminum probes usable up to 10 m depth. At depths greater than 10 m, friction and icing on the probes made it impossible to obtain a sample. Slope angle and aspect observations were used only as a check on location. The values for these variables were calculated from the DEM for data analysis.

Snow pits were dug at selected sites throughout the watershed to obtain density and temperature profiles. Pit locations were retained for each survey to minimize labor efforts because several of the pits exceeded 6 m depth. The pit wall was excavated inward to a point which had not been subjected to the environmental changes induced by previous sampling margins. Density was measured by two techniques which have been discussed previously in this report.

Snow covered area was estimated from many of oblique photographs obtained during the surveys and throughout the melt season. The nature of the basin topography allowed us to get adequate views of nearly the entire watershed from opposing ridges. Aerial overflights were not effective due to cloud cover during some of the surveys and difficulty in getting commercial aerial photography companies to comply with our needs. However, two overflights were successful between survey periods and these were useful for reference.

8.6. Preliminary Results

It is possible to estimate the basin SWE simply from the mean of depth and density the values obtained from the snow surveys when the sample size is large enough. The sample size of depth measurements exceeded 125 in all but the first survey, where it was 86. Density did not vary appreciably through the entire melt season with a mean of 520 kg m^{-3} and a standard deviation of 44.0 kg m^{-3}. The small deviation allowed us to apply the mean density value to all depths to obtain SWE estimates. Statistics on the depth measurements from the four surveys are summarized in Table 8.3. The relatively low depth variance in the April survey data is an artifact of the sample distribution; only a small, relatively homogeneous portion of the basin was sampled, for safety reasons. The basin mean snow water equivalence ($\overline{SWE}$) was obtained by multiplying the mean snow depth by the mean density for each survey date. Total volume of water stored in the basin was calculated by multiplying the total basin area by $\overline{SWE}$ and results from all four surveys are listed in Table 8.4. Snow covered area was implicitly accounted for in the calculations because the survey points without snow were averaged into the mean snow depth. Again, with a large, randomly located sample, this procedure should be sufficient.

Some justification is necessary for using snow depths from the subsample of the basin obtained in the first survey to represent the entire basin. The first survey covered only the northeast wall of the basin. Early season effects of radiation on the spatial distribution of snow in the basin appear to be negligible. At this time the energy budget is small and the energy budget difference between points within the basin is minimal. As the season progresses and the sun angle changes, some portions of the basin receive a great deal more energy than others. Significant ablation may take place in some areas of the basin before melt is initiated in others, leading to increased variation in SWE. To characterize this difference through time, an ANOVA was used to test the means of depth from the northeast wall against the means from the entire basin for the second, third, and fourth surveys. The null hypothesis was stated as follows: there is no difference between the mean depth for the northeast wall and the mean depth of the entire basin. An F test showed, at the 5% significance level, that there was no difference in $\overline{SWE}$ for the locations in either the second or third survey, and that the means for the subarea fell well within the 95% confidence intervals for the entire basin. The null hypothesis was rejected for the fourth survey, indicating that the northeast wall was no longer representative of the entire basin. The mean and variance of the three surveys can be found in Table 8.5 and the results from the F tests are listed in Table 8.6. Based on these results, it was possible to obtain a reliable estimate of basin $\overline{SWE}$ for the first survey date using the data available from the northeast wall. The mean from this survey was applied to the entire basin to calculate the values for the first survey in Table 8.5.

This is an important result because this survey was completed close to the date of maximum accumulation and preceded any significant ablation. The total amount of water stored in the basin at this time is an important value to other facets of the project. Due to the relatively large sample sizes and the field techniques employed, we have confidence in the values presented in Table 8.4. As stated above, these large surveys are seldom practical and new techniques must be developed to obtain a similar degree of accuracy with a reasonable time, manpower, and economic investment. Some possibilities toward this end are presented below.

8.7. Future Work

The objective of this portion of the project is to develop a model of snow distribution in an alpine basin based on topographical parameters that account for variations in both accumulation and ablation, by identifying and mapping zones of similar snow properties. These zones will be delineated using the DEM and the extensive data base of snow properties now existing from the surveys. Topographical parameters will be used in zone calculations, including elevation, slope, rate of change in slope, aspect, and an index of radiation. The radiation index will be total daily beam radiation summed for selected days prior to the survey date, calculated by the methods described elsewhere in this report. All of the parameters mentioned, with the exception of radiation, can be considered stationary in time. Clearly, snow distribution in rugged terrain does not change uniformly in space over time. The radiation index will change through time and should produce a meaningful relationship with snow distribution. This may prove to be the best parameter for snow distribution in the Emerald Lake basin because it is the most reasonable physically based index. Although other physically based indices are being tested, such as elevation, slope and aspect, they may not be important on the scale of the Emerald lake basin. Haston et al. [1985] found poor correlations between snow depth and slope, exposure, southness and westness in the basin. Elevation was not tested because the DEM was not yet available. The improved accuracy attained in the present study may produce different results, but more analysis is necessary before conclusions may be drawn.

Analysis will be carried out using the statistical package "S" [Becker and Chambers, 1984] and the newly developed image processing software "IPW" [Frew and Dozier, 1986]. Images of the parameters described above have been constructed using IPW software.

The images will be randomly sampled and combined with the points from the 1986 water year surveys for which SWE data exists. This test group will be clustered and the results used for classification of the entire watershed. The classification results will then be tested using standard statistical procedures until an optimal classification is reached. These results will then be applied to the 1987 water year survey results for similar analysis. In the 1988 water year, one intensive random survey will be carried out at peak accumulation simultaneously with a stratified random survey designed from the results of the present study. This will provide a third year of testing the distribution model with the intensive surveys as well as an opportunity to test the optimal survey against an intensive one. This should provide information on the usefulness of the entire approach and indicate whether it has potential for application beyond the present study.

8.8. References

Adams, W. P., Areal differentiation of snow cover in east central Ontario, *Water Resour. Res.*, *12*, 1226-1234, 1976.

Alford, D. L., Cirque glaciers of the Colorado Front Range: mesoscale aspects of a glacier environment, *Ph. D. Thesis*, 198 pp., Univ. Colorado, Boulder, 1973.

Anderson, E. A., A point energy and mass balance model of a snow cover, *NWS Tech. Rep. 19*, 150 pp., NOAA, Washington, DC, 1976.

Andrews, J. T., *Glacial Systems; an Approach to Glaciers and Their Environments*, 191 pp., Wadsworth, Belmont, CA, 1975.

Anno, Y., Development of a snowdrift wind tunnel, *Cold Regions Sci. Technol.*, *10*, 153-161, 1985a.

Anno, Y., Froude number paradoxes in the modeling of a snowdrift, *Cold Regions Sci. Technol.*, *10*, 191-192, 1985b.

Bagnold, R. A., An approach to the sediment transport problem from general physics, *Prof. Pap. 422-I*, U.S. Geol. Survey, Washington, DC, 1966.

Becker, R. A. and J. M. Chambers, *S: An Interactive Environment for Data Analysis and Graphics*, Wadsworth Advanced Book Program, Belmont, CA, 1984.

Bernier, P., Extrapolating snow measurements on the Marmot Creek Experimental Basin, *Nordic Hydrol.*, *17*, 83-92, 1986.

Caine, N., An elevational control of peak snowpack variability, *Water Resources Bulletin*, *11*, 613-621, 1975.

Cochran, W. G., *Sampling Techniques*, 3rd ed., 428 pp., Wiley, New York, 1977.

Colbeck, S. C., An overview of seasonal snow metamorphism, *Rev. Geophys. Space Phys.*, *20*, 45-61, 1982.

Colbeck, S. C., Snow particle morphology in the seasonal snow cover, *Bull. Amer. Meteorol. Soc.*, *64*, 602-609, 1983.

Davis, R. E., Simulation of an alpine soil thermal regime beneath a snowpack, M.A. Thesis, 60 pp., Dept. Geogr., Univ. Calif., Santa Barbara, CA, 1980.

Davis, R. E., J. Dozier, and D. Marks, Micrometeorological measurements and instrumentation in support of remote sensing observations of an alpine snow cover, *Proc. Western Snow Conf.*, *51*, 161-164, 1984.

Davis, R. E. and D. Marks, Undisturbed measurement of the energy and mass balance of a deep alpine snowcover, *Proc. Western Snow Conf.*, *48*, 62-67, 1980.

Dexter, L. R., Aspect and elevation effects on the structure of the seasonal snowcover in Colorado, Ph. D. Thesis, 228 pp., Univ. Colorado, Boulder, CO, 1986.

Dickison, R. and D. Daugharty, A square grid system for modeling snow cover in small watersheds, in *Proceedings, Modeling Snow Cover Runoff*, edited by S. C. Colbeck and M. Ray, pp. 71-76, U.S. Army Cold Regions Res. Engrg. Lab., Hanover, NH, 1979.

Dingman, S. L., E. Henry, and R. Hendrick, Variation of snow properties with elevation in New Hampshire and Vermont, in *Proceedings, Modeling Snow Cover Runoff*, edited by S. C. Colbeck and M. Ray, pp. 93-100, U.S. Army Cold Regions Res. Engrg. Lab., Hanover, NH, 1979.

Dozier, J., A clear-sky spectral solar radiation model for snow-covered mountainous terrain, *Water Resour. Res.*, *16*, 709-718, 1980.

Dozier, J. and S. I. Outcalt, An approach toward energy balance simulation over rugged terrain, *Geogr. Anal.*, *11*, 65-85, 1979.

Dunne, T., A. G. Price, and S. C. Colbeck, The generation of runoff from subarctic snowpacks, *Water Resour. Res.*, *12*, 677-685, 1976.

Dyunin, A. K. and V. M. Kotlyakov, Redistribution of snow in the mountains under the effect of heavy snow storms, *Cold Regions Sci. Technol.*, *3*, 287-294, 1980.

Engelen, G. B., A graphical and statistical approach to the regional study of snowpack in mountain areas, with a special reference to Colorado and New Mexico, in *The Role of Snow and Ice in Hydrology*, edited by J. C. Rodda, IAHS-AIHS Publ. 107, pp. 885-889, Intl. Assoc. Hydrol. Sci., Wallingford, UK, 1972.

Föhn, P. M., Snow transport over mountain crests, *J. Glaciol.*, *26*, 469-480, 1980.

Frew, J. and J. Dozier, The Image Processing Workbench – portable software for remote sensing instruction and research, in *Proc. IGARSS '86*, ESA SP-254, pp. 271-276, European Space Agency, Paris, 1986.

Goodison, B. E., H. L. Ferguson, and G. A. McKay, Measurement and data analysis, in *Handbook of Snow*, edited by D. M. Gray and D. H. Male, pp. 191-274, Pergamon Press, New York, 1981.

Granberg, H., Snow accumulation and roughness changes through winter at a forest-tundra site near Schefferville, Quebec, in *Proceedings, Modeling Snow Cover Runoff*, edited by S. C. Colbeck and M. Ray, pp. 83-92, U.S. Army Cold Regions Res. Engrg. Lab., Hanover, NH, 1979.

Granger, R. J. and D. H. Male, Melting of a prairie snowpack, *J. Appl. Meteorol.*, *17*, 1833-1842, 1978.

Grant, L. O. and J. O. Rhea, Elevation and meteorological controls on the density of new snow, in *Advanced Concepts and Techniques in the Study of Snow and Ice Resources*, pp. 169-181, Natl. Acad. Press, Washington, DC, 1974.

Hasholt, B., Random sampling technique in measuring snow-water equivalent in a drainage basin, in *Role of Snow and Ice in Hydrology*, edited by J. C. Rodda, IAHS-AIHS Publ. 107, pp. 680-687, Intl. Assoc. Hydrol. Sci., Wallingford, UK, 1973.

Haston, L., D. Marks, and J. Dozier, Mapping zones of similar terrain for an improved estimate of snow volume and chemical loading over an alpine watershed, *Eos, Trans. Amer. Geophys. Union*, *66*, 889, 1985.

Iveronova, M. I., Le rôle hydrologique des avalanches, in *Scientific Aspects of Snow and Ice Avalanches*, IAHS-AIHS Publ. 69, pp. 73-77, Intl. Assoc. Hydrol. Sci., Gentbrugge, Belgium, 1966.

Kattelmann, R. C., B. J. McGurk, N. H. Berg, J. A. Bergman, J. A. Baldwin, and M. A. Hannaford, The isotope profiling snow gage: twenty years of experience, *Proc. Western Snow Conf.*, *51*, 1-8, 1983.

LaChapelle, E. R., *Field Guide to Snow Crystals*, 101 pp., University of Washington Press, Seattle, 1969.

La Casinière, A. C. de, Heat exchange over a melting snow surface, *J. Glaciol.*, *13*, 55-72, 1974.

Leaf, C. F. and J. Kovner, Sampling requirements for areal water equivalent estimates in forested subalpine watersheds, *Water Resour. Res.*, *8*, 713-716, 1972.

Logan, L., Basin-wide water equivalent estimation from snowpack depth measurements, in *Role of Snow and Ice in Hydrology*, edited by J. C. Rodda, IAHS-AIHS Publ. 107, pp. 864-884, Intl. Assoc. Hydrol. Sci., Wallingford, UK, 1973.

Male, D. H. and R. J. Granger, Snow surface energy exchange, *Water Resour. Res.*, *17*, 609-627, 1981.

Marks, D. and J. Dozier, A clear-sky longwave radiation model for remote alpine areas, *Arch. Meteorol. Geophys. Bioklim., Ser. B*, *27*, 159-187, 1979.

Marsh, P., Grain growth in a wet Arctic snow cover, *Cold Regions Sci. Technol.*, *14*, 23-31, 1987.

Martinec, J., Study of snowmelt runoff process in two representative watersheds with different elevation range, in *Results of Research on Representative Experimental Basins, Proceedings of the Wellington Symposium*, pp. 29-39, IAHS/UNESCO, Paris, 1970.

Martinec, J. and M. R. de Quervain, The effect of snow displacement by avalanches on snowmelt and runoff, in *Snow and Ice*, IAHS-AIHS Publ. 104, pp. 364-377, Intl. Assoc. Hydrol. Sci., Wallingford, UK, 1975.

Martinelli, M. Jr. and A. Ozment, Some strength features of natural snow surfaces that affect snow drifting, *Cold Regions Sci. Technol.*, *11*, 267-283, 1985.

McKay, D. C. and G. W. Thurtell, Measurements of the energy fluxes involved in the energy budget of a snow cover, *J. Appl. Meteorol.*, *17*, 339-349, 1978.

Meiman, J. R., Snow accumulation related to elevation, aspect and forest canopy, in *Snow Hydrology, Proceedings of a Workshop Seminar*, pp. 35-47, Can. Natl. Comm. Intl. Hydrol. Decade, Ottawa, Ontario, 1968.

Mellor, M., Blowing Snow, *CRREL Monograph, part 3, section A3c*, 79 pp., U.S. Army Cold Regions Res. Engrg. Lab., Hanover, NH, 1965.

Obled, Ch. and H. Harder, A review of snow melt in the mountain environment, in *Proc. Modeling Snow Cover Runoff*, edited by S. C. Colbeck and M. Ray, pp. 179-204, U.S. Army Cold Regions Res. Engrg. Lab., Hanover, NH, 1979.

Olyphant, G. A., Insolation topoclimates and potential ablation in alpine snow accumulation basins: Front Range, Colorado, *Water Resour. Res.*, *20*, 491-498, 1984.

Olyphant, G. A., The components of incoming radiation within a mid-latitude alpine watershed during the snowmelt season, *Arctic Alpine Res.*, *18*, 163-169, 1986a.

Olyphant, G. A., Longwave radiation in mountainous areas and its influence on the energy balance of alpine snowfields, *Water Resour. Res.*, *22*, 62-66, 1986b.

Perla, R. and M. Martinelli, Jr., *Avalanche Handbook*, Agric. Hbk. 489, rev. ed., 254 pp., U.S. Dept. Agric., Washington, DC, 1978.

Price, A. G. and T. Dunne, Energy balance computations of snowmelt in a subarctic area, *Water Resour. Res.*, *12*, 686-694, 1976.

Pysklywec, D. W., K. S. Davar, and D. I. Bray, Snowmelt at an index plot, *Water Resour. Res.*, *4*, 937-946, 1968.

Radok, U., Snow drift, *J. Glaciol.*, *19*, 123-139, 1977.

Rawls, W. J., T. J. Jackson, and J. F. Zuzel, Comparison of areal snow storage sampling procedures for rangeland watersheds, *Nordic Hydrol.*, *11*, 71-82, 1980.

Rhea, J. O. and L. O. Grant, Topographic influences on snowfall patterns in mountainous terrain, in *Advanced Concepts and Techniques in the Study of Snow and Ice Resources*, pp. 182-192, National Academy of Sciences Press, Washington, DC, 1974.

Schmidt, R. A., Threshold wind-speeds and elastic impact in snow transport, *J. Glaciol.*, *26*, 453-467, 1980.

Schmidt, R. A., Properties of blowing snow, *Rev. Geophys. Space Phys.*, *20*, 39-44, 1982a.

Schmidt, R. A., Vertical profiles of wind speed, snow concentration, and humidity in blowing snow, *Boundary-Layer Meteorol.*, *23*, 223-246, 1982b.

Schmidt, R. A., Measuring particle size and snowfall intensity in drifting snow, *Cold Regions Sci. Technol.*, *9*, 121-129, 1984.

Schmidt, R. A., R. Meister, and H. Gubler, Comparison of snow drifting measurements at an alpine ridge crest, *Cold Regions Sci. Technol.*, *9*, 131-141, 1984.

Sosedov, I. S. and I. V. Seversky, On hydrological role of snow avalanches in the northern slope of the Zailiysky Alatau, in *Scientific Aspects of Snow and Ice Avalanches*, IAHS-AIHS Publ. 69, pp. 78-85, Intl. Assoc. Hydrol. Sci., Gentbrugge, Belgium, 1966.

Steppuhn, H. W. and G. D. Dyck, Estimating true basin snow cover, in *Advanced Concepts and Techniques in the Study of Snow and Ice Resources*, pp. 314-328, National Academy of Sciences Press, Washington, DC, 1974.

Storr, D and D. Golding, A preliminary water balance evaluation of an intensive snow survey in a mountainous watershed, in *Advanced Concepts and Techniques in Study of Snow and Ice Resources*, pp. 294-303, National Academy of Sciences, Washington, DC, 1974.

Tabler, R. D., Ablation rates of snowfence drifts at 2300 meters elevation in Wyoming, *Proc. Western Snow Conf.*, *53*, 1-12, 1985.

Tushinsky, G. K., The part avalanches play in the formation and dynamics of glaciers and snow patches in the territory of the USSR, in *Snow and Ice Symposium*, edited by J. C. Rodda, IAHS-AIHS Publ. 104, pp. 381-389, Intl. Assoc. Hydrol. Sci., Wallingford, UK, 1975.

Woo, M., A numerical simulation model for snow storage in small coastal basins, southwestern British Columbia, in *Role of Snow and Ice in Hydrology*, edited by J. C. Rodda, IAHS-AIHS Publ. 107, pp. 992-1003, Intl. Assoc. Hydrol. Sci., Wallingford, UK, 1973.

Woo, M. and R. Heron, Modeling basin snow storage in a high arctic environment, in *Proceedings, Canadian Hydrology Symposium*, pp. 206-216, Associate Committee on Hydrology, Natl. Res. Council Canada, 1979.

Woo, M. and P. Marsh, Analysis of error in the determination of snow storage for small high Arctic basins, *J. Appl. Meteorol.*, *17*, 1537-1541, 1978.

Young, G. J., A stratified sampling design for snow surveys based on terrain shape, *Proc. Western Snow Conf.*, *42*, 14-22, 1974.

Young, G. J., Accumulation and ablation patterns as functions of the surface geometry of a glacier, in *Snow and Ice Symposium*, edited by J. C. Rodda, IAHS-AIHS Publ. 104, pp. 134-138, Intl. Assoc. Hydrol. Sci., Wallingford, UK, 1975.

Zalikhanov, M. C., Hydrological role of avalanches in the Caucasus, in *Snow and Ice Symposium*, edited by J. C. Rodda, IAHS-AIHS Publ. 104, pp. 390-394, Intl. Assoc. Hydrol. Sci., Wallingford, UK, 1975.

Zuzel, J. F. and L. M. Cox, Relative importance of meteorological variables in snowmelt, *Water Resour. Res.*, *11*, 174-176, 1975.

TABLE 8.1. Previous Studies

Study	Location	Elevation (m)	Dependent Variable(s)	Independent Variable(s)
Meiman [1968]	Reviews previous studies		SWE	elevation, aspect, forest canopy
Leaf and Kovner [1972]	Fraser Experimental Forest and Fool Creek, Colorado	not specified	SWE	elevation
Alford [1973]	Front Range, Colorado	3440-4040	SWE	elevation, cirque orientation
Engelen [1973]	Snow courses in Colorado and New Mexico	not specified	depth, SWE	elevation, topography, vegetation, date, latitude, longitude
Logan [1973]	Wilmot Creek Basin, Ontario	76-373	depth, density, SWE	elevation, season air temperature barometric pressure liquid precipitation
Grant and Rhea [1974]	Snow courses in Colorado	2370-3440	density	geographic location, upper wind direction, wind speed, temperature regime, weather modification
Rhea and Grant [1974]	Colorado and Utah	2700-3400	SWE	elevation, topographic slope of storm approach, number of upstream barriers
Steppuhn and Dyck [1974]	Beir Basin, Yukon; Bad Lake Basin, Saskatchewan; Battle Basin, Alberta	not specified	SWE	terrain, vegetation land use
Storr and Golding [1974]	Marmot Creek Experimental Watershed, Alberta	1585-2805	SWE	elevation
Young [1974, 1975]	Peyto Glacier, Alberta	2100-3200	SWE	elevation, slope angle, local relief
Caine [1975]	San Juan Mountains, Colorado	2650-3500	SWE	elevation
Adams [1976]	Peterborough, Ontario	~220	depth, density, SWE	vegetation
Dickison and Daugharty, [1978]	Nashwaak Experimental Watershed, New Brunswick	195-480	depth, SWE	elevation, slope angle, aspect, vegetation cover, vegetation basal area
Dingman et. al. [1978]	Snow courses in New Hampshire and Vermont	90-760	depth, density, SWE	elevation, date
Granberg [1978]	Timmins 4 Permafrost Experimental Site, Quebec	755-795	SWE	topographic and vegetative roughness
Woo and Heron [1979]	Resolute, Northwest Territories	85-200	SWE	terrain
Rawls et. al. [1980]	Reynolds Creek Experimental Watershed, Idaho	1400-2195	depth, density, SWE,	slope angle, aspect, vegetation, drift vs. non-drift area
Haston [1985]	Emerald Lake Watershed, California	2780-3415	SWE	elevation, slope angle, aspect
Dexter [1986]	Front Range, Colorado	2500-4000	depth, density, SWE	elevation, slope angle, aspect, exposure, date

TABLE 8.2. Measured Physical Snow Properties
(Snowboards and Snowpits)
Emerald Lake Watershed, 1986 Snow Season

Measured Parameter	Range	Instrument	Precision
Snow Temperature T_s	-20 to 0 °C	Digital Thermometer	±0.2°C
Snow Depth z_s	0 to 10 m	Metric Tape	±0.005m
Snow Density ρ_s	65 to 650 kg m^{-3}	PVC Tube	±5–15%
		1000 cm^3 Cutter	±3%
SWE			±5%

TABLE 8.3 Summary of Depth Survey Statistics - 1986 Water Year

date of survey	n	mean depth (cm)	std. dev.	variance
April 15-17	86	384	127	16,128
May 2-5	127	378	219	47,939
May 23-26	157	292	197	38,685
June 24-27	166	107	163	26,528

TABLE 8.4 Summary of Snow Water Equivalent - 1986 Water Year

survey date	mean depth (cm)	mean density ($kg\,m^{-3}$)	SWE (m^3)	total H_2O volume
April 15-17	384	520	200	2,398,550
May 2-5	378	520	197	2,361,080
May 23-26	292	520	152	1,823,900
June 24-27	107	520	56	668,350

TABLE 8.5. Depth Statistics - Entire Basin vs. Northeast Wall (1986)

	entire basin			northeast wall		
survey date	n	mean depth (cm)	variance	n	mean depth (cm)	variance
May 2-5	127	378	47,939	50	357	21,870
May 23-26	157	292	38,655	34	269	13,005
June 24-27	166	107	26,528	42	49	7,727

TABLE. 8.6 F Test Results - Entire basin vs. Northeast Wall (1986)

survey date	May 2-5	May 23-26	June 24-27
F_{est}	0.399	0.453	12.19
$F_{(0.05)(1)(1)(v)}$	3.89	3.89	3.90
accept/reject H_o *	accept	accept	reject
% conf. level	0.001	0.001	0.002
basin mean depth	378.10	292.46	107.43
NE wall mean depth	356.84	268.97	49.29
95% conf. interval for basin mean depth	±38.45	±31.01	±24.95

* see text for desciption of H_o

9. Energy Exchange at the Snow Surface

Snow metamorphism and transport of chemical species in snow are driven by energy exchange at the snow surface. In this chapter we review energy exchange processes at magnitudes in the Emerald Lake watershed.

In a seasonal snowcover, newly fallen snow is thermodynamically unstable, undergoing continuous metamorphism until it melts and becomes runoff during spring [Colbeck, 1982]. These metamorphic changes and final melting are driven by temperature and vapor density gradients within the snowcover, which are caused by heat exchange at the snow surface and at the snow-soil interface [Colbeck et al., 1979; Male and Granger, 1981]. In general, the energy balance of a snowcover is expressed as

$$\Delta Q = R_n + H + L_v E + G + M \qquad (48)$$

where ΔQ is change in snowcover energy, and R_n, H, $L_v E$, G, and M are net radiative, sensible, latent, conductive, and advective energy fluxes. In temperature equilibrium, $\Delta Q = 0.0$; a negative energy balance will cool the snowcover, increasing its cold content (the amount of energy required to bring it to 0.0°C), while a positive energy balance will warm the snowcover. The snowcover cannot be warmer than 0.0°C, and melt cannot occur in significant amounts until the entire snowcover has reached this temperature. In a deep alpine snowcover, liquid water can occur in some layers while others are sub-freezing. This liquid water may re-freeze if it comes in contact with a sub-freezing layer, accelerating the snowcover toward equilibrium, or it may slowly drain from the snowcover if it occurs near the snow-soil interface. Once the entire snowcover is isothermal at 0.0°C, positive values of ΔQ must result in melt.

As shown in Table 9.1, since the U.S. Army Corps of Engineers published their detailed report, Snow Hydrology [USACE, 1956] many detailed and theoretical studies of the snowcover energy balance have been undertaken. These studies took place in a variety of snowcover conditions and locations, and represent very different approaches to measuring or modeling the snowcover energy balance. They all agree, however, that the energy balance approach, when reliable energy exchange data are available, allows accurate snowmelt computations at a point that are physically based and independent of site-specific considerations. The problem is that it is generally not possible to directly measure energy exchange in a natural environment. Each of the energy exchange terms in the energy balance equation is calculated from a combination of measured meteorological parameters and a set of constants and coefficients which reflect our best understanding of the physical and thermodynamic characteristics of the atmosphere, the snowcover, and the soil. At a point, these cannot be measured with complete certainty, and monitoring their variation over a short distance is difficult. Over a small watershed, like Emerald Lake, we must examine the variation of a multitude of properties and processes in time and over a complex terrain surface. We must then generalize these so that our estimates of the input parameters and the physical constants and coefficients, while not exact, provide a reasonable characterization of the climate and the sn cover and lead to an acceptable solution for the ener and mass balance.

In the physical sciences, it is difficult to provide an absolute verification of either calculated or measured conditions or characteristics. Instead, we evaluate the uncertainties in the measurement and in the assumptions inherent in the calculation to estimate the uncertainty of the result. The sensitivity of the result to error in any of the inputs is important in the determination of the appropriate computational approach and of priorities in the field measurement program. We have tried to measure most accurately those parameters that have the greatest influence on the accuracy of the result. Computational approaches requiring inputs or levels of accuracy that are difficult to achieve have been modified or eliminated.

In the following, each of the terms in the energy balance equation is presented in detail, showing the parameters which were measured or calculated. The uncertainty of those measurements and the assumptions made in calculating energy flux are evaluated, and the sensitivity of the result to errors in each phase of the calculation is determined. The magnitude of each term in the energy balance is estimated through the snow season, and the sensitivity of this balance to errors in the exchange calculations is evaluated.

9.1. Net Radiation at the Snow Surface

The radiant energy flux, or net all-wave radiation, at a point is the incident spectral irradiance less spectral exitance integrated over all wavelengths:

$$R_n = I - E_x \qquad (49)$$

where all quantities have units of W m^{-2}:

R_n = net all-wave radiation,
I = incident all-wave irradiance,
E_x = all-wave exitance.

The irradiance term includes direct and diffuse solar radiation and longwave radiation emitted from the atmosphere. Exitance includes both reflected and emitted radiation from the surface.

Radiation is the only form of energy transfer that can be measured directly in the natural environment. Incident radiation can be reliably and accurately measured in broad wavelength band widths, using well established techniques and instrumentation [Monteith, 1973] as demonstrated by Anderson [1976], Davis and Marks [1980], Olyphant [1984], Davis et al. [1984], Olyphant [1986a], and Marks et al. [1986]. The distribution of incident radiation can be modeled over complex alpine terrain, under clear sky conditions, for both solar [Dozier, 1980] and thermal [Marks and Dozier, 1979] wavelength ranges. Under cloudy conditions, measurements are necessary because the separate contributions of direct and diffuse solar and emitted thermal radiation from the atmosphere and clouds are not easily predicted or modeled. At some sites, measured irradiance may include reflection and emission from adjacent terrain. This effect can be accounted for if the surrounding terrain structure or "terrain configuration factor" is characterized. The solution to this problem is computationally difficult because each terrain facet visible from a point must be considered and because reflection from adjacent terrain is seldom isotropic [Siegel and Howell, 1981; Arnfield, 1982; Dozier and Marks, 1987]. At Emerald Lake incident radiation is measured at two sites to calibrate the estimate of irradiance for terrain effects, atmospheric effects, and cloud cover. Parameters that cannot be reliably measured are modeled. Net radiation is calculated from a combination of measured and modeled parameters.

Solar Radiation

Net radiation at the earth's surface is separated into two solar and one thermal spectral bands. Solar radiation (effectively 0.3 to 3.0 µm) is absorbed and scattered by terrestrial materials, but not emitted. For snow, absorption and scattering are functions of wavelength, incidence angle, and the optical properties of the surface [Bohren and Barkstrom, 1974; Warren, 1982].

These spectral features must be considered, but detailed spectral measurements of radiation at the snow surface are difficult under controlled conditions and not possible at a remote site. A spectral approach to modeling solar radiation, such as presented by Dozier [1980], will give an accurate result under clear skies, but it is complicated computationally and requires detailed information about the atmosphere and the snow surface which cannot be known when monitoring a remote site. Other investigators have taken a single-band, global approach to modeling solar radiation over remote alpine areas [Davies and Idso, 1979; Munroe and Young, 1982; Olyphant, 1984]. This simplifies the calculation of net radiation so that it can be done at a remote site, but may give an incorrect result by ignoring the distinct differences in the absorption and scattering properties of the snow surface in the visible and near-infrared wavelengths.

Marshall and Warren [1987] point out that most global climate models (GCM's) parameterize solar radiation into two bands, and suggest that snow albedo can also be parameterized to reduce computational difficulties while retaining the most important aspects of the spectral differences affecting net solar radiation at the snow surface. Utilizing this approach to better simulate solar radiation transfer at the snow surface, incident and reflected solar radiation are measured in two wavelength bands: visible (0.28–0.7 µm) and near-infrared (0.7–2.8 µm). The net solar radiation at a point is calculated by:

$$R_{n,sol} = I_v\,(1.0-\rho_v)+I_{nir}\,(1.0-\rho_{nir}) \qquad (50)$$

where:

$R_{n,sol}$ = net solar radiation ($W\,m^{-2}$),
I_v, I_{nir} = visible and near-infrared irradiance ($W\,m^{-2}$),
ρ_v, ρ_{nir} = visible and near-infrared reflectances.

The irradiances are measured, but the reflectances, or albedos, are estimated from a limited set of measured reflectances made at the Mammoth Mt. snow study plot. Measuring reflectance is difficult, even under controlled conditions, and it is not possible at a remote, unattended site. Detailed models of radiation transfer over a snow surface show that the spectral albedo of snow is determined by the snow grain size and by the concentration of absorbing impurities in the near-surface layer [Wiscombe and Warren, 1980; Warren and Wiscombe, 1980]. The effective grain size is generally defined as the radius of an ice sphere with optical properties equivalent to those exhibited by actual snow grains or crystals [Warren, 1982]. The effective grain radius of new snow is typically in the range of 20–200 µm, while old snow may have radii as large as 1500–2000 µm. The spectral albedo is parameterized into a two-band albedo that corresponds to the measured irradiance bands.

These bands correspond closely to those used by Marshall and Warren [1987] in their model which parameterizes the albedo of snow into visible and near-infrared bands. This model approximates snow albedo as a function of grain growth, contamination content, and sun angle for both bands. The decay of albedo with grain growth and the increase of albedo with solar zenith was calculated by Marshall and Warren [1987] by integrating theoretical values from the spectral albedo model of Wiscombe and Warren [1980] and Warren and Wiscombe [1980]. Measurements from the Mammoth Mt. snow study plot show albedo changes with sun angle and decay after a snow deposition event. The decay of albedo is inversely related to the square root of the grain radius. The albedo decay with increasing snow grain size is linear in the visible and non-linear in the near-infrared. The increase in albedo with solar zenith angle is a function of the square root of the grain size and the cosine of the zenith angle and is essentially linear in both the visible and near-infrared bands, but the effect is much larger in the near-infrared.

When the solar zenith angle is 0.0 with respect to the snow surface:

$$\rho_{v,0} = \rho_{v,max} - a_v\, r^{1/2} \qquad (51)$$

$$\rho_{nir,0} = \rho_{nir,max}\, \exp[a_{nir}\, r^{1/2}] \qquad (52)$$

where:

r = effective grain radius (µm),
$\rho_{v,max}$ = maximum visible albedo (1.0),
a_v = slope coef., visible albedo decay with grain growth (2.0×10^{-3}),
$\rho_{nir,max}$ = maximum near-infrared albedo (0.85447),
a_{nir} = slope coef., near-infrared albedo decay with grain growth (-2.123×10^{-2}).

This allows a linear decay of $\rho_{v,0}$ from about 0.98 to 0.90, and an exponential decay of $\rho_{nir,0}$ from 0.70 to 0.40, when reasonable grain radii are used. For sun angles other than 0.0:

$$\rho_{v,\theta} = \rho_{v,0}+[r^{1/2} a_{v,\theta}]\,[1.0-\cos\theta] \qquad (53)$$

$$\rho_{nir,\theta} = \rho_{nir,0}+[(r^{1/2} a_{nir,\theta})+b_{nir,\theta}]\,[1.0-\cos\theta] \qquad (54)$$

where:

θ = solar zenith angle, corrected for slope,
$a_{v,\theta} = \rho_{v,\theta}$ slope coef. (1.375×10^{-3}),
$a_{nir,\theta} = \rho_{nir,\theta}$ slope coef. (2.0×10^{-3}),
$b_{nir,\theta} = \rho_{nir,\theta}$ offset coef. (0.1).

The slope and offset coefficients in the above equations were derived from measured reflectances from the Mammoth Mt. snow study plot. They are similar, though not identical, to those reported by Marshall and Warren [1987]. Figure 9.1 shows albedo decay with grain growth and albedo increase with zenith angle for grain radii from 36 to 1600 µm.

The concentration of contaminants in the snow is difficult to determine, will increase with time in the absence of new snowfall, and is probably site specific. Grain size is difficult to measure as well, but both of these parameters must be determined before an estimate of the albedo can be made using the model presented above. No measurements of either were available for this analysis, so the combined effect of both had to be lumped together in the determination of the coefficients in the above equations. Two years of intermittent measurements of snow albedo from the Mammoth Mt. snow study plot (located at 2925 m in the eastern Sierra Nevada) were combined with the above equations to evaluate the range of values and growth rates that can be expected in an environment similar to Emerald Lake. The above equations were inverted to solve for grain size from measured albedo, which for the visible band is actually a combination of grain size and contamination. In the implementation of the Marshall and Warren [1987] albedo model, contamination was treated as affecting only the visible albedo. It has the effect of increasing the effective grain radius for the calculation of ρ_v over the measured value. This approach showed that for the measured albedos, the effective visible grain radius, after accounting for contamination, was typically 1.5–3.0 times the solution for near-infrared grain radius, which should be close to measured grain size. Lower values occurred in early winter, during cold conditions, with higher values occurring in spring. The range of grain growth also appeared to be seasonally constrained. Early season data showed initial grain sizes of around 20–75 µm, while spring storms were in the 50–150 µm range. Winter maximum grain growth was in the 500–700 µm range, while spring values were 1000 µm or more.

Once a solution was reached on the apparent effect of contamination and for initial and maximum grain sizes, grain growth rates could be approximated. The solution allowed a single grain size for both visible and near-infrared, with only the contamination factor differentiating the two. If the time (in days) of the last snowfall t, the effective grain size of that event r, the expected grain growth maximum r_{max}, and visible contamination factor c_{tm}, are known, albedo can be estimated from time (in days) since that snowfall, and solar zenith. The initial effective grain size, after a snow event, and expected growth range for the visible and near-infrared are calculated by:

$$r_{v(0)} = c_{tm}\, r^{1/2} \tag{55}$$

$$r_{nir(0)} = r^{1/2} \tag{56}$$

$$r_{ng,v} = c_{tm}\,[\,r_{\max} - r\,]^{1/2} \tag{57}$$

$$r_{ng,nir} = [\,r_{\max} - r\,]^{1/2} \tag{58}$$

Grain growth rates are approximated by a second order Chebyshev polynomial [Acton, 1970], where t = time since last snowfall + 1.0 (days):

$$g_{th} = 1.0 - \left\{ \frac{4+3t+t^2}{2+t+t^2} - 1.0 \right\} \tag{59}$$

The effective grain size at time t after a snow event is:

$$r_{v(t)} = r_{v(0)} + [r_{ng,v}\ \ g_{th}] \tag{60}$$

$$r_{nir(t)} = r_{nir(0)} + [r_{ng,nir}\ \ g_{th}] \tag{61}$$

This function ranges from 0.0 to 1.0, while t ranges from 0 to ∞, but it achieves 80% of its range by $t = 9$. It appears to have no seasonal variation, but this is difficult to determine as periods of continuous albedo measurement are seldom longer than a few weeks. It is not based on the physics of grain growth, but fits the measured reflectance decay for both visible and near-infrared.

Albedos at time t after a snow event are calculated as above, first for $\theta = 0$:

$$\rho_{v,0}(t) = \rho_{v,\max(t)} - r_{v(t)}\, a_v \tag{62}$$

$$\rho_{nir,0}(t) = \rho_{nir,\max(t)} \exp[\, r_{nir(t)}\, a_{nir}\,] \tag{63}$$

and then corrected for zenith angle:

$$\rho_{v,\theta(t)} = \rho_{v,0}(t) + [r_{v(t)}\, a_{v,\theta}]\,[1.0 - \cos\theta]$$

$$\rho_{nir,\theta(t)} = \rho_{nir,0}(t) + \\ [(r_{nir(t)}\, a_{nir,\theta}) + b_{nir,\theta}]\,[1.0 - \cos\theta]$$

Figure 9.2 shows computed vs. measured albedo for the data from the Mammoth Mt. site, for early and mid-winter and early and late spring periods during the 1986 snow season. Because solar reflectance is difficult to measure continuously, only a small data set from a few clear days during the 1986 snow season is currently available and the effect of shadowing and cloud cover is unknown. It is therefore not justified to statistically evaluate the fit of the modeled vs. measured albedos. Flat regions in the measured curves are probably the result of shadowing by the instrument at high solar zeniths, but they could also be caused by cloud cover. The effect of cloud cover is difficult to calibrate from these data, as independent measurement of beam and diffuse irradiance was not made. It is not possible to correct the measured reflectances for these effects because information on conditions and instrument position during the experiment are not available. However, these data represent the best continuously measured broad wavelength band albedos made in the past 10 or 15 years in the Sierra Nevada. The fit of the modeled to the measured albedos appears to be good. To make a better evaluation of an albedo model would require a more detailed measurement program and a careful evaluation of snow grain size and contamination content.

Data for snowfall dates and volumes were used with the model presented above to calculate albedos for the Emerald Lake watershed for the period from October 20, 1985 to August 1, 1986. This period represents the duration of significant snowcover in the watershed. Figure 9.3 presents the results of this calculation. The upper curve is the visible albedo, and the lower is the near-infrared albedo. The width of each function illustrates the magnitude of the increase in albedo with cosine of the solar zenith, while the bottom of each function illustrates the effective albedo for each band during the period of maximum solar irradiance. The visible albedo shows a rapid, but limited decay following a snowfall, while the near-infrared albedo shows a rapid, significant decay following a snowfall.

Net solar radiation was computed from the modeled albedos and measured irradiances for two sites in the Emerald Lake watershed. Figures 9.4 and 9.5 present these results for daily averages at both the ridge and lake sites. As shown in Table 9.2, near-infrared irradiance represents 53% of the total solar irradiance at the ridge site, and 60% of the total at the lake site. However, it represents 85% of the net solar input at the ridge and 89% at the lake site. In early winter, the ridge site receives more solar irradiance than the lake site, but by early spring they are about the same, and by late spring the lake site is receiving significantly more solar radiation than the ridge. Large solar zenith angles during winter cause the lake site to be shadowed for a significant part of the day, but in spring the sun is higher in the sky, and this shadowing is reduced.

Figure 9.6 shows hourly average solar irradiance for a diurnal cycle in mid-December and mid-June. In December the sun at the lake site "rises" about 1 hour later than at the ridge site and "sets" about 2 hours earlier. By June these differences are halved. Because the watershed is a bowl-shaped cirque, it acts as a reflector to scatter solar radiation down toward the lake site. The mid-day maximum solar irradiance is greater at the lake site in both December and June. Scattering by snowcovered adjacent terrain contributes to the slightly larger total and near-infrared contribution at the Lake site during the spring melt season. Shadowing in the early morning and late afternoon at the lake site reduces the daily input of visible light more than the near-infrared.

The surrounding slopes have low solar incidence angles during the most of the day. Both visible and near-infrared irradiance are increased, but the near-infrared increase is larger because increase in near-infrared albedo is greater at low incidence angles than is the visible albedo. For an unobstructed site, the increase in albedo at low sun angles (early morning, and late afternoon) has little effect on the radiation budget, because the irradiant energy at those times is small. This is not true when the albedo increase occurs during mid-day when solar irradiance is large. The contribution of radiation scattered from adjacent terrain at the lake site is large enough to overcome shadowing during spring when sun angles are high, and most of the surrounding slopes are snowcovered. Figure 9.7 shows hourly average net solar radiation, and net visible and near-infrared radiation at both sites for the same diurnal periods in December and June. There is no real difference in the maximum visible net radiation between the two sites at either time. It is the shorter sunlit period at the lake site that causes the difference. The maximum net near-infrared radiation is greater at the lake site at both times, but the much shorter sunlit period at the lake site in winter causes the integral to be smaller. In spring, the difference in the illuminated periods is reduced and the mid-day increase in the near-infrared at the lake site increases, so that the integral at the lake site is slightly larger.

Thermal Radiation

Thermal radiation (effectively 3.5 to 50 μm) is absorbed and emitted without appreciable scattering [Paltridge and Platt, 1976]. Because net thermal radiation is a function of the absolute temperature of its constituents, the assumption is made that spectral variations are minimal. This simplifies the measurement of thermal irradiance and the calculation of the net thermal radiation by eliminating spectral considerations and allowing the use of broad band emissivities for the snow surface and surrounding terrain. As explained by Marks and Dozier [1979], in an alpine region the net thermal radiation at the surface is a function of the surface temperature and thermal properties, atmospheric conditions, and terrain effects. If thermal irradiance is measured, net thermal radiation is:

$$R_{n,lw} = I_{lw} - (\varepsilon_s \sigma T_s^4) \tag{66}$$

where:

$R_{n,lw}$ = net thermal radiation (W m^{-2}),
I_{lw} = thermal irradiance (W m^{-2}),
ε_s = surface emissivity (≈0.99),
σ = Stefan-Boltzmann Constant (5.6697×10^{-8} Wm^{-2}K^{-1}),
T_s = surface temperature (K).

Considerable effort has gone into modeling thermal irradiance from the atmosphere, with most of this work concentrating on estimating atmospheric emissivity under clear sky conditions [e.g., Idso and Jackson, 1969; Marks and Dozier, 1979; Satterlund, 1979; Idso, 1981; Kimball et al., 1982]. In addition to estimating atmospheric emissivity, Marks and Dozier [1979] allow for calculation of longwave radiation over an area, by accounting for terrain effects and for variations in atmospheric emissivity with air pressure as a function of elevation. Cloud cover will cause marked increased in thermal irradiance at the snow surface and, as for solar radiation, this effect in not easily modeled. Thermal radiation is generally a stable function and does not vary much over an area the size of the Emerald Lake watershed. Measured values at a few points effectively characterize thermal irradiance, incorporating the effect of cloud cover.

Thermal exitance is a function of the snow surface temperature and emissivity. The emissivity of snow is 0.988–0.990 for all grain sizes above r = 75μm; for fine-grained snow, r = 50μm, the emissivity drops slightly to 0.985 [Dozier and Warren, 1982].

If the full energy budget is calculated, the surface temperature can be derived, but these calculations are not possible at this time for an entire snow season at a one hour time step. Snow surface temperature was estimated using the method discussed in a previous section. It is recognized that these estimates may be incorrect during some conditions, especially periods when winds are light or calm, and radiative heating or cooling that would be expected to occur cannot be accounted for by this simple model. It is important to note, however, that the calculation of thermal exitance requires the Kelvin temperature, so that even a modest error in surface temperature will not have a significant effect on the result. Measured surface temperatures suggest that errors in the estimate of snow surface temperature are seldom larger than 1°C. If the true snow surface temperature is –5.0°C and the modeled surface temperature is in the range of –10.0 to 0.0°C, the error in the calculated thermal exitance will be no larger than about 20 Wm^{-2}, or 6.5%.

Thermal exitance, and net thermal radiation were calculated for hourly averages of measured thermal irradiance and modeled surface temperature. Figure 9.8 presents these results for daily net thermal radiation. Net thermal radiation tends to have a cooling effect on the snowcover throughout the season. It can be very negative during the early and mid-winter, and then tends to small negative values or zero during spring and melt.

Net All-wave Radiation

Net all-wave radiation is the sum of net solar and net thermal. Figures 9.9 and 9.10 present daily means for the ridge and lake sites during the 1986 snow season. Table 9.3 shows the monthly total input for each component of the radiation balance at the two sites. Thermal and solar radiation make up approximately equal parts of the radiation balance. If the October and August totals were included the difference between net solar and net thermal would be closer to zero. Radiation is slightly more important at the lake site than at the ridge, but the two sites are about the same throughout the snow season. Early in the snow season the radiation budget is dominated by thermal radiation, but during melt solar radiation predominates. The ratios of one to the other are almost exactly reversed between November and July. April is the cross-over month with solar and thermal radiation almost exactly balancing each other.

9.2. Turbulent Transfer at the Snow Surface

Turbulent energy exchange at the snow surface is second only to radiation in importance during the snow season. The turbulent transfer of momentum, heat, and water vapor at the snow surface are the most complicated forms of energy exchange, and are not easily measured in a natural environment. The data required to calculate them are difficult to measure at a point, and they have a highly stochastic distribution over a topographic surface. Yet not only does significant energy transfer occur by turbulent exchange, but in the Sierra Nevada significant mass loss can occur by these processes [Beaty, 1975; Stewart, 1982; Davis et al., 1984]. Therefore the calculation of turbulent exchange at the snow surface should be as accurate as possible.

Several tractable approaches to calculating sensible and latent fluxes have been presented [Sellers, 1965; Businger, 1973; Fleagle and Businger, 1980; Brutsaert, 1982]. Andreas et al. [1979, 1984] developed a technique for calculation of turbulent transfer over snow and ice in the Arctic and Antarctic, and Stewart [1982] presented a method for use over an alpine snowcover. For the general case of bulk transfer near the snow surface:

$$H = \rho\, C_p\, K_H\, (T_a - T_s) \tag{67}$$

and

$$L_v E = \rho\, K_W\, L_v\, (q - q_s) \tag{68}$$

where:

H = sensible heat exchange (Wm^{-2}),
$L_v E$ = latent heat exchange (Wm^{-2}),
ρ = air density ($kg\,m^{-3}$),
C_p = specific heat of dry air, constant pressure ($1005\,J\,kg^{-1}\,K^{-1}$),
K_H, K_W = heat and water vapor bulk transfer coefficients,
T_s, T_a = surface and air potential temperatures (K),
L_v = latent heat of vaporization ($\geq 2.5\times10^6 J\,kg^{-1}$),
q_s, q = specific humidities at surface and in the air.

The problem is that K_H and K_W are difficult to estimate and may vary significantly in both time and space. They are functions of surface temperature and air temperature, the humidity of the air, the wind field, and the surface roughness over the watershed.

The magnitude of H and $L_v E$ can be large over a snow surface and can have a significant effect on the energy budget of the snowcover. Stewart [1982] developed a point model based on the Businger-Dyer simplification of the eddy transfer equations [Fleagle and Businger, 1980]. Using this model and measurements of vapor stress and snow ablation from the Mammoth Mt. snow study plot, he showed that as much as 25% (0.65 m $H_2O\,m^{-2}$) of the mass of the snowcover was lost to sublimation during May, 1981. While this volume of water loss in one month may be extreme, measurements from the same site over several years indicate that it is common to lose that much or more SWE to sublimation during the snow season.

An improvement over the method tested by Stewart for calculating sensible and latent heat, and mass fluxes is adapted from Brutsaert [1982]. The usual condition for data collection at a remote site is that only one measurement is available for air temperature, humidity, and wind speed, and that these may not all be at the same height above the surface. (In fact, the height above the snow surface will be continually changing as the snowcover accumulates and ablates.) Air temperature T_a is measured at height z_T, specific humidity q which can be calculated from vapor pressure at z_q, and wind speed u at z_u. The equations to be solved are:

Obukhov stability length:

$$L = \frac{u_*^3\,\rho}{k\,g\left[\dfrac{H}{T_a\,C_p} + 0.61E\right]} \tag{69}$$

Friction velocity:

$$u_* = \frac{u\,k}{\ln\left[\dfrac{z_u - d_0}{z_0}\right] - \psi_{sm}\left[\dfrac{z_u}{L}\right]} \tag{70}$$

Sensible heat flux (positive toward the surface):

$$H = \frac{(T_a - T_s)\,a_H\,k\,u_*\,\rho\,C_p}{\ln\left[\dfrac{z_T - d_0}{z_0}\right] - \psi_{sh}\left[\dfrac{z_T}{L}\right]} \tag{71}$$

Mass flux (positive toward the surface):

$$E = \frac{(q - q_s)\,a_E\,k\,u_*\,\rho}{\ln\left[\dfrac{z_q - d_0}{z_0}\right] - \psi_{sv}\left[\dfrac{z_q}{L}\right]} \tag{72}$$

The other variables are:

a_H, a_E = ratio of eddy diffusivity and viscosity for heat and water vapor; while there is some uncertainty associated with the value of these dimensionless ratios, Brutsaert suggests $a_H = a_E = 1.0$;

k = von Karman's constant (dimensionless); $k \approx 0.40$;

g = acceleration of gravity (9.80616 m s^{-2});

d_0 = zero-plane displacement height (m); Brutsaert suggests $d_0 = (2/3)\ 7.35\ z_0$;

z_0 = surface roughness length (m); For snow, which is fairly smooth, z_0 ranges from 0.0001 to 0.005 m, though if local vegetation cover and terrain features are considered, the value could be much higher.

The ψ-functions, ψ_{sm} for mass, ψ_{sh} for heat, and ψ_{sv} for water vapor, are:

Stable ($\zeta = \frac{z}{L} > 0$):

$$\psi_{sm}(\zeta) = \psi_{sv}(\zeta) = \psi_{sh}(\zeta) = \begin{cases} -\beta_s & 0<\zeta\le 1 \\ -\beta_s & \zeta>1 \end{cases}, \quad \beta_s = 5 \qquad (73)$$

Unstable ($\zeta = \frac{z}{L} < 0$):

$$x = (1 - \beta_u\, \zeta)^{1/4}, \quad \beta_u = 16 \qquad (74)$$

$$\psi_{sm} = 2 \ln\left[\frac{1+x}{2}\right] + \ln\left[\frac{1+x^2}{2}\right] - 2 \arctan x + \frac{\pi}{2} \qquad (75)$$

$$\psi_{sh}(\zeta) = \psi_{sv}(\zeta) = 2 \ln\left[\frac{1+x^2}{2}\right] \qquad (76)$$

The three most critical terms in the above equations are the wind speed u, the temperature difference between the air and the surface $T_a - T_s$, and the humidity difference between the air and the surface $q - q_s$. If the wind speed goes to zero, u^*, H, and E also go to zero. If the air and the surface are the same temperature, H is zero, and if the humidity of the air and the surface are the same, E is zero. Turbulent transfer of heat and mass is controlled first by the magnitude of the wind speed, and then by the temperature and humidity gradients between the snow surface and the air.

From the discussion of weather conditions in the Emerald Lake basin during the 1986 snow season we know that while the lake site is significantly less windy than the ridge site, there is seldom a long duration period of calm conditions at either site (Figure 6.6). Except under very cold, calm conditions or during storms, the vapor pressure of the air is always less than that of the snow surface (Figure 6.5). As long as the air temperature is less than 0.0°C, snow surface temperature will track air temperature, so it is unlikely that the temperature difference between the two can be very large. However, once the air temperature is above 0.0°C, the snow surface is constrained to be 0.0°C or less, and the temperature difference can increase in magnitude. This is particularly important during spring of the 1986 snow season when air temperatures remained above freezing throughout the diurnal period from early May on (Figure 6.1).

The magnitudes of latent heat and mass flux and sensible heat flux are controlled by the wind speed, and therefore will be smaller at the lake site than at the ridge. The direction (positive toward, negative away from the surface) of these fluxes is controlled by the sign of the temperature and humidity difference between the air and the snow surface. Latent heat and mass flux are therefore constrained by the data to be negative at both the ridge and lake sites throughout the year. Sensible heat flux will be mostly positive at both sites throughout the year and always positive during spring once the air temperature does not go below freezing at night.

Figure 9.11 presents daily averages of calculated sensible and latent heat transfer for the ridge and lake sites during the 1986 snow season. As expected, the magnitude of turbulent exchange was larger at the ridge than at the lake, and in general, latent transfer is away from, and sensible transfer is toward the snow surface. What is striking about these calculations, is that the latent and sensible transfers tend to mirror each other most of the time.

For both to be negative the air must be both colder and less humid than the snow surface. This condition occurs occasionally during winter, but does not persist as the snow surface either cools to the air temperature or the air temperature increases during a diurnal cycle. It almost never occurs during spring in Emerald Lake watershed. In a warm alpine environment, like the Emerald Lake watershed, above-freezing air temperatures are likely during part of the day throughout the snow season (Figure 6.1), and as shown in Figure 6.3, very cold temperatures tend to occur during periods of low wind speeds. The air temperature did not go below freezing at either site after early spring during 1986.

For both to be positive, the air must be warmer and more humid than the snow surface. These conditions occurred very infrequently during the 1986 snow season, as shown by the indicated surface condensation events in Figure 6.5. When they did it was either during a storm or during very cold, calm conditions. A warm rain event during spring would be an extreme case of combined positive turbulent transfer at the snow surface. This did not occur during the 1986 snow season, and even when it does, it is usually a short-duration event.

Over time, the magnitudes of sensible and latent heat transfer over a snow surface are of opposite sign, and their sum tends to minimize their effect on the overall snow surface energy budget. This sum, designated "net" turbulent transfer, shown as daily means in Figure 9.12 illustrates the overall effect of turbulent transfer at the snow surface during the 1986 snow season.

The values of the coefficients a_H, a_E, k, d_0, and z_0 used in the turbulent transfer calculations cannot be known precisely, though Brutsaert [1982] states that they can be estimated to within 10% of their true values from an evaluation of conditions at the data collection site. This uncertainty, however, will affect the magnitude but not the sign of the result. Thus, the sum of sensible and latent heat transfer should not be affected over a period of a day or more. Mass flux will be affected, however, because it is the result of latent exchange only. Calculations of mass flux are approximations with an uncertainty of at least 10% over a time period of a day or less. Over a longer time period, this uncertainty should diminish.

Table 9.4 summarizes turbulent heat and mass transfer during the 1986 snow season. Over the snow season, sensible (H) and latent ($L_v E$) heat transfer make up about equal parts of the net turbulent transfer ($H + L_v E$) at both sites, though $L_v E$ is slightly favored. About 626m^{-2} of SWE sublimated at the ridge site, and about 487m^{-2} of SWE sublimated at the lake site during the 1986 snow season. Turbulent transfer is slightly more important at the ridge site than at the lake, but though the magnitudes of both H and $L_v E$ are larger at the ridge throughout the snow season, differences in the net turbulent transfer are not large. Latent heat exchange dominates at both sites during winter, but is replaced by sensible heat transfer during spring melt. Though the magnitude of H during spring is larger than $L_v E$ during winter, $L_v E$ is also large during spring, unlike H during winter. The effect of H on the net turbulent exchange is therefore reduced. The cross-over between negative and positive net turbulent exchange is made during May and June when H and $L_v E$ are about equal in magnitude. This is important because these were the months of maximum snow melt runoff generation during the 1986 snow season. Errors in the estimation of the magnitudes of H and $L_v E$ during this period would have minimal effect on calculation of snowmelt.

9.3. Conduction and Advected Heat Transfer to the Snowcover

Both conductive and advective heat transfer tend to be small when compared to the seasonal energy balance of the snowcover. They can therefore be ignored or greatly simplified. One dimensional, steady-state heat flow in a homogeneous layer is:

$$G = K \frac{\partial T}{\partial z} \tag{77}$$

where:

K = thermal conductivity (J m^{-1} K^{-1} s^{-1}),
T = temperature (K),
z = layer thickness (m).

Because soil and snow temperature near their interface are usually very similar, the calculation of heat transfer between them is based on the assumption that the two represent homogeneous layers in contact with each other. If we know the temperature, T_{sno} and T_g, of these layers, and estimate their thickness (usually the distance of the temperature measurement above and below the interface) heat transfer can be approximated by:

$$G = \frac{2 K_{es,l} K_{eg} (T_g - T_{s,l})}{K_{eg} z_{s,l} + K_{es,l} z_g} \tag{78}$$

where:

$K_{es,l}, K_{eg}$ = snow and soil layer effective thermal conductivity (J m^{-1} K^{-1} s^{-1}),
$T_{s,l}, T_g$ = snow and soil layer temperatures (K),
$z_{s,l}, z_g$ = snow and soil layer thicknesses (m).

The thermal conductivity of soil, K_g, is assumed essentially constant [Davis, 1980]; we use the value for a moist coarse sand (2.2 J m^{-1} K^{-1} s^{-1}) [Oke, 1978]. There are a variety of empirical methods for estimating the thermal conductivity of the snow as a function of density, summarized by Yen [1969] and more recently by Langham [1981]. The method described by Yen [1965], selected as most appropriate for use in the Emerald Lake basin, is used to compute thermal conductivity of a snowcover layer as a function of snow density ρ_s (kg m^{-3}):

$$K_{s,l} = 3.2238\times10^{-8}\ \rho_s{}^2 \tag{79}$$

Because the air fraction of the snowcover is always at saturation, and the air fraction of soil is usually at saturation, vapor diffusion is estimated as a function of snow and soil temperature and air pressure. Both the snow and soil thermal conductivities $K_{s,l}$ and K_g are corrected for vapor diffusion by adding a value that is based on their specific humidities $q_{s,l}$ and q_g, and the calculated vapor diffusion coefficient for each. The effective diffusion coefficient for water vapor in snow or a saturated, inorganic soil at 0.0°C and sea level air pressure $D_{e,0}$ was determined experimentally by Yen [1965] to be around 10^{-5} m^{-2} s^{-1}. Anderson [1976] developed the following relationship for determining the diffusion coefficient at other temperatures:

$$D_e = D_{e,0} \frac{P_0}{P_a} \left[\frac{T_{s,l}}{T_{melt}} \right]^{n_T} \tag{80}$$

where:

P_a = air pressure (Pa),
P_0 = sea level air pressure (101,342 Pa),
$T_{s,l}$ = snowcover layer temperature (K),
T_{melt} = melting temperature of ice (273.16K),
n_T = layer temperature exponent ($\approx$14).

The temperature exponent was empirically determined by Anderson to be about 14. Because the temperature for a snow or soil layer is nearly always close or equal to 273.16K during the snow season, and P_a is always equal to or less than the sea level value, precision of n_T is not critical. The effective diffusion coefficient D_e is always small and relatively stable, varying from 10^{-5} down to around 0.5×10^{-5} m^{-2} s^{-1} for air pressure of 65 kPa and snow temperatures between 273.16 and 250K.

Thermal conductivities are adjusted for vapor transport by an empirical correction based on the effective diffusion coefficient; this is an empirical correction developed by Anderson [1976] and is not dimensionally correct:

$$K_{es,l} = K_{s,l} + [L_v D_e q_{s,l}] \tag{81}$$

$$K_{eg} = K_g + [L_v D_e q_g] \tag{82}$$

where:

$K_{es,l}, K_{eg}$ = effective thermal conductivities of snow and soil layers (J m^{-1} K^{-1} s^{-1}),
$q_{s,l}, q_g$ = specific humidity of snow and soil layers.

While the latent heat of vaporization or sublimation is a function of temperature, it is always large (>2.5x10^6 J kg^{-1}), so this correction can have the effect of increasing the thermal conductivity of snow by a factor of 10 or more. Under conditions found at Emerald Lake during spring of 1986:

$\rho_S = 600\,\mathrm{kg\,m^{-3}}$,
$P_a = 75\,\mathrm{kPa}$,
$T_{s,l} = 273.16\mathrm{K}$,
$D_e = 1.351\times10^{-5}\,\mathrm{m^2\,s^{-1}}$,
$q_{s,l} = 4.847\times10^{-3}$,
$L_v = 2.834\times10^{6}\,\mathrm{J\,kg^{-1}}$,
$K_{s,l} = 0.0116\,\mathrm{J\,m^{-1}\,K^{-1}\,s^{-1}}$,
$K_{es,l} = 0.1971\,\mathrm{J\,m^{-1}\,K^{-1}\,s^{-1}}$.

Though there is nearly a twenty-fold increase in the thermal conductivity of the snow when it is corrected for vapor diffusion this is still a very low conductivity; it is more than an order of magnitude lower that the uncorrected thermal conductivity of the soil ($2.2\,\mathrm{J\,m^{-1}\,K^{-1}\,s^{-1}}$). The effective thermal conductivity of the soil K_{eg} will also increase when corrected for diffusion, but much less significantly.

Heat transfer between the soil and the snowcover was computed for the ridge and lake sites for the 1986 snow season. Table 9.5 presents a summary of these calculations for the 1986 snow season. The flux is small and slightly positive during the snow season at both sites. The season totals represent an average flux less than $3.0\,\mathrm{Wm^{-2}}$ at the ridge site, and less than $4.0\,\mathrm{Wm^{-2}}$ and the lake site. This flux is slightly larger at the lake site during winter than at the ridge, but by spring both sites are the same. From mid-March until the end of the snowcover the values are essentially zero at both sites. This is because liquid water percolation into the soil removes most of the temperature gradient. Davis [1980], utilizing a similar, but more detailed model at several sites in the alpine Sierra Nevada, got the same result because temperature gradients were always small.

Table 9.5. Soil Heat Transfer Summary
Monthly Totals ($\mathrm{MJ\,m^{-2}}$)
Emerald Lake Watershed, 1986 Snow Season

Month	Ridge	Lake
November	17.15	21.93
December	13.53	20.45
January	10.28	15.14
February	8.67	11.86
March	6.00	8.46
April	3.97	4.46
May	2.61	2.77
June	1.46	1.47
July	4.93	3.69
Total	68.6	90.23

Advected heat transfer at the snow surface occurs when mass, in the form of precipitation (rain or snow), is added to the snowcover. If there is a difference between the added precipitation and the snowcover, the energy transfer ($\mathrm{J\,m^{-2}}$) is a function of the mass added, and the magnitude of the temperature difference:

$$M = C_{p\_p}\,\rho_{pp}\,z_{pp}\,[T_{pp} - T_S] \tag{83}$$

where:

C_{p_p} = specific heat of precipitation ($\mathrm{J\,kg^{-1}\,K^{-1}}$),
ρ_{pp} = precipitation density ($\mathrm{kg\,m^{-3}}$),
z_{pp} = precipitation depth (m),
T_{pp} = average precipitation temperature (K),
T_S = average snowcover temperature (K).

Because the temperature difference is not likely to be large, the magnitude of advection is largely controlled by the mass of precipitation ($\rho_{pp} \times z_{pp}$) deposited on the snow surface. Advection is treated as an event occurrence because no reliable data exist on deposition rates or conditions. The mean air temperature during the precipitation event is assumed to be the precipitation temperature. If precipitation is warmer than the snowcover, M will be positive.

Specific heat of a substance is the amount of energy required to change its temperature. Specific heat of both water and ice is a function of temperature. The specific heat of water at 273.16K is $4217.7\,\mathrm{J\,kg^{-1}\,K^{-1}}$, and the specific heat of ice is about half that of water. Specific heat of both ice and water can be approximated as a linear function of absolute temperature in the region from −25 to 25°C:

$$C_{p\_ice} = 104.369 + 7.369\,T_{ice} \tag{84}$$

$$C_{p\_w} = C_{p\_w,melt} - 2.55\,[T_w - T_{melt}] \tag{85}$$

where:

C_{p_ice} = specific heat of ice ($\mathrm{J\,kg^{-1}\,K^{-1}}$),
C_{p_w} = specific heat of water ($\mathrm{J\,kg^{-1}\,K^{-1}}$),
$C_{p\_w,melt}$ = specific heat of water at 273.16K ($4217.7\,\mathrm{J\,kg^{-1}\,K^{-1}}$),
T_{ice} = ice temperature (K),
T_w = water temperature (K).

Advection will be relatively small unless the temperature difference is large, which is not usually the case. Even rain-on-snow events tend to be at or very close to freezing temperatures. Heat transfer during rain-on-snow is usually dominated by condensation rather than advection.

Seventeen precipitation events were recorded during the 1986 snow season. Table 9.6 shows the advected heat and mass transfer for each of these. Mass flux is presented as a specific mass, or mass/area, which can be converted directly to $\mathrm{m^{-2}}$ liquid water. The total advected heat from all events is relatively small during the 1986 snow season. The direction of the transfer has no seasonal pattern, though most of the advected heat transfer occurred during the large volume events during February and March.

TABLE 9.6. Advected Heat and Mass Transfer
Emerald Lake Watershed, 1986 Snow Season

Event Date	Advection ($J\,m^{-2}$)	Mass Flux ($kg\,m^{-2}$)
85/10/06	-16,929	16
85/10/08	58,021	11
85/10/21	239,216	38
85/11/11	-194,142	118
85/11/20	-48,188	115
85/12/03	79,706	378
85/12/11	21,812	35
86/01/08	-418,172	152
86/02/03	1,162,046	178
86/02/06	-16,682	5
86/02/18	5,756,722	826
86/02/19	-553,888	240
86/03/19	-1,782,649	427
86/04/10	130,863	35
86/04/16	-110,653	14
86/05/04	-104,383	24
86/05/07	-10,187	10
Total	4,192,513	2622

Table 9.7 summarizes advected heat and mass transfer for the 1986 snow season, presenting monthly totals. (The November totals include heat transfer and mass flux from October.) Advection is always small, but it was largest during February when most of the season's precipitation occurred. The mass of precipitation falling during a snow season will dominate the magnitude of advected heat transfer. That the 1986 snow season was one of the largest on record makes it clear that the magnitude of this form of energy transfer will always be very small.

Table 9.7. Advected Heat and Mass Transfer Summary
Monthly Totals, Emerald Lake Watershed, 1986 Snow Season

Month	Advection ($MJ\,m^{-2}$)	Mass Flux ($kg\,m^{-2}$)
November	-0.24	298
December	0.10	413
January	-0.42	152
February	6.35	1249
March	-1.78	427
April	0.02	49
May	-0.12	34
June	0.00	0
July	0.00	0
Total	3.91	2622

9.4. Snowcover Energy and Mass Balance

The energy transfer terms discussed in previous sections determine the thermal condition and the ablation rates for the seasonal snowcover. The sum of the energy transfer terms is referred to as the energy balance, because in thermal equilibrium, all of these terms must sum to zero. When the snowcover is not in equilibrium, this sum determines the sign and magnitude of ΔQ, the energy available to alter the thermal structure and mass of the snowcover. Negative ΔQ indicates a cooling snowcover, while positive ΔQ indicates warming. Once the snowcover has been warmed to the melting temperature of ice (0.0°C or 273.16K) any additional input of energy must result in melt which will become runoff.

Table 9.8 presents a summary of the energy and mass balance of the snowcover for the ridge and lake sites for the 1986 snow season. Table 9.9 presents a summary of the relative magnitudes of energy transfer and Table 9.10 a summary of the relative magnitudes of mass flux at both sites. In general, ΔQ is greater in magnitude at the ridge site throughout the snow season though this difference is not large. At both sites, the transition from a negative to a positive ΔQ occurs in late April or early May. The critical terms in determining the energy budget are the net radiation, R, and net turbulent transfer, $H + L_v E$. The importance of energy transfer by conduction from the soil, G, is slightly greater at the lake site, but it is always small and is especially unimportant during spring melt. Advected energy transfer, M, has no significant effect on the magnitude of ΔQ at either site.

The absolute uncertainty of the energy transfer terms presented cannot be determined in the field. However, an estimate of the uncertainty is presented in Table 9.11 for the critical parameters affecting the magnitude of each energy transfer term. Radiation and turbulent transfer each contribute about half of the uncertainty in the total energy balance. These estimates are for conditions during snowmelt and are based on the the recorded data precision estimates presented in Table 3.2. They represent the maximum range of variance that could occur for all terms considered. Uncertainty should diminish if averaged over a longer period, and it is likely that the combination of positive and negative errors in individual parameters would tend to cancel.

Figure 9.13 presents daily average values for net all-wave radiation and net turbulent energy exchange, which make up most of the energy budget at the ridge and lake sites. Figure 9.14 presents daily averages of the sum of all energy transfer terms at both the ridge and lake sites. It is noteworthy that the magnitude of the hourly averages of ΔQ can be large (greater than $\pm 500\,Wm^{-2}$), though the daily averages are seldom greater than $\pm 200\,Wm^{-2}$. The effect of these short term periods of large magnitude energy flux on the snowcover are masked when only longer term averages are considered. This is especially true during spring melt when significant melt may occur only during half of the diurnal cycle.

Net radiation is greater in magnitude than net turbulent transfer in all months, except March and April at the ridge site and April at the lake site. During winter (November through March), both net radiation and turbulent transfer are negative, with the magnitude of net radiation being around 1.5−2.0 times that of net turbulent transfer at both sites. The transition from negative to positive occurs in April for net radiation, but not until May for net turbulent transfer. This causes the relative magnitude of turbulent transfer to be much larger, having a greater effect on the value of ΔQ during this period as the magnitude of net radiation is close to 0.0. During the 1986 water year, most snowmelt and 87% of the snowmelt runoff occurred during May, June, and July. During these months net radiation accounted for over 71% of the energy input at the ridge site and over 82% of the energy input at the lake site. While turbulent transfer is important during snowmelt, radiation dominates the energy budget, even at an exposed, windy site like the ridge.

The mass balance presented is only an approximation to the true mass balance. Detailed information on the thermal condition and mass of the snowcover were not available for the entire season for these calculations. These calculations are presented as a verification of the energy transfer calculations. By the end of July, the snowcover had essentially ablated at both the ridge and lake sites. This is also predicted by the energy balance sum for the nine months for which data were available. While the calculations show that the snowcover should have ablated sooner at the ridge than at the lake, the difference is only 5%, which is well within the uncertainty of these calculations. Pit data from the ridge site indicate that at maximum accumulation there were over 3.0 m of SWE there. Observations during the snow season indicate that this site received considerable re-deposition of snow between storm events. Early season data, when snowboards were in place at both the ridge and lake sites, indicate that event deposition volumes were similar at both sites. After the large February storm, snowboard data were not available at the ridge site. The snow deposition volumes shown in the tables represent the best estimate of what the average deposition was at the two sites.

Estimates of snowmelt runoff volumes are based on measured flow volumes from the outflow of Emerald Lake. This volume was subtracted from the monthly flow volumes at the outflow, and the residual was assumed to be snowmelt. Though the data indicate that the ridge and lake do not differ greatly in terms of energy transfer, we observed many locations in the watershed that either receive more energy early in the season, or remain colder longer into the spring. The snowcover at these sites either ablated earlier or persisted throughout the summer. This is reflected in the snowmelt runoff volumes, which show both initial melt occurring in March and April, and continuing into August and September. However, 87% of the snowmelt runoff occurred in May, June, and July, and these volumes correspond closely with the melt volumes calculated at the ridge and lake sites.

This indicates that the calculated melt volumes are reasonable, even though they are based on generalized characteristics of the snowcover and meteorologic conditions. It also suggests that there is very little lag time between the generation of melt, the initiation of runoff, and the flow of water through the watershed. This is expected, given the small size of the watershed and the general lack of soils. The estimate of precipitation input volumes presented in the tables is intended as the best estimate of input volumes at the ridge and lake sites, and not as the average input over the watershed. Average input, based on measured snowmelt runoff volumes from Emerald Lake outflow for the 1986 water year, is 1.55 m of SWE, which is significantly less than the 2.622 m of SWE indicated for the ridge and lake sites. Several things account for this discrepancy in addition to uncertainty in the measured lake outflow volume. Even at maximum snowcover, snow covered area was not 100%. Steep slopes and jagged ridges did not retain snow. These steep areas are also unlikely to retain the volume of SWE that flatter areas, like the ridge and lake sites do. Moreover, just as the ridge sites appeared to be a re-deposition site, many areas in the upper watershed are probably scour sites, losing much of their snowcover during wind events. All these processes are very difficult to quantify.

9.5. References

Acton, F. S., *Numerical Methods That Work*, 541 pp., Harper and Row, New York, 1970.

Aguado, E., Radiation balances of melting snow covers at an open site in the central Sierra Nevada, California, *Water Resour. Res., 21*, 1649-1654, 1985.

Anderson, E. A., Development and testing of snow pack energy balance equations, *Water Resour. Res., 4*, 19-37, 1968.

Anderson, E. A., A point energy and mass balance model of a snow cover, *NWS Tech. Rep. 19*, 150 pp., NOAA, Washington, DC, 1976.

Anderson, E. A., Streamflow simulation models for use on snow covered watersheds, in *Proc. Modeling Snow Cover Runoff*, edited by S. C. Colbeck and M. Ray, pp. 336-351, U.S. Army Cold Regions Res. Engrg. Lab., Hanover, NH, 1979.

Anderson, E. A. and N. Crawford, The synthesis of continuous snowmelt runoff hydrographs on a digital computer, *Tech. Rep. 36*, 103 pp., Dept. Civil Engrg., Stanford Univ., Stanford, CA, 1964.

Anderson, H. W., Forest-cover effects on snowpack accumulation and melt, Central Sierra Snow Laboratory, *Eos, Trans. Amer. Geophys. Union, 37*, 307-312, 1956.

Andreas, E. L., A new method of measuring the snow-surface temperature, *Cold Regions Sci. Technol., 12*, 139-156, 1986.

Andreas, E. L., W. B. Tucker III, and S. F. Ackley, Atmospheric boundary-layer modification, drag coefficient, and surface heat flux in the Antarctic marginal ice zone, *J. Geophys. Res., 89*, 649-661, 1984.

Andreas, E. L., C. A. Paulson, R. M. Williams, R. W. Lindsay, and J. A. Businger, The turbulent heat flux from Arctic leads, *Boundary-Layer Meteorol., 17*, 57-91, 1979.

Arnfield, A. J., Estimation of diffuse irradiance on sloping, obstructed surfaces: an error analysis, *Arch. Meteorol. Geophys. Bioklim., Ser. B, 30*, 303-320, 1982.

Beaty, C. B., Sublimation or melting: observations from the White Mountains, California and Nevada, U.S.A., *J. Glaciol., 14*, 275-286, 1975.

Bernard, M. and W. T. Wilson, A new technique for the determination of heat necessary to melt snow, *Eos, Trans. Amer. Geophys. Union, 22*, 178-181, 1941.

Bilello, M. A., R. E. Bates, and J. Riley, Physical characteristics of the snow cover, Ft. Greeley, Alaska, 1966-67, *Tech. Rep. 230*, U.S. Army Cold Regions Res. Engrg. Lab., Hanover, NH, 1970.

Bohren, C. F. and B. R. Barkstrom, Theory of the optical properties of snow, *J. Geophys. Res., 79*, 4527-4535, 1974.

Braithwaite, R. J., On glacier energy balance, ablation, and air temperature, *J. Glaciol., 27*, 381-391, 1981.

Brutsaert, W., *Evaporation into the Atmosphere*, 299 pp., D. Reidel, Dordrecht, 1982.

Businger, J., Turbulent transfer in the atmospheric surface layer, in *Workshop on Micrometeorology*, edited by D. A. Haugen, pp. 67-100, Amer. Meteorol. Soc., Boston, 1973.

Charbonneau, R., J. P. Lardeau, and C. Obled, Problems of modeling a high mountainous drainage basin with predominant snow yields, *Hydrol. Sci. Bulletin, 26*, 345-361, 1981.

Charbonneau, R., G. Morin, and J. P. Fortin, Effet du pourcentage et de la distribution des surfaces boisées sur les crues de fonte de neige, *J. Hydrol.*, *41*, 93-103, 1979.

Choudhury, B. J., C. S. Cheng, and A. T. C. Chang, Numerical simulation of the thermal structure of snow packs using an energy balance model: model description and parameter test, *Tech. Mem. 82044*, 30 pp., NASA Goddard Space Flight Ctr., Greenbelt, MD, 1980.

Church, J. E., The melting of snow, *Proc. Central Snow Conf.*, *1*, 21-32, 1941.

Colbeck, S. C., An overview of seasonal snow metamorphism, *Rev. Geophys. Space Phys.*, *20*, 45-61, 1982.

Colbeck, S. C., E. A. Anderson, V. C. Bissel, A. G. Crook, D. H. Male, C. W. Slaughter, and D. R. Wiesnet, Snow accumulation, distribution, melt, and runoff, *Eos, Trans. Amer. Geophys. Union*, *60*, 465-474, 1979.

Collins, E. H., Relationship of degree-days above freezing to runoff, *Eos, Trans. Amer. Geophys. Union*, *15*, 624-629, 1934.

Davies, J. A. and S. B. Idso, Estimating the surface radiation balance and its components, in *Modification of the Aerial Environments of Plants*, edited by J. F. Gerber and B. J. Barfield, ASAE Monogr. 2, pp. 183-210, 1979.

Davis, R. E., Simulation of an alpine soil thermal regime beneath a snowpack, M.A. Thesis, 60 pp., Dept. Geogr., Univ. Calif., Santa Barbara, CA, 1980.

Davis, R. E., J. Dozier, and D. Marks, Micrometeorological measurements and instrumentation in support of remote sensing observations of an alpine snow cover, *Proc. Western Snow Conf.*, *51*, 161-164, 1984.

Davis, R. E. and D. Marks, Undisturbed measurement of the energy and mass balance of a deep alpine snowcover, *Proc. Western Snow Conf.*, *48*, 62-67, 1980.

Dozier, J., A clear-sky spectral solar radiation model for snow-covered mountainous terrain, *Water Resour. Res.*, *16*, 709-718, 1980.

Dozier, J. and D. Marks, Snow mapping and classification from Landsat Thematic Mapper data, *Ann. Glaciol.*, *9*, 97-103, 1987.

Dozier, J. and S. I. Outcalt, An approach toward energy balance simulation over rugged terrain, *Geogr. Anal.*, *11*, 65-85, 1979.

Dozier, J. and S. G. Warren, Effect of viewing angle on the infrared brightness temperature of snow, *Water Resour. Res.*, *18*, 1424-1434, 1982.

Dunne, T. and R. D. Black, Runoff processes during snowmelt, *Water Resour. Res.*, *7*, 1160-1172, 1971.

Dunne, T., A. G. Price, and S. C. Colbeck, The generation of runoff from subarctic snowpacks, *Water Resour. Res.*, *12*, 677-685, 1976.

Fleagle, R. G. and J. A. Businger, *An Introduction to Atmospheric Physics*, 2nd ed., 432 pp., Academic Press, New York, 1980.

Föhn, P. M., Short-term snowmelt and ablation derived from heat- and mass-balance measurements, *J. Glaciol.*, *12*, 275-289, 1973.

Frampton, M. J. and D. Marks, Mapping snow surface temperature from thermal satellite data in the southern Sierra Nevada, *Proc. Western Snow Conf.*, *48*, 88-96, 1980.

Granger, R. J. and D. H. Male, Melting of a prairie snowpack, *J. Appl. Meteorol.*, *17*, 1833-1842, 1978.

Gray, D. M. and D. H. Male, eds., *Handbook of Snow*, Pergamon Press, New York, 1981.

Harstveit, K., Measuring and modelling snowmelt in Dyrdalen, Western Norway, 1979 and 1980, *Nordic Hydrol.*, *12*, 2[illegible]5-246, 1981.

Hendrie, L. K. and A. G. Price, Energy balance and snowmelt in a deciduous forest, in *Proc. Modeling Snow Cover Runoff*, edited by S. C. Colbeck and M. Ray, pp. 211-221, U.S. Army Cold Regions Res. Engrg. Lab., Hanover, NH, 1979.

Horton, R., The melting of snow, *Monthly Weath. Rev.*, *43*, 599-605, 1915.

Idso, S. B., A set of equations for full spectrum and 8- to 14- μ and 10.5- to 12.5- μ thermal radiation from cloudless skies, *Water Resour. Res.*, *17*, 295-304, 1981.

Idso, S. B. and R. D. Jackson, Thermal radiation from the atmosphere, *J. Geophys. Res.*, *74*, 5397-5403, 1969.

Kimball, B. A. and S. B. Idso, A model of thermal radiation from partly cloudy and overcast skies, *Water Resour. Res.*, *18*, 931-936, 1982.

Kuusisto, E., Temperature index, energy balance - or something else?, in *Symposium on the Use of Hydrological Research Basins in Planning*, vol. 1, p. 9, Sonderheft Landeshydrologie, Bern, 1982.

La Casinière, A. C. de, Heat exchange over a melting snow surface, *J. Glaciol.*, *13*, 55-72, 1974.

Langham, E. J., Physics and properties of snowcover, in *Handbook of Snow*, edited by D. M. Gray and D. H. Male, pp. 275-337, Pergamon Press, Toronto, 1981.

Male, D. H. and R. J. Granger, Energy and mass fluxes at the snow surface in a prairie environment, in *Proc. Modeling Snow Cover Runoff*, edited by S. C. Colbeck and M. Ray, pp. 101-125, U.S. Army Cold Regions Res. Engrg. Lab., Hanover, NH, 1979.

Male, D. H. and R. J. Granger, Snow surface energy exchange, *Water Resour. Res.*, *17*, 609-627, 1981.

Male, D. H. and D. M. Gray, Problems in developing a physically based snowmelt model, *Can. J. Civil Engrg.*, *2*, 474-488, 1975.

Marks, D. and J. Dozier, A clear-sky longwave radiation model for remote alpine areas, *Arch. Meteorol. Geophys. Bioklim., Ser. B*, *27*, 159-187, 1979.

Marks, D., R. Kattelmann, J. Dozier, and R. E. Davis, Monitoring snowcover properties and processes in a small alpine watershed, in *Proceedings of Sixth International Northern Research Basins Symposium / Workshop*, edited by H. S. Santeford, pp. 259-275, Mich. Technol. Univ., Houghton, MI, 1986.

Marshall, S. E. and S. G. Warren, Parameterization of snow albedo for climate models, in *Large Scale Effects of Seasonal Snow Cover*, edited by B. E. Goodison, R. G. Barry, and J. Dozier, IAHS-AIHS Publ. 166, pp. 43-50, Intl. Assoc. Hydrol. Sci., Wallingford, UK, 1987.

McKay, D. C. and G. W. Thurtell, Measurements of the energy fluxes involved in the energy budget of a snow cover, *J. Appl. Meteorol.*, *17*, 339-349, 1978.

Miller, S. A., Some snow-melt runoff characteristics, *Eos, Trans. Amer. Geophys. Union*, *31*, 741-745, 1950.

Monteith, J. L., *Principles of Environmental Physics*, 241 pp., Edward Arnold, London, 1973.

Morris, E. M., Sensitivity of the European Hydrological System snow models, in *Hydrological Aspects of Alpine and High-Mountain Areas*, edited by J. W. Glen, IAHS-AIHS Publ. 138, pp. 221-231, Intl. Assoc. Hydrol. Sci., Wallingford, UK, 1982.

Morris, E. M., Modelling of a seasonal snowcover, in *Snow Watch '85*, edited by G. Kukla, R. G. Barry, A. Hecht, and D. Wiesnet, Glaciol. Data report GD-18, pp. 225-240, World

Data Ctr. Glaciol., Boulder, CO, 1986.

Munroe, D. S. and G. J. Young, An operational net shortwave radiation model for glacier basins, *Water Resour. Res.*, *18*, 220-230, 1982.

Obled, Ch. and H. Harder, A review of snow melt in the mountain environment, in *Proc. Modeling Snow Cover Runoff*, edited by S. C. Colbeck and M. Ray, pp. 179-204, U.S. Army Cold Regions Res. Engrg. Lab., Hanover, NH, 1979.

Obled, Ch. and B. Rosse, Mathematical models of a melting snowpack at an index plot, *J. Hydrol.*, *32*, 139-163, 1977.

Olyphant, G. A., Insolation topoclimates and potential ablation in alpine snow accumulation basins: Front Range, Colorado, *Water Resour. Res.*, *20*, 491-498, 1984.

Olyphant, G. A., Longwave radiation in mountainous areas and its influence on the energy balance of alpine snowfields, *Water Resour. Res.*, *22*, 62-66, 1986.

Olyphant, G. A., The components of incoming radiation within a mid-latitude alpine watershed during the snowmelt season, *Arctic Alpine Res.*, *18*, 163-169, 1986.

Outcalt, S. I., The development and application of a simple digital surface-climate simulator, *J. Appl. Meteorol.*, *11*, 629-636, 1972.

Paltridge, G. W. and C. M. R. Platt, *Radiative Processes in Meteorology and Climatology*, 488 pp., Elsevier, Amsterdam, 1976.

Price, A. G. and T. Dunne, Energy balance computations of snowmelt in a subarctic area, *Water Resour. Res.*, *12*, 686-694, 1976.

Pysklywec, D. W., K. S. Davar, and D. I. Bray, Snowmelt at an index plot, *Water Resour. Res.*, *4*, 937-946, 1968.

Satterlund, D. R., An improved equation for estimating long-wave radiation from the atmosphere, *Water Resour. Res.*, *15*, 1649-1650, 1979.

Sellers, W. D., *Physical Climatology*, 272 pp., Univ. Chicago Press, Chicago, 1965.

Siegel, R. and J. R. Howell, *Thermal Radiation Heat Transfer*, 2nd ed., 862 pp., McGraw-Hill, New York, 1981.

Smith, J. L. and N. Berg, *The Sierra Ecology Project*, vol. III, 104 pp., U.S. Dept. Int., 1982.

Stewart, B. J., Sensitivity and significance of turbulent energy exchange over an alpine snow surface, M.A. Thesis, 41 pp., Dept. Geogr., Univ. Calif., Santa Barbara, CA, 1982.

U.S. Army Corps of Engineers, *Snow Hydrology*, Rep. PB-151660, 437 pp., USACE, Portland, OR, 1956.

Warren, S. G., Optical properties of snow, *Rev. Geophys. Space Phys.*, *20*, 67-89, 1982.

Warren, S. G. and W. J. Wiscombe, A model for the spectral albedo of snow II. Snow containing atmospheric aerosols, *J. Atmos. Sci.*, *37*, 2734-2745, 1980.

Wilson, W. T., Some factors relating the melting of snow to its causes, *Proc. Central Snow Conf.*, *1*, 33-41, 1941.

Wilson, W. T., An outline of the thermodynamics of snow-melt, *Eos, Trans. Amer. Geophys. Union*, *22*, 182-195, 1941.

Wiscombe, W. J. and S. G. Warren, A model for the spectral albedo of snow I. Pure snow, *J. Atmos. Sci.*, *37*, 2712-2733, 1980.

Woo, M. and H. O. Slaymaker, Alpine streamflow response to variable snowpack thickness and extent, *Geogr. Annaler, Ser. A*, *57A*, 201-212, 1975.

Yen, Y.-C., Heat transfer characteristics of naturally compacted snow, *Tech. Rep. 166*, 9 pp., U.S. Army Cold Regions Res. Engrg. Lab., Hanover, NH, 1965.

Yen, Y.-C., Recent studies on snow properties, in *Advances in Hydroscience*, edited by V. T. Chow, vol. 5, pp. 173-214, Academic Press, New York, 1969.

Zuzel, J. F. and L. M. Cox, Relative importance of meteorological variables in snowmelt, *Water Resour. Res.*, *11*, 174-176, 1975.

TABLE 9.1. Selected Studies of Climate, Energy Exchange, and Snowmelt

Horton [1915]	Discussion of the relationship between climatic conditions and the generation of snowmelt.
Collins [1934]	Defined the "degree-day", and evaluated the utility of this parameter as an index to overall climatic conditions.
Bernard & Wilson [1941]	Presentation of a method for calculating the energy required to melt a volume of snow.
Church [1941]	Observations of the effect of climatic conditions on the generation of snowmelt.
Wilson [1941a]	Discussion of the relationship between climate, energy exchange, and the generation of snowmelt.
Wilson [1941b]	Description of the thermodynamics of snowmelt.
Miller [1950]	Showed that air temperature could be used as an index to climate and snowmelt in forested environments where solar radiation and wind were minimized.
Anderson [1956]	Showed that because forest cover reduced diurnal variation in surface climate and energy exchange, it had a strong influence on the generation of snowmelt.
USACE [1956]	General discussion of all aspects of snow hydrology. Recognized that energy balance snowmelt calculations were more accurate in the alpine environment, but recommended statistical-index modeling of snowmelt because of limited climatic data availability.
Anderson & Crawford [1964]	Presentation of a computer modeling technique that could be adapted to either statistical-index or energy balance calculations of snowmelt.
Anderson [1968]	Presentation of a set of equations that could be used to calculate the energy balance of the snowcover.
Pysklywec et al. [1968]	Comparison of energy balance and temperature index calculations of snowmelt at an index plot.
Yen [1969]	Detailed review of research efforts to measure or estimate the physical and thermal properties of snow.
Bilello et al. [1970]	Presentation of results of several years of monitoring physical and thermal properties of the snowcover at a study site in the mountains of southern Alaska.
Dunne & Black [1971]	Snowcover energy balance calculations of snowmelt in a sparse, open forest.
Outcalt [1972]	Presentation of a digital computer model of surface climate and energy balance.
Fohn [1973]	Energy balance calculations of short term melt and mass flux from a glacier snowcover.
Bohren & Barkstrom [1974]	Theoretical discussion of the optical properties of snow.
de La Casinid[1974]	Surface climate and energy transfer monitoring over snow in the French Alps.
Beaty [1975]	Observation of significant snowcover mass loss by direct sublimation from high elevation snowcover in the White Mountains of California.
Male & Gray [1975]	Discussion of the problems developing a physically based energy balance snowmelt model.
Woo & Slaymaker [1975]	Showed that because alpine streamflow responded to the variable distribution of snow a simple statistical-index could not adequately predict snowmelt runoff. To adequately model snowmelt runoff in small alpine watersheds, a more deterministic approach would be required.
Zuzel & Cox [1975]	Evaluation of the relative importance of meteorological variables in estimating energy flux during snowmelt.
Anderson [1976]	Developed and tested an energy balance snowmelt model at a snow study site in northern Vermont.
Dunne et al. [1976]	Discussion of climate, energy exchange, and snowmelt in the Canadian subarctic.
Price & Dunne [1976]	Showed that in the sparse open forests of the subarctic radiation dominated the snowcover energy balance during melt because the trees reduced wind at the snow surface but there was not significant shading.
Obled & Rosse [1977]	Evaluation of the snowcover energy balance at an alpine site in the French Alps.
Granger & Male [1978]	Evaluation of climate, energy exchange, and snowmelt in the Canadian prairie.
McKay & Thurtell [1978]	Energy flux monitoring and snowmelt calculations at a prairie site in Canada.
Anderson [1979]	Review of approaches to modeling snowmelt runoff and streamflow. Concluded that while energy balance models are sometimes more accurate their data requirements prohibit them from operational use.
Andreas et al. [1979]	Discussion of turbulent heat transfer over snow and ice leads surrounded by open water in the Arctic.
Charbonneau et al. [1979]	Discussion of the effect of forest cover on the energy balance and snowmelt runoff in the French Alps.
Colbeck et al. [1979]	General discussion of snow deposition, melt, and runoff, with emphasis on energy exchange.
Dozier & Outcalt [1979]	Simulation of the surface energy balance over rugged terrain using a digital elevation model (DEM) of the terrain structure.
Hendrie & Price [1979]	Energy balance snowmelt calculations under a deciduous forest.
Kuhn [1979]	Monitored energy gradients used to compute heat transfer over a glacier.
Male & Granger [1979]	Presentation of energy and mass flux calculations for a snowcover in the Canadian prairie.
Marks & Dozier [1979]	Developed and tested a model of thermal radiation from clear skies distributed over rugged alpine terrain.
Obled & Harder [1979]	Review of climate, energy exchange, and snowmelt in the mountains.
Choudhury et al. [1980]	Developed a numerical energy balance model of the thermal structure of a snowcover.

Davis [1980]	Simulation of heat flow between snow and soil under conditions typical of the alpine Sierra Nevada.
Davis & Marks [1980]	Discussion of instrumentation and measurement techniques used to monitor snow surface climate and energy exchange over at an alpine study site in the Sierra Nevada.
Dozier [1980]	Developed and tested a spectral model of solar radiation transfer over rugged alpine terrain.
Frampton & Marks [1980]	Investigation of the utility of estimating snow surface temperature from thermal satellite imagery.
Warren & Wiscombe [1980]	Developed a spectral model of snow albedo for snow contaminated by atmospheric aerosols.
Wiscombe & Warren [1980]	Developed a spectral model of snow albedo for pure snow.
Braithwaite [1981]	Discussion of the surface energy balance and glacial ablation. Air temperature could be used as an index to glacial ablation only when the energy balance was dominated by sensible heat exchange.
Charbonneau et al. [1981]	Discussion of difficulty associated with modeling snowmelt runoff from alpine watersheds. Statistical index approaches are usually inadequate.
Gray & Male [1981]	Detailed discussion of all aspects of snow science.
Harstveit [1981]	Discussion of monitoring and modeling snowmelt in western Norway. Energy balance approach is required if meteorological conditions are variable during snowmelt.
Langham [1981]	Detailed review and discussion of measurement, calculation, and appropriate procedures for estimating physical and thermal properties of snow.
Male & Granger [1981]	Review of snow surface energy balance.
Dozier & Warren [1982]	Theoretically determined and verified the variation of snow surface emissivity with viewing angle.
Kuusisto [1982]	Comparison of statistical-index and energy balance snowmelt models to determine the conditions under which each is most appropriate.
Morris [1982]	Discussion of the level of determinism and sensitivity to climatic variation for several snowmelt runoff models in use in Europe.
Munroe & Young [1982]	Presentation of a single wavelength band solar radiation model for use in glacial basins, taking terrain structure into account.
Smith & Berg [1982]	Description of climate, snow deposition and snowmelt in the Sierra Nevada.
Stewart [1982]	Presentation of an approach for calculation of turbulent transfer of heat and mass at the snow surface from a limited set of measurements.
Warren [1982]	Review of optical properties of snow.
Andreas et al. [1984]	Discussion of turbulent transfer calculations and determining surface roughness and drag coefficients under arctic conditions where large surface temperature differences exist over small distances.
Davis et al. [1984]	Description of instrumentation and measurement techniques used to monitor snow surface climate and energy transfer at an alpine study site in the Sierra Nevada.
Olyphant [1984]	Investigation of the relationship between net solar radiation and snowmelt in rugged terrain in the Front Range of Colorado.
Aguado [1985]	Investigation of the snowcover radiation balance in a forest clearing in the central Sierra Nevada.
Andreas [1986]	Developed and tested a hygrometric technique for estimating snow surface temperature.
Marks et al. [1986]	Discussion of measurement strategy and description of instrumentation and measurement techniques used to monitor climate and energy exchange over a remote alpine watershed in the southern Sierra Nevada.
Morris [1986]	Presentation of an energy balance snowmelt runoff model.
Olyphant [1986a]	Discussion of the effect of the terrain structure and the snow surface radiation balance during snowmelt in the Front Range of Colorado.
Olyphant [1986b]	Discussion of the effect of the terrain structure on the importance of thermal radiation to the snowcover energy balance.
Dozier & Marks [1987]	Presentation of a technique that allows correction of satellite imagery for terrain effects in rugged alpine areas.

TABLE 9.2. Solar Radiation Summary
Monthly Totals (MJ m^{-2}), Emerald Lake Watershed, 1986 Snow Season

Month	Solar Irradiance (MJ m^{-2}): I_{sol} (.28–2.8μm)	I_v (.28–.7μm)	% of I_{sol}	I_{nir} (.7–2.8μm)	% of I_{sol}	Net Solar (MJ m^{-2}): $R_{n,sol}$ (.28–2.8μm)	$R_{n,v}$ (.28–.7μm)	% of $R_{n,sol}$	$R_{n,nir}$ (.7–2.8μm)	% of $R_{n,sol}$
Ridge Site										
Nov	250.26	119.24	48	131.02	52	58.4	6.81	12	51.59	88
Dec	217.91	103.17	47	114.74	53	49.54	6.05	12	43.49	88
Jan	245.3	115.38	47	129.92	53	58.05	5.05	9	53.00	91
Feb	251.99	125.83	50	126.16	50	55.83	5.44	10	50.39	90
Mar	350.92	179.53	51	171.39	49	90.36	12.19	13	78.17	87
Apr	573.09	275.77	48	297.32	52	163.42	19.96	12	143.46	88
May	717.71	340.49	47	377.22	53	227.36	34.21	15	193.15	85
Jun	891.05	406.82	46	484.23	54	341.61	54.98	16	286.63	84
Jul	814.19	376.39	46	437.80	54	314.47	52.04	17	262.43	83
Total	4312.42	2042.62	47	2269.8	53	1359.04	196.73	15	1162.31	85
Lake Site										
Nov	210.28	88.71	42	121.57	58	52.64	4.26	8	48.38	92
Dec	191.33	82.10	43	109.23	57	44.87	3.62	8	41.25	92
Jan	217.09	91.71	42	125.38	58	56.17	4.32	8	51.85	92
Feb	254.03	104.76	41	149.27	59	65.95	4.83	7	61.12	93
Mar	449.96	181.24	40	268.72	60	134.52	11.43	9	123.09	92
Apr	628.03	253.71	40	374.32	60	198.84	18.43	9	180.41	91
May	786.31	318.09	40	468.22	60	266.55	30.02	11	236.53	89
Jun	874.45	338.11	39	536.34	61	368.56	46.84	13	321.72	87
Jul	827.6	320.91	39	506.69	61	352.87	45.39	13	307.48	87
Total	4439.08	1779.34	40	2659.74	60	1540.97	169.14	11	1371.83	89

TABLE 9.3. Net All-Wave Radiation Summary
Monthly Totals (MJ m^{-2}), Emerald Lake Watershed, 1986 Snow Season

Month	R_n (.28–50μm)	$R_{n,sol}$ (.28–2.8μm)	% of R_n	$R_{n,lw}$ (3.5–50μm)	% of R_n
Ridge Site					
Nov	−188.11	58.4	19	−246.51	81
Dec	−270.82	49.54	13	−320.36	87
Jan	−197.81	58.05	18	−255.86	82
Feb	−183.11	55.83	19	−238.94	81
Mar	−78.93	90.36	35	−169.29	65
Apr	−16.45	163.42	48	−179.87	52
May	68.67	227.36	59	−158.69	41
Jun	214.4	341.61	73	−127.21	27
Jul	225.12	314.47	78	−89.35	22
Total	−427.04	1359.04	43	−1786.08	57
Lake Site					
Nov	−139.39	52.64	22	−192.03	78
Dec	−261.86	44.87	13	−306.73	87
Jan	−199.44	56.17	18	−255.61	82
Feb	−174.72	65.95	22	−240.67	78
Mar	−90.85	134.52	37	−225.37	63
Apr	7.24	198.84	51	−191.60	49
May	95.34	266.55	61	−171.21	39
Jun	232.62	368.56	73	−135.94	27
Jul	249.07	352.87	77	−103.80	23
Total	−281.99	1540.97	46	−1822.96	54

TABLE 9.4. Turbulent Transfer Summary
Monthly Totals, Emerald Lake Watershed, 1986 Snow Season

Month	Net ($H + L_v E$)	H ($MJ\ m^{-2}$)	% of Net	$L_v E$ ($MJ\ m^{-2}$)	% of Net	Mass Flux ($kg\ m^{-2}$)
Ridge Site						
Nov	–118.54	27.18	16	–145.72	–84	–51.24
Dec	–69.69	1.09	2	–70.78	–98	–24.71
Jan	–160.97	17.54	9	–178.51	–91	–61.31
Feb	–114.19	20.00	13	–134.19	–87	–54.29
Mar	–143.32	32.08	15	–175.40	–85	–61.31
Apr	–156.41	70.48	24	–226.89	–76	–83.27
May	–22.19	175.45	47	–197.64	–53	–64.66
Jun	85.57	290.76	59	–205.19	–41	–73.20
Jul	110.32	302.06	61	–191.74	–39	–64.05
Aug	110.43	351.61	59	–241.18	–41	–87.54
Total	–478.99	1288.25	42	–1767.24	58	–625.58
Lake Site						
Nov	–72.72	20.80	18	–93.52	–82	–33.86
Dec	–155.03	54.73	21	–209.76	–79	–73.20
Jan	–141.05	43.40	19	–184.45	–81	–64.36
Feb	–73.59	17.74	16	–91.33	–84	–35.69
Mar	–73.07	48.21	28	–121.28	–72	–43.01
Apr	–86.44	39.77	24	–126.21	–76	–46.06
May	–10.69	131.74	48	–142.43	–52	–49.41
Jun	55.83	241.93	57	–186.10	–43	–65.88
Jul	60.00	182.48	60	–122.48	–40	–39.96
Aug	84.32	183.83	65	–99.51	–35	–35.69
Total	–412.44	964.63	41	–1377.07	59	–487.12

TABLE 9.8. Snowcover Energy and Mass Balance Summary
Monthly Totals, Emerald Lake Watershed, 1986 Snow Season

Month	Energy Transfer (MJ m^{-2})					Mass Flux (kg m^{-2})		
	R_n	$H + L_v E$	G	M	ΔQ	E_S	q_{melt}	$[\rho_{pp} \times z_{pp}]$
Ridge Site								
Nov	-188.11	-118.54	17.15	-0.24	-289.75	-51.2	0.0	298
Dec	-270.82	-69.69	13.53	0.10	-326.88	-24.7	0.0	413
Jan	-197.81	-160.97	10.28	-0.42	-348.92	-61.3	0.0	152
Feb	-183.11	-114.20	8.67	6.35	-282.29	-54.3	0.0	1249
Mar	-78.92	-143.32	6.00	-1.78	-218.02	-61.3	0.0	427
Apr	-16.45	-156.42	3.97	0.02	-168.87	-83.3	0.0	49
May	85.63	-22.19	2.61	-0.12	65.93	-64.7	-197.6	34
Jun	214.41	85.57	1.46	0.00	301.44	-73.2	-903.6	0
Jul	225.12	110.32	4.93	0.00	340.37	-64.1	-1020.3	0
Total						-538.1	-2121.5	2622
Lake Site								
Nov	-139.39	-72.72	21.93	-0.24	-190.42	-33.9	0.0	298
Dec	-261.52	-155.03	20.45	0.10	-396	-73.2	0.0	413
Jan	-199.43	-141.05	15.14	-0.42	-325.76	-64.4	0.0	152
Feb	-174.24	-73.59	11.86	6.35	-229.62	-35.7	0.0	1249
Mar	-90.94	-73.07	8.46	-1.78	-157.33	-43.0	0.0	427
Apr	6.83	-86.44	4.46	0.02	-75.13	-46.1	0.0	49
May	101.71	-10.69	2.77	-0.12	93.66	-49.4	-280.8	34
Jun	232.62	55.83	1.47	0.00	289.93	-65.9	-869.1	0
Jul	249.06	60.00	3.69	0.00	312.75	-40.0	-937.5	0
Total						-442.4	-2087.4	2622

TABLE 9.9. Snowcover Energy Balance Summary Monthly Percentages, Emerald Lake Watershed 1986 Snow Season

Month	Percent Energy Transfer R_n	$H+L_vE$	G	M
Ridge Site				
Nov	58	37	5	0
Dec	77	20	3	0
Jan	54	44	2	0
Feb	59	36	3	2
Mar	34	62	3	1
Apr	10	88	2	0
May	78	20	2	0
Jun	71	28	1	0
Jul	66	32	3	0
Lake Site				
Nov	59	31	10	0
Dec	60	35	5	0
Jan	56	40	4	0
Feb	65	28	5	2
Mar	52	42	5	1
Apr	7	88	5	0
May	88	10	2	0
Jun	80	19	1	0
Jul	80	19	1	0

TABLE 9.10. Snowcover Mass Balance Summary Monthly Percentages, Emerald Lake Watershed 1986 Snow Season

Percent Mass Flux

Month	Precip	Snowmelt Runoff	Ridge Site Evap	Melt	Lake Site Evap	Melt
Nov	11	0	−2	0	−1	0
Dec	16	0	−2	0	−3	0
Jan	6	0	−2	0	−2	0
Feb	48	0	−2	0	−1	0
Mar	16	−1	−2	0	−2	0
Apr	2	−5	−3	0	−2	0
May	1	−23	−3	−8	−2	−11
Jun	0	−38	−3	−35	−3	−33
Jul	0	−26	−2	−39	−2	−36
Total	100	−83	−21	−81	−17	−80

TABLE 9.11. Estimated Parameter Uncertainty Melting Conditions, Emerald Lake Watershed, Spring 1986

	Parameter	Uncertainty
Radiation:	$R_{n,sol}$	$\pm 10\ W\ m^{-2}$
	$R_{n,lw}$	$\pm 10\ W\ m^{-2}$
	R_n	$\pm 20\ W\ m^{-2}$
	I_v	$\pm 10\ W\ m^{-2}$
	I_{nir}	$\pm 5\ W\ m^{-2}$
	ρ_v	± 0.01
	ρ_{nir}	± 0.02
	I_{lw}	$\pm 10\ W\ m^{-2}$
	ε_s	± 0.001
	T_s	$\pm 0.01°C$
Turbulent Transfer:	H	$\pm 14\ W\ m^{-2}$
	L_vE	$\pm 6\ W\ m^{-2}$
	T_a	$\pm 0.4°C$
	T_s	$\pm 0.01°C$
	e_a	± 25 Pa
	e_s	± 0.5 Pa
	u	$\pm 0.5\ m\ s^{-1}$
	z_0	± 0.0001 m
Conduction:	G	$\pm 0.5\ W\ m^{-2}$
	T_g	$\pm 0.25°C$
	$T_{s,l}$	$\pm 0.25°C$
	ρ_s	$\pm 25\ kg\ m^{-3}$
Advection:	M	$\pm 0.1\ W\ m^{-2}$
	T_{pp}	$\pm 0.5°C$
	T_s	$\pm 0.25°C$
	ρ_{pp}	$\pm 25\ kg\ m^{-3}$
	z_{pp}	± 0.02 m
Energy Balance:	ΔQ	$\pm 40.5\ W\ m^{-2}$

Figure 9.1. Two-band albedo model [after Marshall and Warren, 1987] showing albedo decay with grain growth and cosine of solar zenith angle.

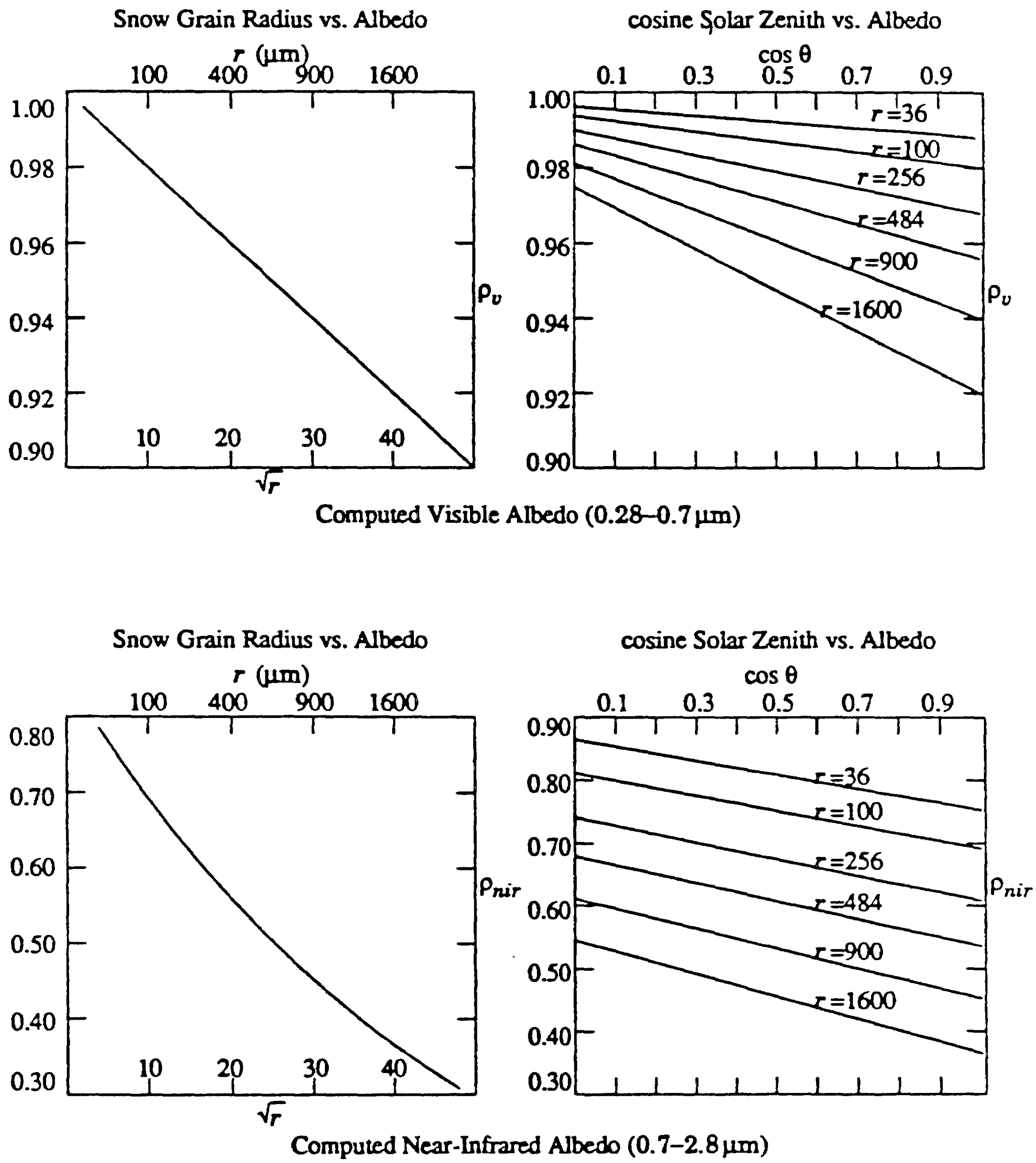

Figure 9.2. Computed vs. measured albedo, two-band (visible: 280 to 700 nm, near-infrared: 700 to 2800 nm) albedo model. Upper curve is visible, lower curve is near-infrared. Smooth curves are modeled, irregular are measured. Each period begins at the end of a snow deposition event. Irregularities in the measured albedos at the beginning of each period are caused by cloud cover and continued snowfall. Flat regions in the measured albedo curves are caused by shadowing during the measurement process. Data from Mammoth Mt. snow study plot, 1986 snow season.

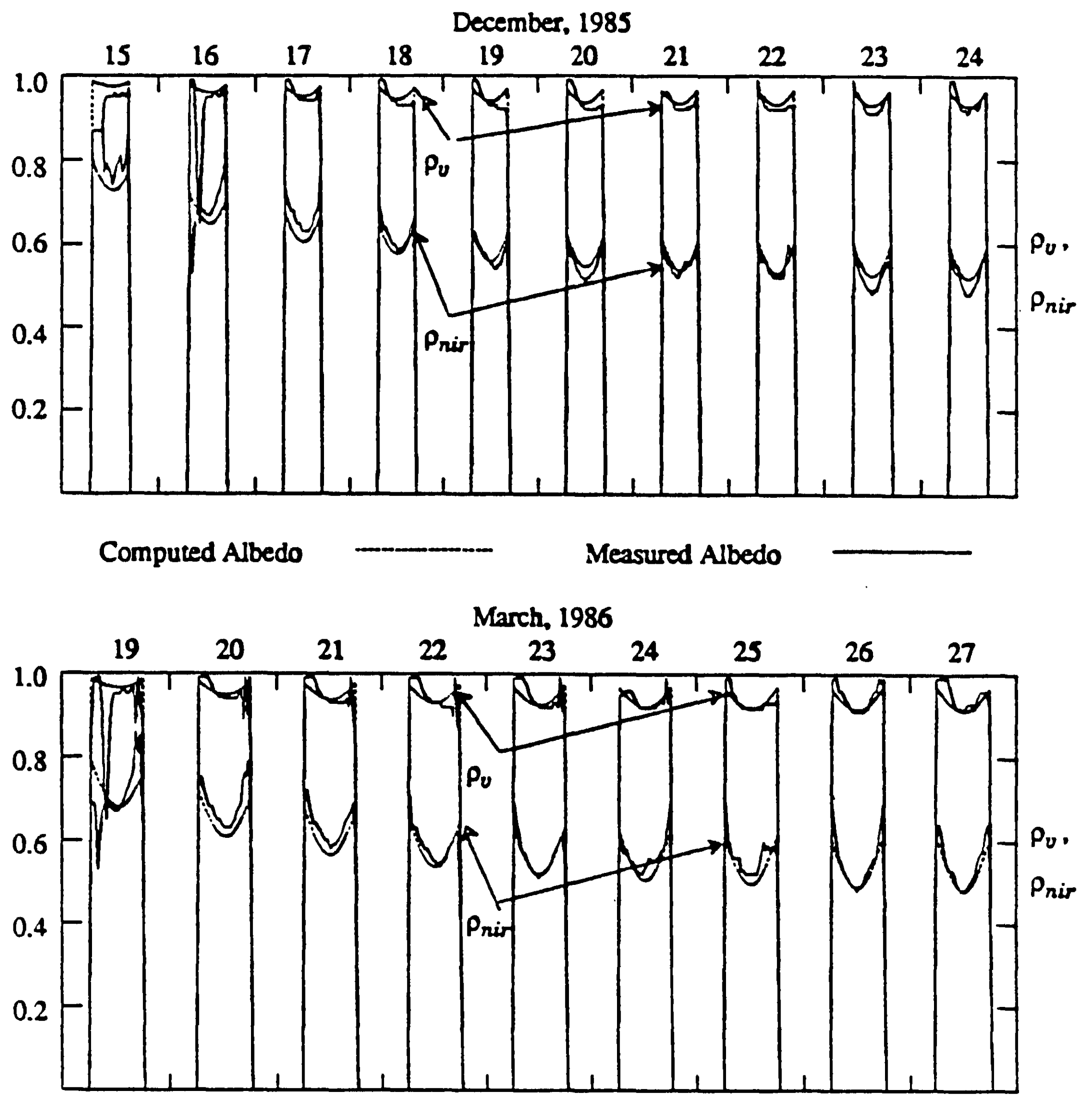

Figure 9.3. Computed two-band albedo, Emerald Lake watershed, 1986 snow season. Width of each function represents magnitude of diurnal increase in albedo with increase in solar zenith angle.

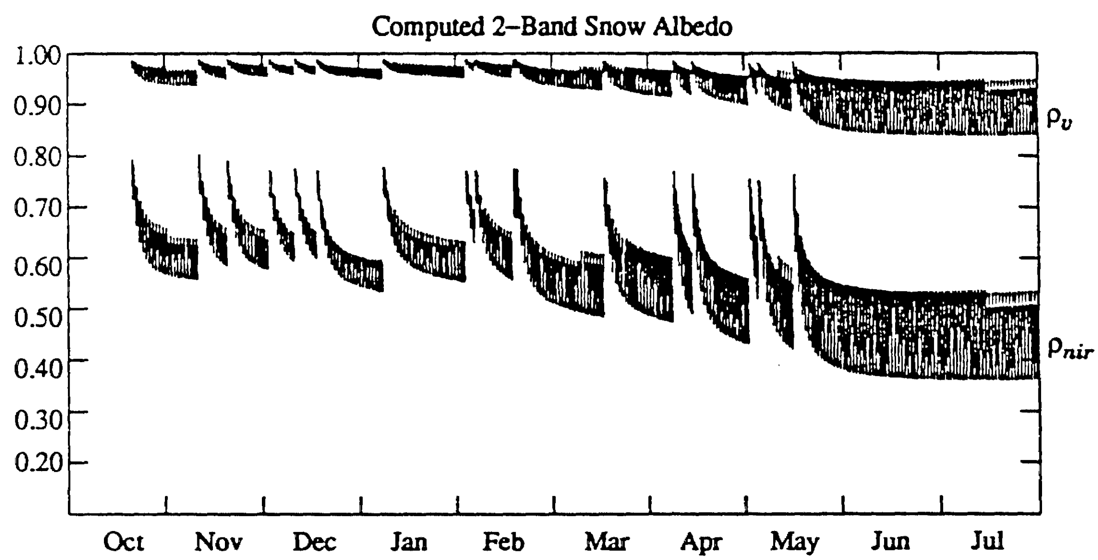

Figure 9.4. Daily average net visible ($R_{n,v}$) (280–700 nm) and near-infrared ($R_{n,nir}$) (700–2800 nm), and net solar radiation ($R_{n,sol}$) (280–2800 nm), ridge site, Emerald Lake watershed, 1986 snow season.

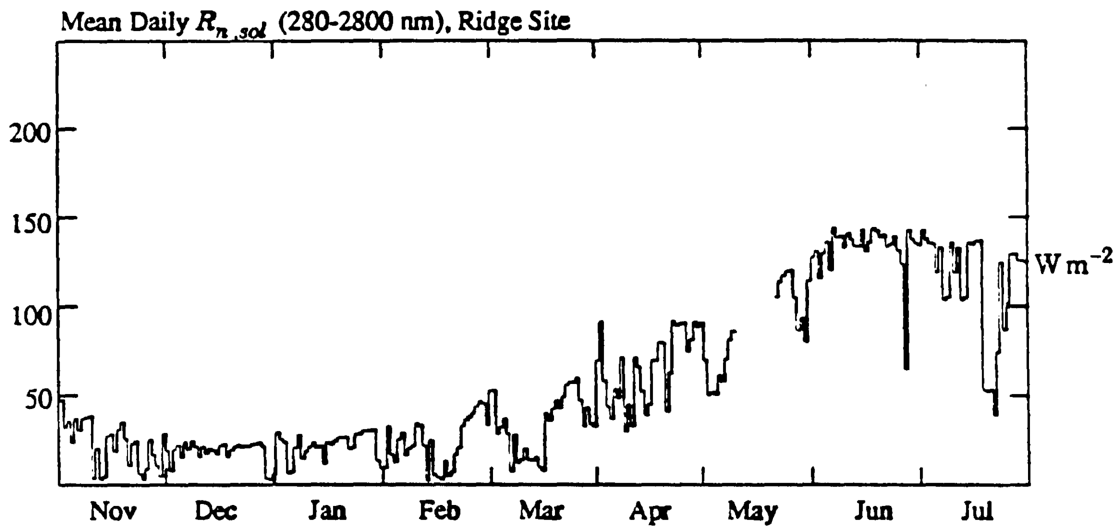

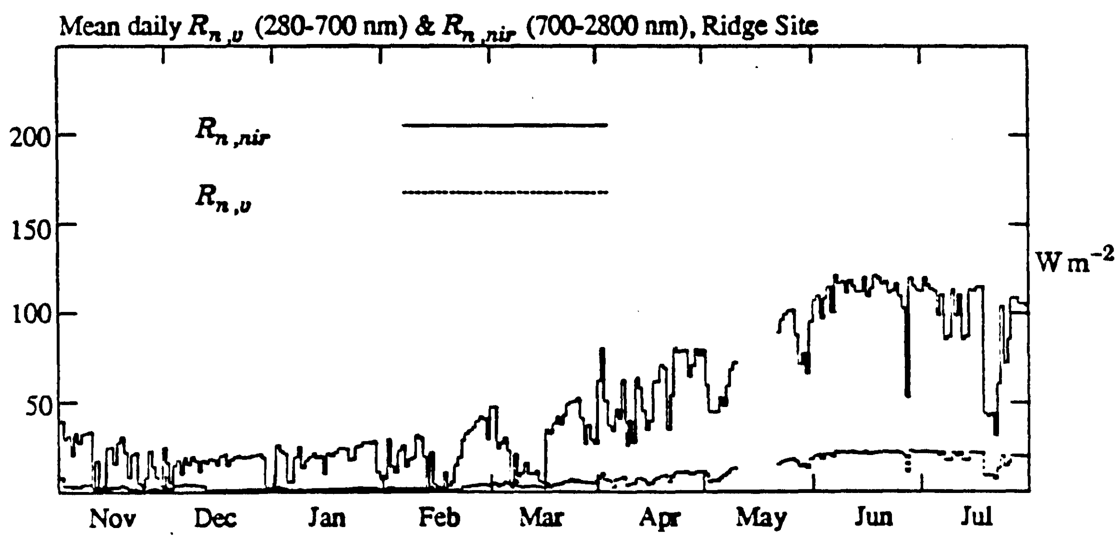

Figure 9.5. Daily average net visible ($R_{n,v}$) (280–700 nm) and near-infrared ($R_{n,nir}$) (700–2800 nm), and net solar radiation ($R_{n,sol}$) (280–2800 nm), lake site, Emerald Lake watershed, 1986 snow season.

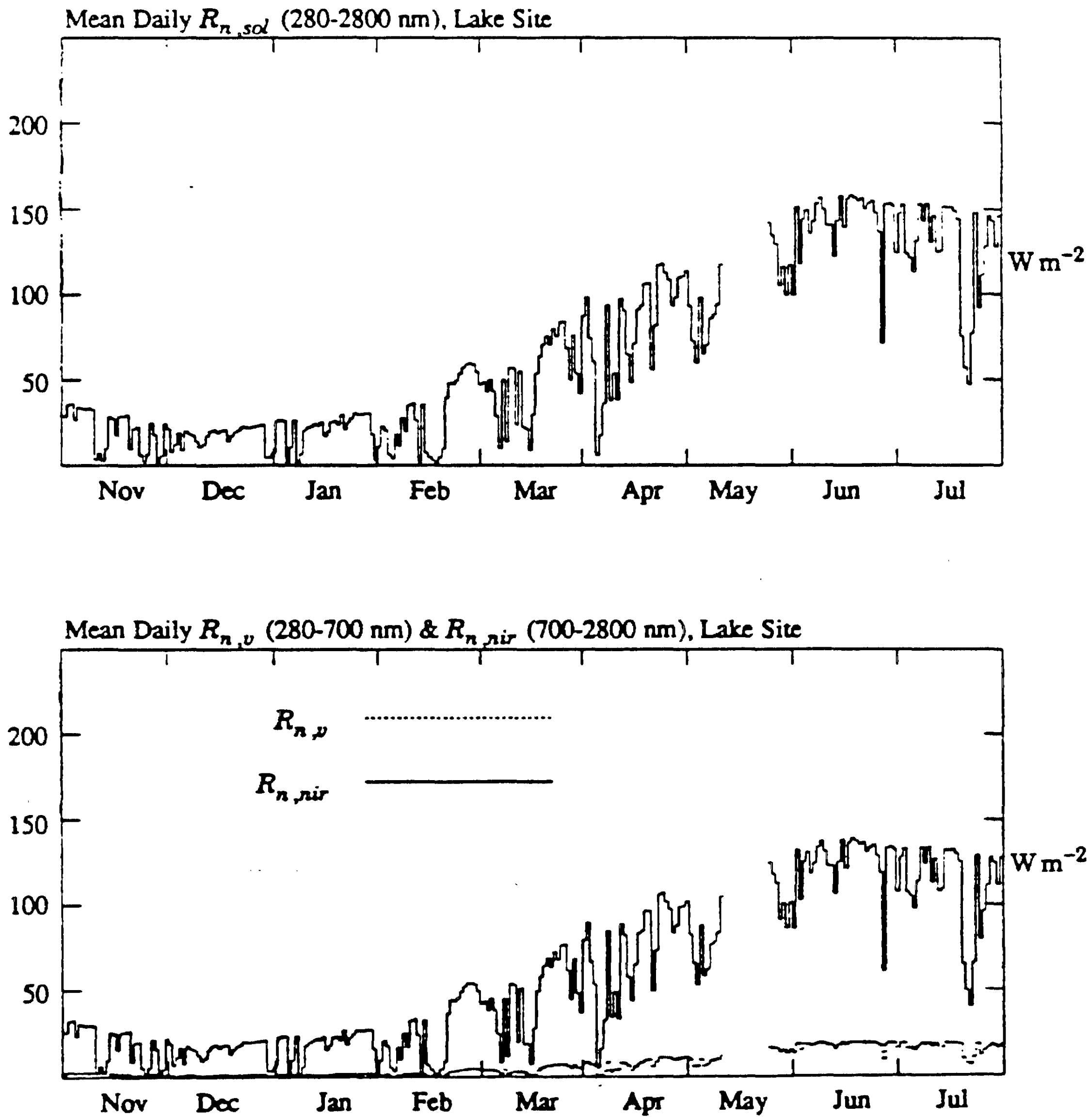

Figure 9.6. Typical hourly solar irradiance (I_{sol}) (280–2800 nm), one diurnal cycle, during winter (mid-December) and spring (mid-June) at the ridge and lake sites, Emerald Lake watershed, 1986 snow season. Hourly values shown were averaged over a 10-day period.

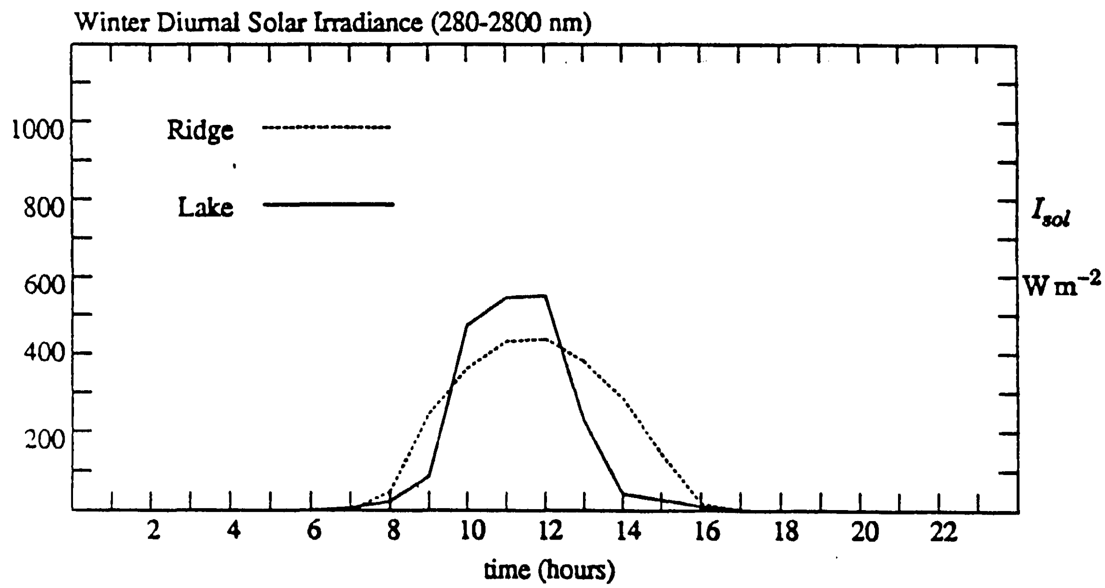

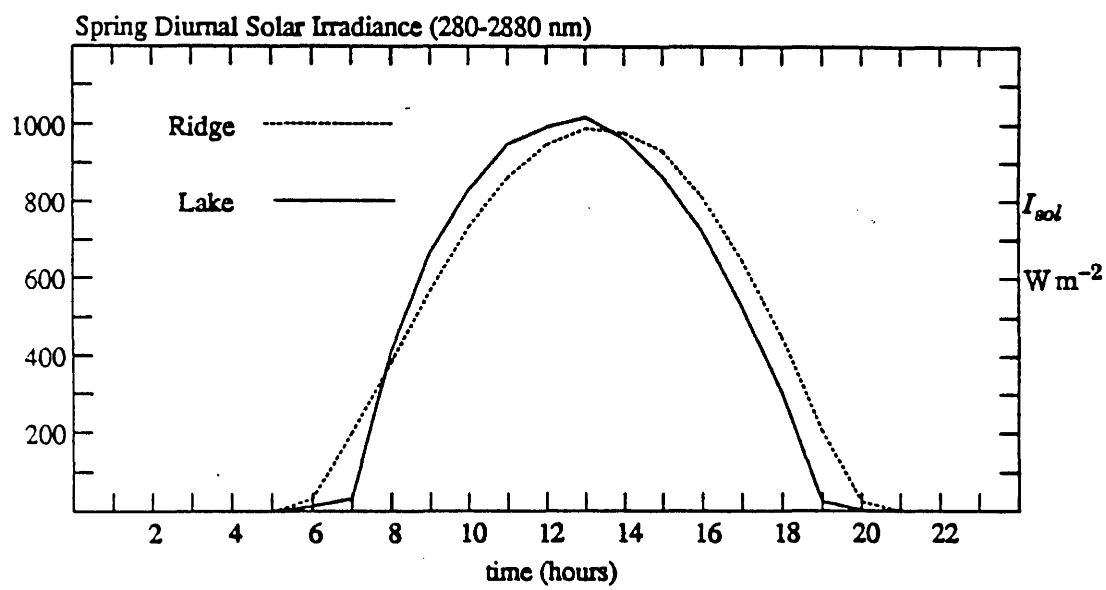

Figure 9.7. Typical hourly net solar ($R_{n,sol}$) (280–2800 nm) radiation, and net visible ($R_{n,v}$) (280–700 nm) and near-infrared ($R_{n,nir}$) (700–2800 nm) radiation, one diurnal cycle, during winter (mid-December) and spring (mid-June) at the ridge and lake sites, Emerald Lake watershed, 1986 snow season. Hourly values shown were averaged over a 10-day period.

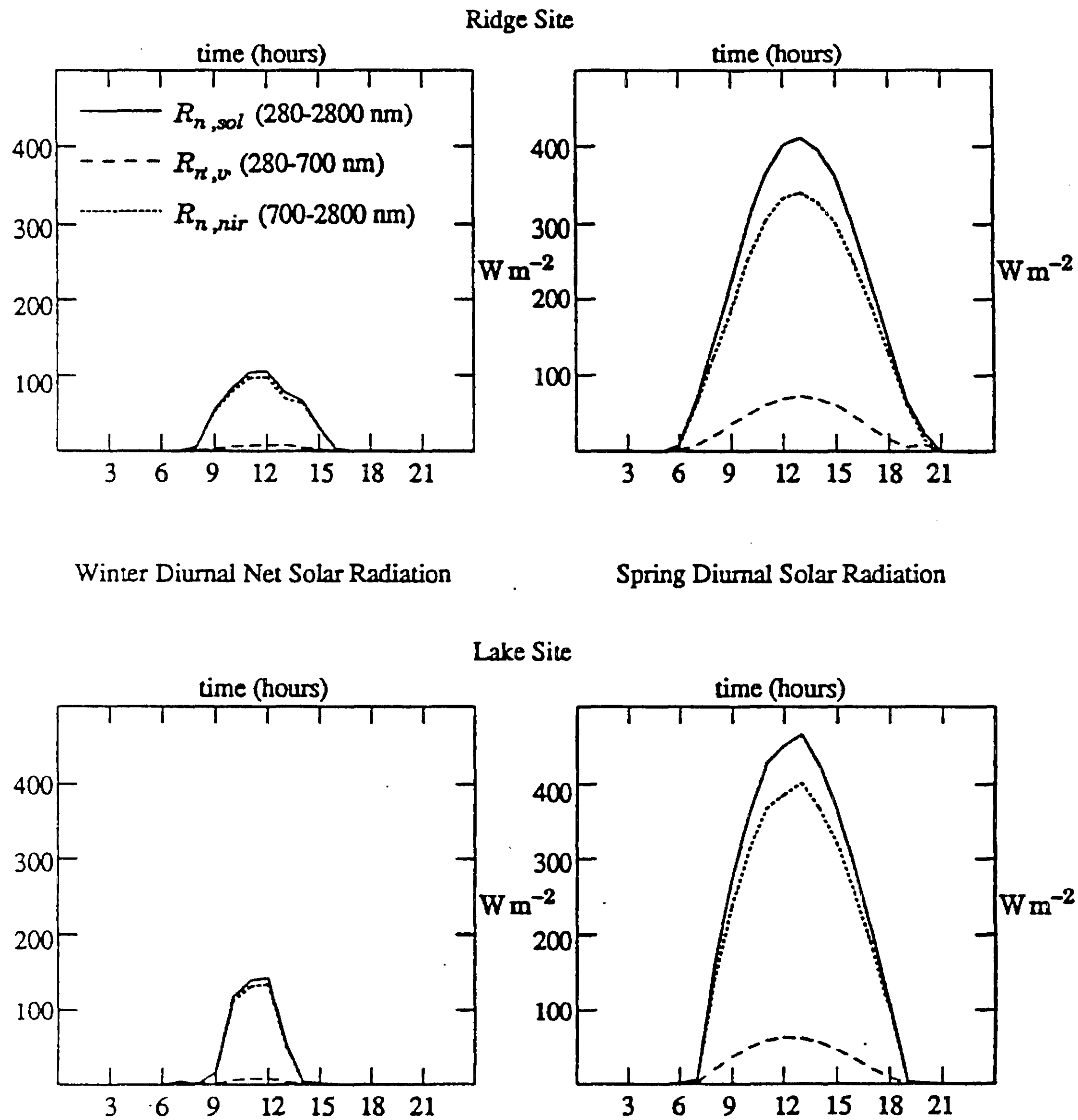

Figure 9.8. Daily average thermal radiation (3.5–50 μm) radiation – irradiance (I_{lw}), exitance ($E_{x,lw}$), and net ($R_{n,lw}$), at the ridge and lake sites, Emerald Lake watershed, 1986 snow season.

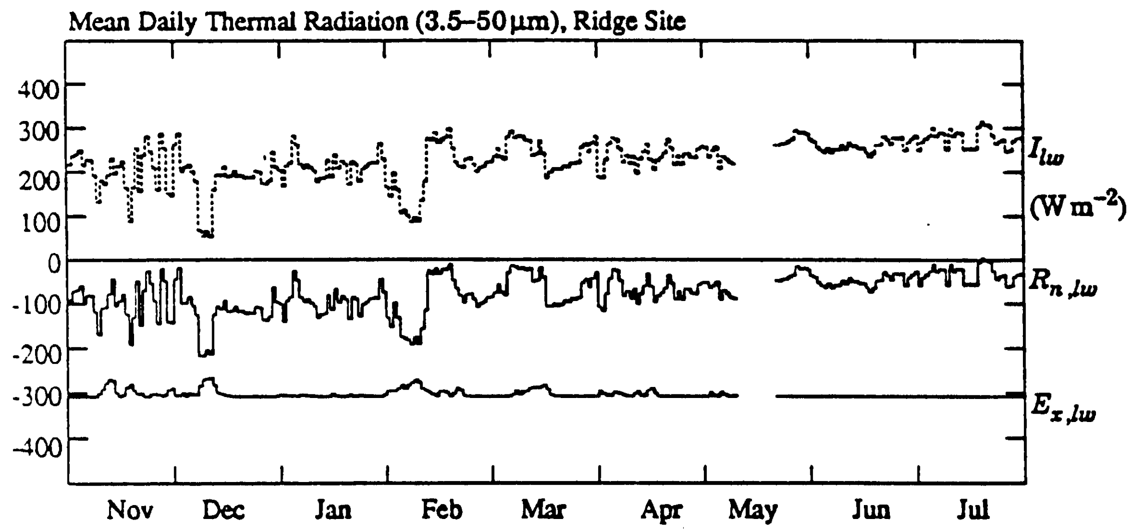

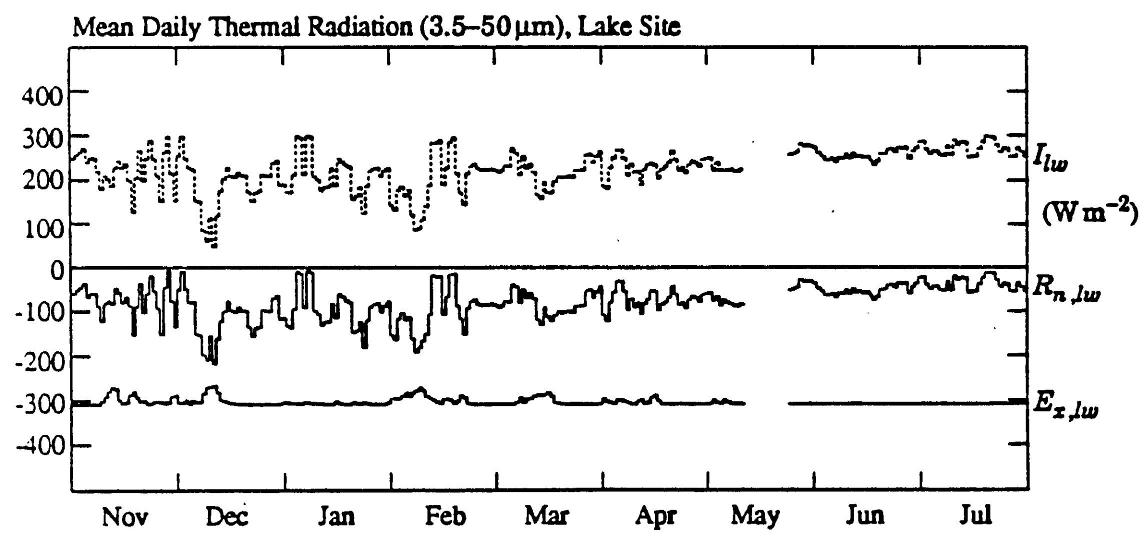

Figure 9.9. Daily average net all-wave radiation (R_n), and net solar ($R_{n,sol}$) (0.28–2.8 µm) and net thermal ($R_{n,lw}$) (3.5–50 µm) radiation at the ridge site, Emerald Lake watershed, 1986 snow season.

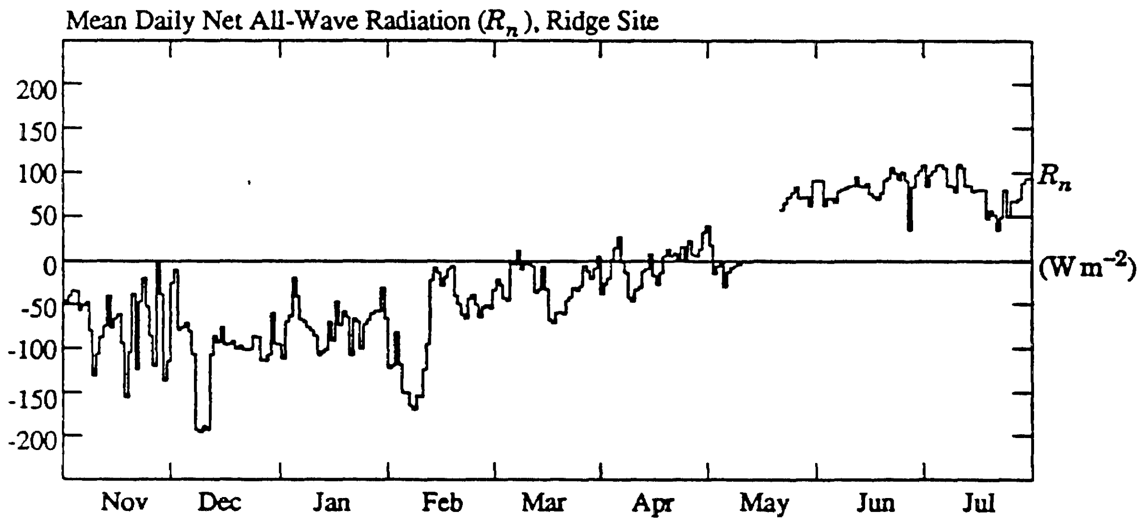

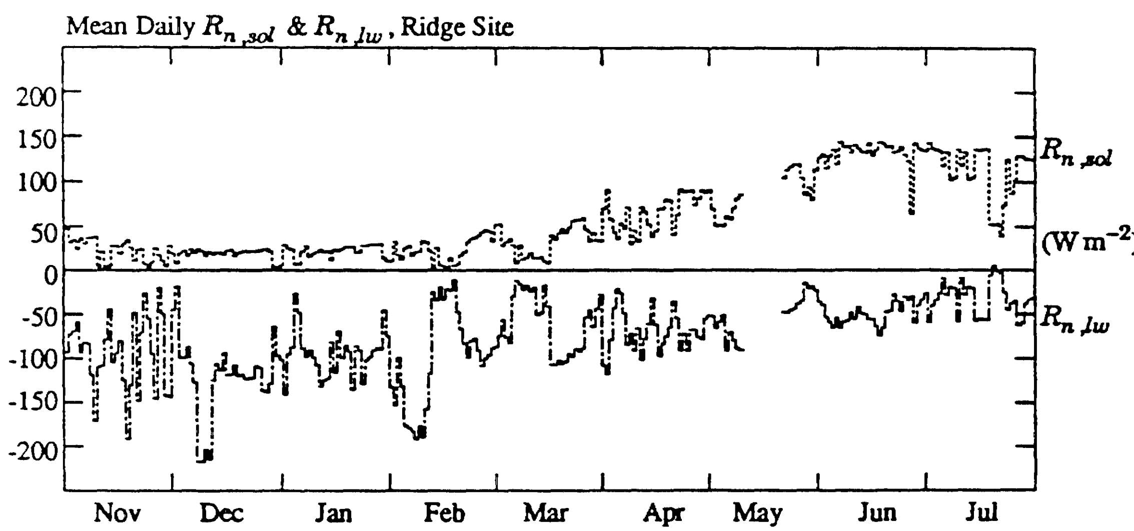

Figure 9.10. Daily average net all-wave radiation (R_n), and net solar ($R_{n,sol}$) (0.28–2.8 μm) and net thermal ($R_{n,lw}$) (3.5–50 μm) radiation at the lake site, Emerald Lake watershed, 1986 snow season.

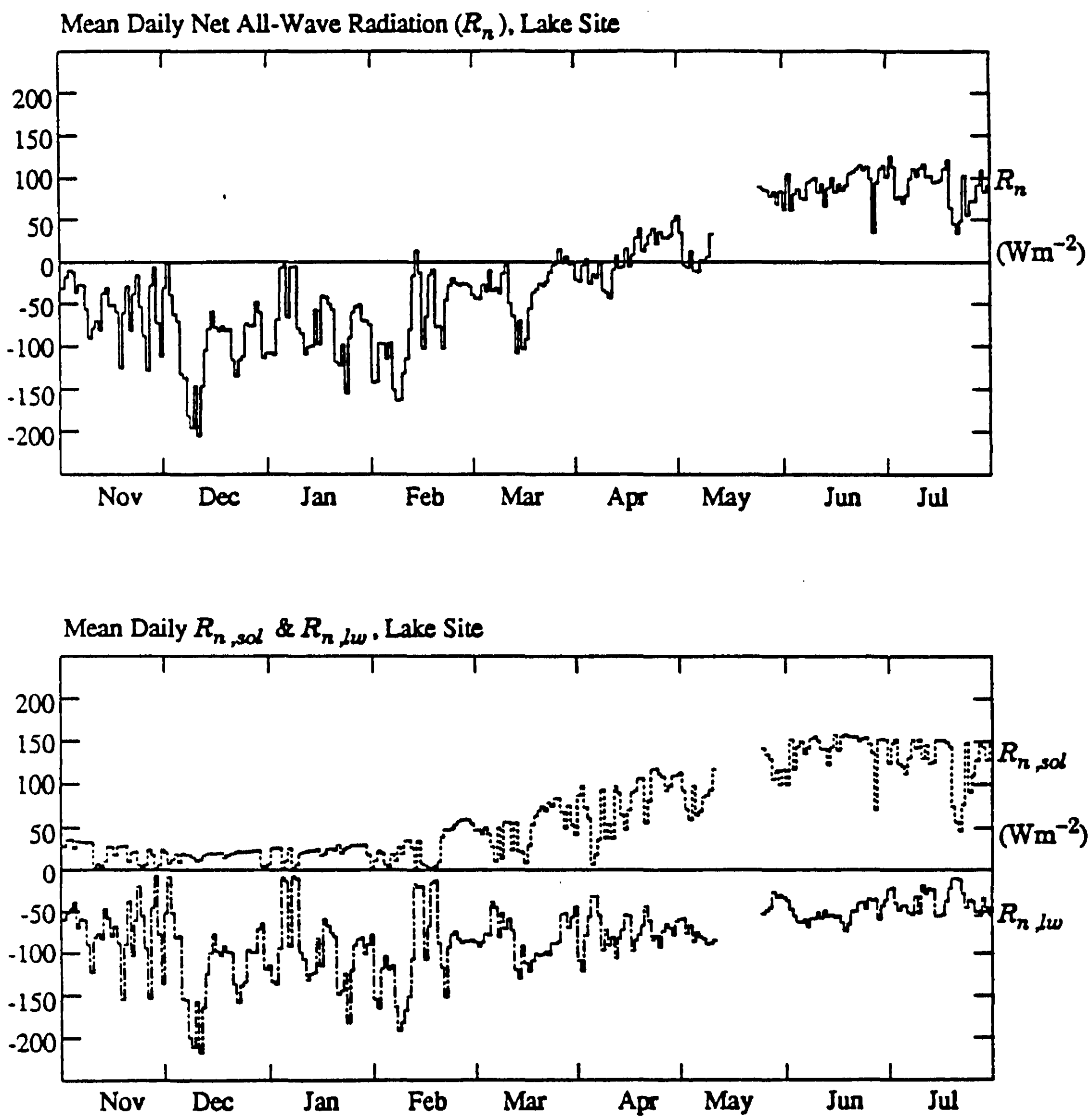

Figure 9.11. Daily average turbulent transfer (H and $L_v E$), ridge and lake sites, Emerald Lake watershed, 1986 snow season.

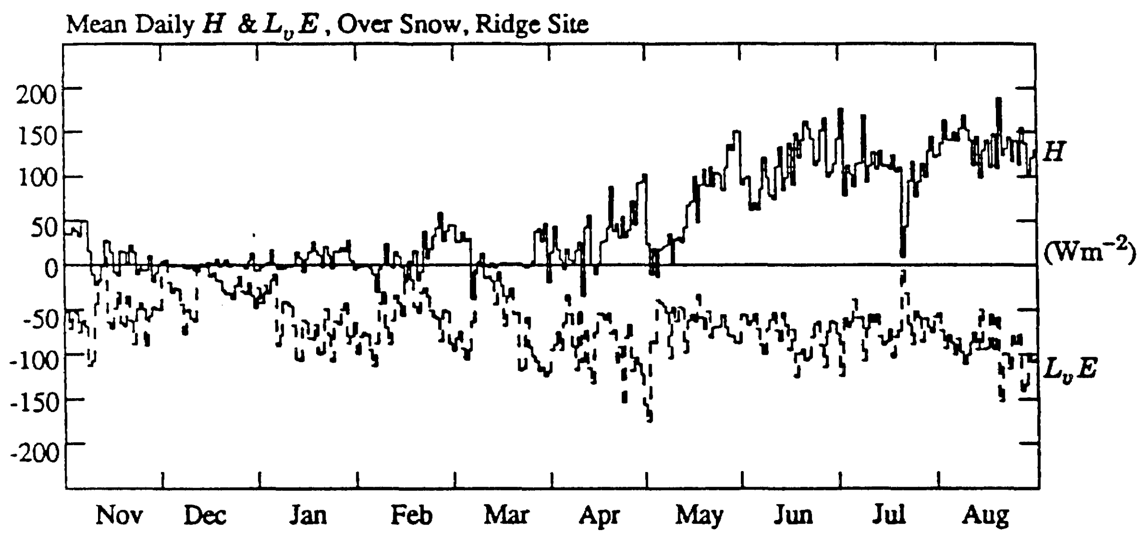

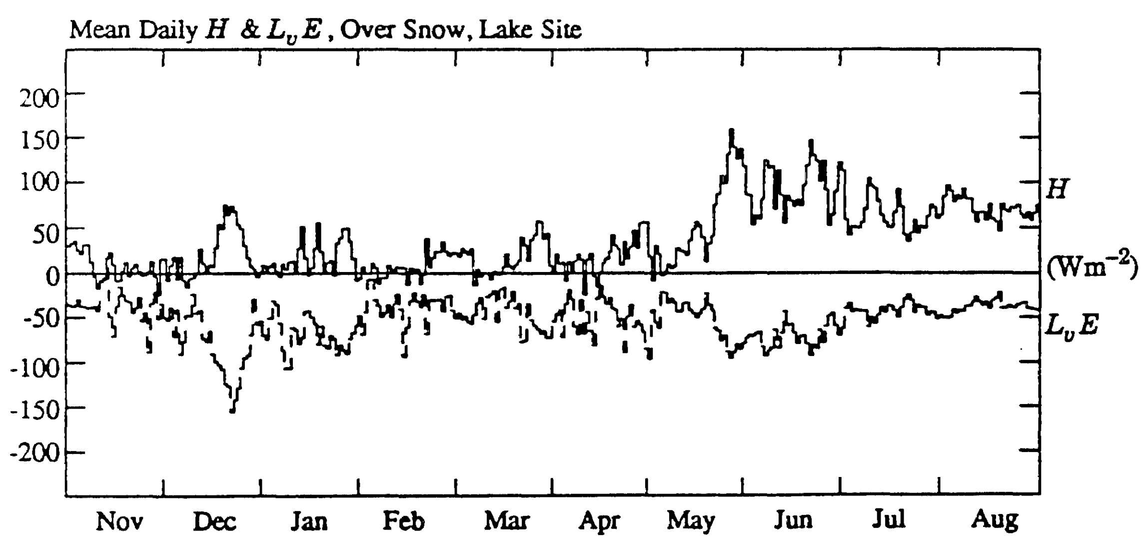

Figure 9.12. Daily average "net" turbulent transfer ($H + L_v E$), ridge and lake sites, Emerald Lake watershed, 1986 snow season.

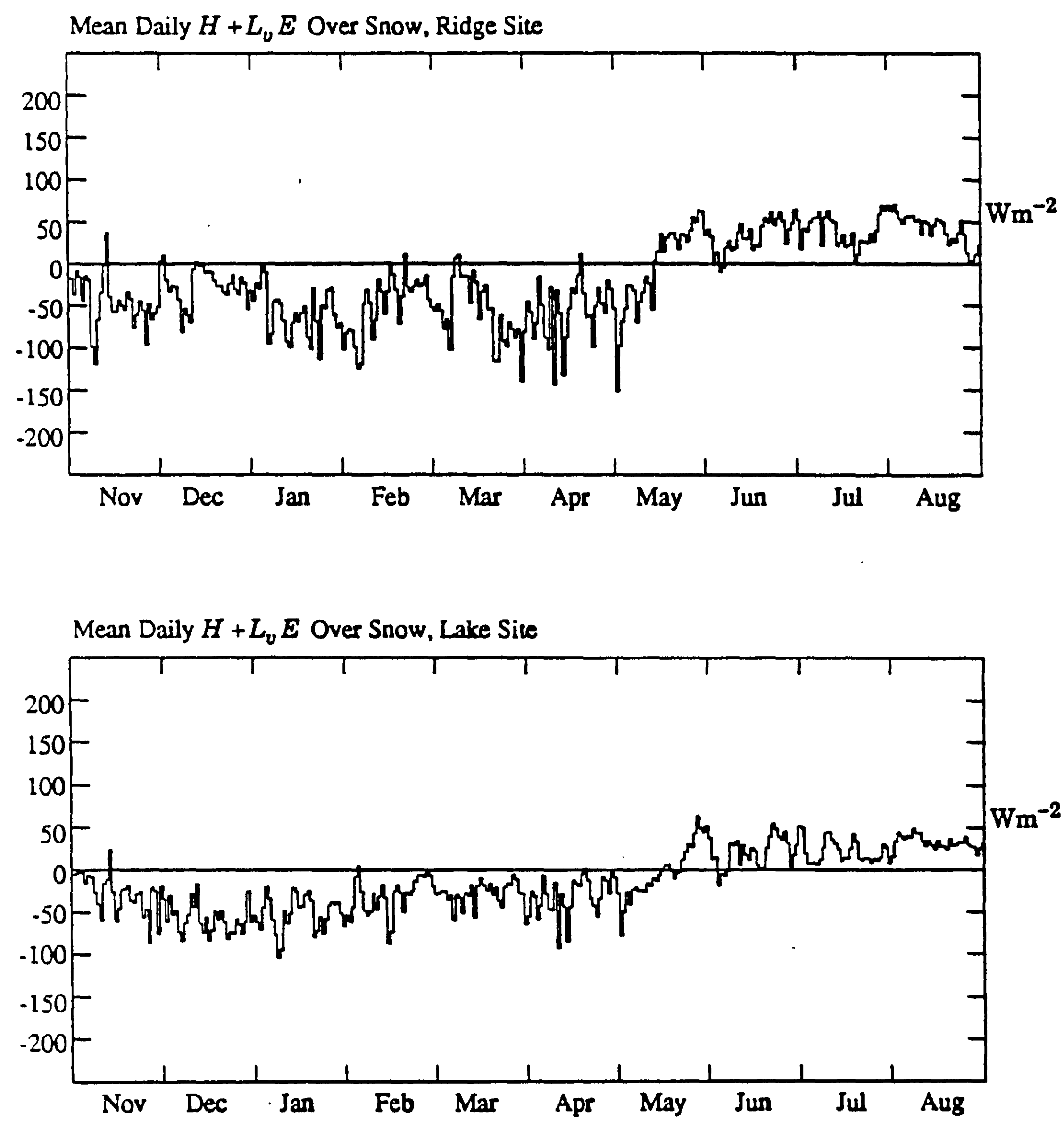

Figure 9.13. Daily average net radiation and "net" turbulent transfer, (R_n and $H + L_v E$) for the ridge and lake sites, Emerald Lake watershed, 1986 snow season.

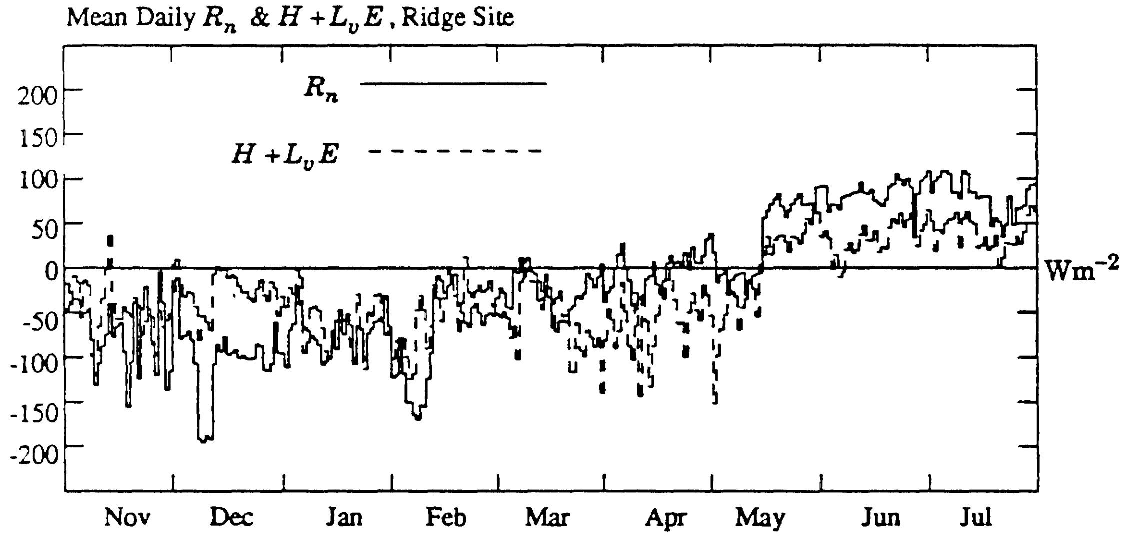

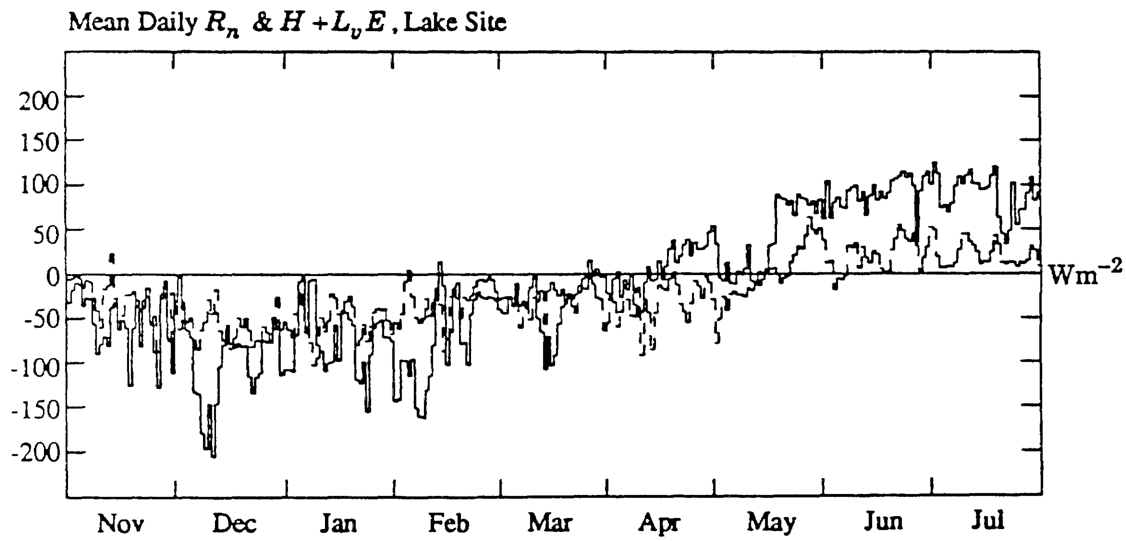

Figure 9.14. Daily average sum of all energy transfer terms $(R_n + H + L_v E + G + M)$ for the ridge and lake sites, Emerald Lake watershed, 1986 snow season.

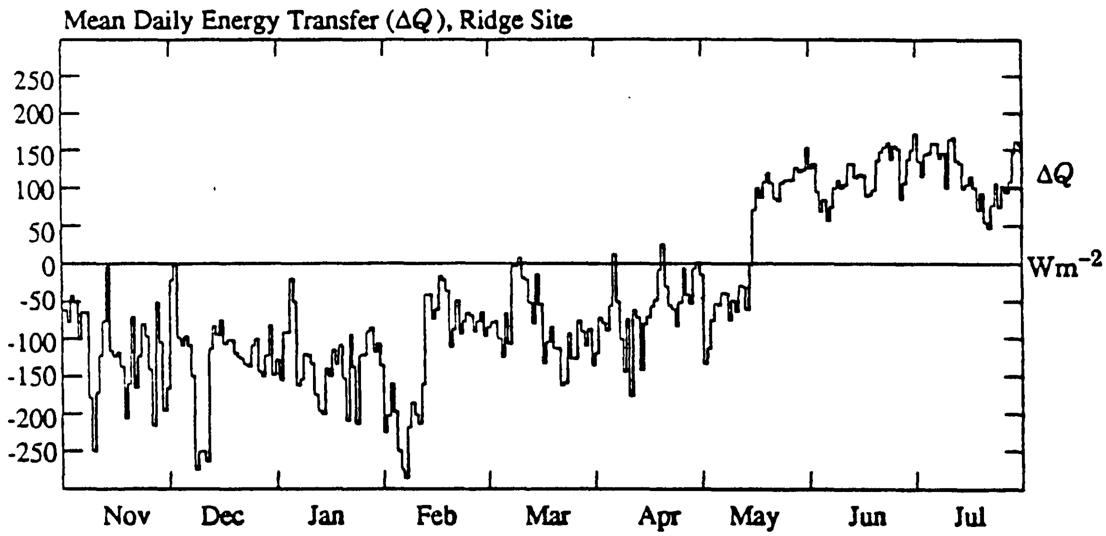

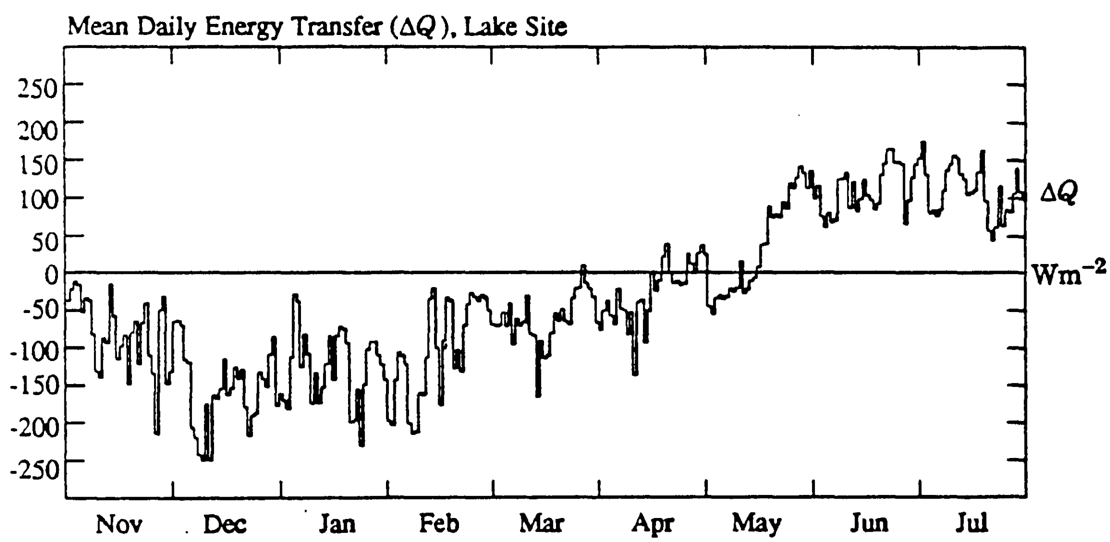

10. Modeling Snowmelt At a Point

As discussed in the previous chapter, the energy balance of a snowcover is expressed:

$$\Delta Q = R_n + H + L_v E + G + M \tag{86}$$

where all quantities have units of $W\,m^{-2}$

ΔQ = Change in snowcover energy,
R_n = Radiant energy flux,
H = Sensible energy flux,
$L_v E$ = Latent energy flux,
G = Heat flux by soil conduction,
M = Heat flux by advection

In equilibrium $\Delta Q = 0$; once the entire snowcover is isothermal at 0.0°C, positive values of ΔQ must result in melt.

In the previous chapter, each of the energy transfer terms has been evaluated in detail. The energy transfer terms were summed and the overall energy budget was examined to evaluate its effect on the mass balance of the seasonal snowcover. This analysis allowed evaluation of the relative importance of each form of energy transfer in the complex snowmelt process. This is the limit of this type of analysis, however, because little information on the actual physical and thermal condition of the snowcover has been included. The interaction between each type of energy exchange, and with the snowcover must also be accounted for. For a more detailed evaluation of energy transfer and snowmelt, an energy balance snowmelt model has been developed so that each of the energy transfer processes previously discussed can be combined with more detailed information on the physical and thermal structure of the snowcover, to account for internal thermal and mass transfer processes. This snowmelt model is designed as a tool to allow analysis of the sensitivity to errors in the input data and simplifying assumptions of predicted snowmelt volumes. This model is an energy balance model of the snowcover and snowmelt at a point, but it will define the type and complexity of the model required to predict the distribution of snowmelt volume over a watershed.

The thermodynamics of snowmelt have been understood for many years. An early discussion of the environmental mechanisms causing snowmelt was presented by Wilson [1941a], a description of the thermodynamics of these by Wilson [1941b], and a technique for calculating snowmelt by Bernard and Wilson [1941]. The U. S. Army Corps of Engineers [USACE, 1956] did a careful evaluation of energy transfer and snowmelt using 10 to 15 years of data from several sites in the Sierra Nevada, concluding that energy transfer measurements and calculations could accurately predict snowmelt volumes. They did not feel at the time, however, that it was feasible to monitor energy transfer for any length of time, due to its complexity, and therefore recommended the temperature-index method for modeling snowmelt. Anderson and Crawford [1964] developed a computational approach that could be used for either statistical or energy balance snowmelt calculations, and Anderson [1968] tested a set of equations in an energy balance snowmelt model. This model gave good results during periods of active melt at an open forested site in the central Sierra Nevada.

Further testing of energy balance calculations of snowmelt was done by Pysklywec et al. [1968] who compared temperature-index and energy balance calculations of snowmelt, finding that in most cases the energy balance approach was more accurate. Dunne and Black [1971] did energy balance snowmelt calculations in a sparse open forest, finding that net radiation was the dominant input. Fohn [1973] used the energy balance approach to predict short term melt and mass flux from a glacier snowcover, and de La Casinière, [1974] monitored energy transfer over snow in the French Alps, also concluding that net radiation provided the dominant input. Kuhn [1979] evaluated methods to compute the energy budget of a glacier. Anderson [1976] presented a detailed energy balance snowmelt model, using several years of data from a well instrumented plot in the Sleepers River Experimental Watershed, Vermont, to test and verify its accuracy. Though this model reliably predicted snowmelt and runoff for a variety of conditions, Anderson concluded its input requirements were too complex and could not be easily satisfied by existing data collection networks. He felt that working to improve more conventional statistical snowmelt models would be a more productive endeavor [Anderson, 1979].

Dunne et al. [1976] investigated energy budget computations and snowmelt in the subarctic, finding that the approach gave accurate results and that net radiation was the most important energy transfer term during snowmelt. Price and Dunne [1976] got similar results at the same subarctic site, finding that in sparse forest cover, wind was reduced, effectively eliminating turbulent transfer. Slope aspect largely controlled the rate of snowmelt because it determined the magnitude of net radiation. Hendrie and Price [1979] had similar findings using the energy balance approach to calculate snowmelt in a deciduous forest, where when the trees were without leaves, solar radiation would dominate the energy budget. Choudhury et al. [1980] developed an energy balance snowmelt model, but were unable to completely test it because of insufficient data. Energy balance computations were used to determine snowmelt rates at prairie sites by Granger and Male [1978], Male and Granger [1979], and McKay and Thurtell [1978]. These studies showed that the method was accurate and that radiation tended to be the most important input. McKay and Thurtell, however, found that the relative importance of radiation, sensible and latent energy transfer was highly variable depending on conditions. During transition periods, when winds tended to be strong and air temperature much colder than the surface, turbulent transfer would replace net radiation as the dominant form of energy transfer. These conditions were, however, unlikely during spring melt.

For the most part, the studies cited above have been restricted to relatively level, low elevation sites. Ground cover, such as trees, deciduous or evergreen, or crop stubble play an important role in controlling the relative magnitudes of energy transfer at such sites, rather than the terrain structure itself. Outcalt [1972] showed that the surface climate and the energy balance could be simulated using a digital computer model driven by relatively simple input data. Obled and Rosse [1977] evaluate energy transfer at an alpine site, and

Obled and Harder [1979] reviewed the snowmelt process in the alpine environment, giving particular attention to the effect of the terrain structure. Dozier and Outcalt [1979] showed that the energy balance could be simulated over rugged terrain, and Morris [1982] presented a detailed discussion of the effect of terrain structure on energy transfer and snowmelt.

Male and Granger [1981], in their review of energy exchange at the snow surface, concluded that the energy balance approach to modeling snowmelt, if reliable data were available, would allow accurate snowmelt computations that would be independent of site considerations. Zuzel and Cox [1975] illustrated the inherent limitations to the temperature-index approach to modeling by showing that while air temperature may be correlated to energy flux, it cannot account for either temporal or spatial variability. Pysklywec et al. [1968] had similar findings, concluding that if meteorological conditions were variable during snowmelt, net radiation was a much better index to snowmelt than air temperature. All felt that snowmelt modeling could be improved by including more than air temperature in the calculations. Braithwaite [1981], however, found air temperature to be a useful index to snowmelt when the energy balance was dominated by sensible heat exchange. Harstveit [1981] concurred with this finding, but pointed out that if meteorological conditions were variable during snowmelt, the energy balance approach was much more effective in predicting snowmelt volumes.

What is clear from the studies cited above is that if meteorological conditions and energy flux are relatively invariant during snowmelt, then the generation of melt water will be uniform, and a statistical approach to modeling snowmelt (like temperature-index) will be effective. However, under most circumstances, these conditions do not occur, particularly in an alpine watershed like Emerald Lake. Kuusisto [1982] points out that the most appropriate snowmelt modeling approach depends on both the site and the type of result required. At Emerald Lake, we know that meteorological conditions vary over the watershed, and therefore expect the generation of melt water to also vary. To evaluate the effect of snowmelt runoff on chemical cycling through the watershed, we must know not only the melt water volume, but the location of its source area. Woo and Slaymaker [1975] noted that in an alpine watershed, the source areas of snowmelt runoff were both spatially and temporally variable. Male and Gray [1975] point out that to develop an effective physically based snowmelt model, the model must be able to account for variability in both the terrain structure and energy flux over the surface. They also point out that methods must be developed to extrapolate point measurements over the area.

The problem with the energy balance approach to modeling snowmelt is that the data requirements are extensive, and these data are not usually collected. Anderson's model [Anderson, 1976] devotes considerable effort to detailed calculations of internal heat transfer and snowcover metamorphism that are not directly related to melt. His model sub-divides the snowcover into multiple layers only a few cm thick, with temperature, density, and liquid water content information required for each layer. Even if this information were available for the snowcover at Emerald Lake, the computational requirements of running such a model on a snowcover that was greater than 5m deep would prohibit its use. The model presented by Choudhury et al. [1980] which required very detailed information about both snow and soil structure, thermal properties, and liquid water content, was never adequately tested, because its data requirements could not be met even at carefully instrumented snow study plots. The complexity of many of the energy balance snowmelt models developed has reduced them to academic exercises, with little or no effort made to apply them to hydrologic problems. To develop a physically based snowmelt model that can be used in a watershed study, we must reduce its complexity. To do this, the snowmelt model presented here is designed to run primarily during the snowmelt season. During this time, the snowcover is more internally homogeneous and can be characterized with fewer measurements. And as shown in the previous section, energy transfer during the melt season is dominated by radiation, which is easily and accurately measured.

Most of the previously cited studies of the energy balance and snowmelt indicate that net radiation is the dominant input. Aguado [1985] found that in a forest clearing in the central Sierra Nevada that energy transfer at the snow surface could be determined from the radiation balance alone most of the time. Olyphant [1986a, 1986b] found that most of the spatial variation in energy transfer at the snow surface in alpine regions of the central Rocky Mountains was due to variations in the solar and thermal radiation balance. As shown by data and calculations of energy transfer in previous sections, this is also the case at Emerald Lake. This is advantageous, because radiation is the only form of energy transfer that can be directly and accurately measured, and investigations of the distribution and/or simulation of radiation transfer over a topographic surface has been undertaken by several investigators [e.g.: Davies and Idso, 1979; Dozier and Outcalt, 1979; Marks and Dozier, 1979; Dozier, 1980; Arnfield, 1982; Munroe and Young, 1982; Siegel and Howell, 1981; Olyphant, 1984, 1986a, 1986b; Dozier and Marks, 1987]. Marks et al. [1986] presented a detailed monitoring strategy for energy balance studies in alpine regions that emphasizes net radiation. The energy balance snowmelt model developed for this study is based on the premise that radiation is the dominant form of energy transfer during snowmelt, and that accurate measurements of radiation are available at one or more points in the watershed. The model also assumes that the snowcover is homogeneous enough that it can be described with only a few measured parameters: average temperature and density, and depth. The model is a point model, that is the preliminary form of a model that will be expanded to run over a watershed. The structure of the model will be thoroughly tested using data from the Emerald Lake study before the final form is determined.

10.1. An Energy Balance Snowmelt Model

The snowmelt model presented here utilizes inputs of radiation, meteorological parameters, measurement heights, and snowcover properties to calculate the energy and mass balance of the snowcover at a point. It predicts melt and runoff, and adjusts the snowcover mass, thermal properties, and measurement heights at each time-step. The modeling approach is similar to that used by Anderson [1976] and Morris [1982, 1986], but the data requirements are simpler and more generalizable. The model is designed to run on a deep, alpine snowcover. It subdivides the snowcover into two layers: a surface layer of constant thickness, and a lower layer made up of the rest of the snowcover. The surface layer is considered the active layer, with its thickness set to the approximate depth of significant solar radiation penetration (the default value is 0.25m). All surface energy transfer occurs in this layer. Both layers are assumed to be homogeneous, and are characterized by the average temperature of each, and a single average density and average liquid water content. Data from Emerald Lake, Mammoth Mt., and the Central Sierra Snow Laboratory, in the southern and central Sierra Nevada indicate that this assumption is reasonable during spring conditions, when both snow temperatures and densities are uniform. During the 1986 snow season at Emerald Lake, this uniformity existed from March on.

The model assumes that energy is transferred between the surface layer and the lower layer, and between the lower layer and the soil by conduction and diffusion. At each time-step, the model calculates the energy balance and then adjusts the temperature and specific mass of each layer. Specific mass, or mass per unit area ($kg\,m^{-2}$) is derived from density × depth ($kg\,m^{-3} \times m$). It is used because it simplifies unit conversions in the model, and because it can be converted directly to a unit-depth or volume of liquid water ($m^{-2}\,m^{-2}$ or $L\,m^{-2}$). In the case of melt or runoff, this term is a flux total for the model time-step, and becomes a specific discharge by dividing by the length of the time-step (seconds), usually dropping the unit area (m^{-2}) in the unit specification: $m\,s^{-1}$, or $m^{-2}\,s^{-1}$, or $L\,s^{-1}$.

If the calculated energy budget is negative, the cold content, or the energy required to bring the temperature of the snowcover to 0.0°C, is increased, and layer temperatures decrease. If the energy budget is positive, layer cold content is decreased until it is zero. Additional input of energy causes the model to predict melt ($kg\,m^{-2}$). If melt occurs, it is assumed to displace air in the snowcover, causing densification, and increasing the average liquid water content of both layers. Liquid water in excess of a specified threshold becomes predicted runoff ($kg\,m^{-2}$). Though meltwater is usually generated in the surface layer, mass lost to runoff is removed from the lower layer. The thickness of the surface layer remains constant until the lower layer is completely melted. At that time, the model treats the snowcover as a single layer.

The model allows input of mass from precipitation (rain or snow), by input of the time of the precipitation event (relative to the beginning of the model run), the precipitation depth, and the average precipitation density and temperature. Precipitation temperature is usually assumed to be the average air temperature during the storm event, but the determination of precipitation type (rain or snow) is based on precipitation temperature. If precipitation temperature is greater than 0.0°C, rain is assumed. Advection is calculated for each input of precipitation, and a new average density, layer content and layer temperatures are calculated, and the thickness of the lower layer, measurement heights and layer specific masses are updated. If rain occurs, it is treated as melt water, increasing the average liquid water content, causing runoff if the threshold value is exceeded.

Snowmelt Model Units

In general, the units for all model initial conditions, constants, inputs, and outputs conform to SI standards, with a few variations. These are the use of specific mass, specific depth, and specific discharge, as discussed above, and the use of decimal hours as the time unit, rather than seconds, as would be the SI standard.

TABLE 10.1. Snowmelt Model Units

height	m
length	m
depth	m
thickness	m
density	$kg\,m^{-3}$
pressure	Pa
temperature	K
energy flux	$W\,m^{-2}$
energy	$J\,m^{-2}$
speed	$m\,s^{-1}$
mass	kg
time	decimal hours
specific mass	$kg\,m^{-2}$
specific depth	m or $m^{-2}\,m^{-2}$
specific discharge	m, m^{-2}, or $L\,s^{-1}$
specific volume	$m^3\,m^{-2}$

Snowmelt Model Constants and Initial Conditions

The snowmelt model presented in this chapter is an interactive point 2-layer energy balance snowmelt model. It was developed on the premise that only limited input data would be available. In its current configuration the model is designed as a tool to help us better determine the range of values used for model constants and coefficients, and to define the minimum data requirements for snowmelt calculations over a watershed. The data required to establish initial conditions and drive the model are relatively simple. Table 10.2 presents a description of all required and optional model inputs.

Initial conditions are set at the beginning of a model run. Some are held constant for the entire run, others are adjusted by the model or updated by additional input data. Run constants are established at the beginning of a model run. Site elevation z_{el} is used to calculate the air pressure P_a from the hydrostatic equation and an assumption of standard sea level air pressure P_0 and a linear temperature lapse rate. The model assumes a constant time-step t_{step}, set at the start of the run. t_{step} is input in decimal hours, but is converted to seconds by the model. Energy and mass fluxes are assumed constant during this time-step. Maximum liquid water threshold is set as a proportion (between 0.0 and 1.0) of the air fraction of the snowcover following the convention set by Davis et al. [1985]:

$$w_c = \frac{V_w}{(V_s - V_i)} \quad (87)$$

where:

w_c = proportion of air fraction displaced by liquid water,
V_w = snowcover volume taken up by liquid water (m^3),
V_s = snowcover volume (m^3),
V_i = snowcover volume taken up by ice (m^3).

Some controversy exists about the water retention capacity of a snowcover, but the volume held is probably relatively small. A reasonable maximum value during active melt is 0.05, but this is much too large for initial melt conditions, and may be too large, if considered an average value for a deep snowcover, for any conditions [Colbeck, 1974a, 1977, 1978a]. The 5% value corresponds to a liquid water retention threshold of about 23 kg m^{-3} (ρ_s = 500 kg m^{-3}, ρ_{ice} = 917 kg m^{-3}), which would have translated into over 100 kg m^{-2} of liquid water, which is far beyond anything observed. A threshold value an order of magnitude less than this (0.5% or 0.005 of the air fraction of the snowcover) is probably more realistic. Liquid water retention can also accelerate densification of the snowcover by systematically reducing the air fraction during freeze-thaw cycles [Colbeck, 1976, 1978b]. If the threshold liquid water retention $w_{c,sat}$ is set too large the model shows very rapid densification. Use of the snowmelt model will help us define what reasonable water retention values are, or show that a more complicated water retention algorithm is required.

The thickness of the surface layer $z_{s,0}$ defines the mass of the snowcover that will be involved in all calculations of surface energy transfer. The temperature of the surface layer is assumed by the model to be the same as the surface temperature of the snowcover. If this layer is too thick, it will have a large thermal inertia, and the diurnal variation in computed surface temperature will be damped and unrealistic. If it is too thin, significant penetration of radiation into the lower layer will occur, causing transfer of energy to the lower layer that is not accounted for by the model. The depth of radiation penetration into snow is variable, depending on grain size and solar zenith angle. However, data from thermistors implanted in the snowcover during melting conditions at the Mammoth Mt. snow study plot indicate that solar heating increased the measured temperatures to above freezing values at depths less than 20 cm, while thermistors at depths below this level tended to record a uniform temperature of 0.0°C [Robert Davis, personal communication]. A surface layer thickness of 0.25 m was selected as the default value for the model, because this seemed to eliminate problems caused by radiation penetration, and yet was thin enough to allow the model to predict a reasonable range of diurnal temperatures. Because the snowcover thickness is in the vertical direction (rather than perpendicular to the soil surface), this may not be true for steeply sloping sites, where a thicker surface layer may be required. If the default surface layer thickness is used, no input is required.

The surface roughness length z_0 is set as a constant for a model run. Over snow, which is fairly smooth, z_0 ranges from 1.0×10^{-4} to 5.0×10^{-3}m, though once vegetation and local terrain features have to be considered, the value could be much higher. As long as the model run is restricted to a period of a few weeks, the assumption of a constant value is valid.

In addition to run constants, two other types of initial conditions must be established at the beginning of each model run: 1) snowcover properties; and 2) measurement heights (for turbulent transfer calculations). Initial conditions for snow properties and measurement heights are set at the beginning of the model run by the first input of these parameters. Input of additional measured values of these parameters to update and verify the model predictions can occur at any time. The time input with the initial snowcover properties defines the start time of the model run. It may be 0.0, but whatever its value, all subsequent times will be considered relative to the start time. Update times must be greater than the start time, but need not fall exactly on a model time-step interval.

Snowcover depth z_S is its total thickness. The thickness of the surface layer $z_{s,0}$ is set as a model constant, and the thickness of the lower layer $z_{s,l} = z_S - z_{s,0}$ depth less the thickness of the surface layer. Mass losses and densification, and input of solid precipitation or condensate cause the model to adjust z_S, which is reflected only in $z_{s,l}$. The model updates z_S and $z_{s,l}$ after each time-step. The model assumes that the density of both layers is uniform. The average snowcover density ρ_S is assigned to both layers. The mass lost to sublimation or evaporation reduces both z_S and ρ_S. Condensation increases z_S without changing ρ_S, if it occurs as a solid. If it occurs as a liquid, it increases mass and density, but not depth. Condensation during rain is assumed to be half solid, and half liquid.

Melt cannot occur until the snow layer temperature reaches 0.0°C. Initial melt increases the density by decreasing depth without decreasing mass. Once the liquid water retention threshold has been reached, the snowcover is considered ripe, and additional melt will result in predicted runoff and will not change the density. Snowcover density is updated at every time-step. Average lower snow layer temperature $T_{s,l}$ is computed as the mass-adjusted difference between T_S and $T_{s,0}$. $T_{s,0}$ and $T_{s,l}$, are constrained to be no larger than T_{melt}. $T_{s,0}$ is considered by the model to be the surface temperature of the snowcover for calculations of energy and mass flux. Both of these snow temperatures are updated at each time-step of the model. New average temperature of the entire snowcover T_S is computed as a mass-weighted average of $T_{s,0}$ and $T_{s,l}$ at the end of each time-step.

The initial and subsequent updates of liquid water content w_c cannot exceed the threshold value $w_{c,sat}$. This parameter represents an average value for the snowcover, and is considered by the model to be uniform in both layers. This is not physically realistic, as evidence suggests that liquid water movement through snow is non-uniform, progressing in diurnal waves [Colbeck, 1972, 1974a, 1974b, 1975, 1978a, 1978c, 1979a; Colbeck and Anderson, 1982]. For a model to adequately predict the flux of liquid water through the snowcover, it would have to be a multi-layer model with more detail devoted to internal thermodynamic and hydraulic processes. The model presented here is rather designed to predict runoff from the snowcover. Because the volume of liquid water retained by the snowcover is relatively small (less that 0.005% of the mass of the snowcover), the exact location of that liquid water within the snowcover is not seen as critical to the prediction of melt during spring. In the model evaporation favors liquid water over ice by the ratio of latent heat of vaporization to sublimation (0.882). Evaporation depletes both liquid water and ice in the surface layer until no liquid water is left. Evaporation or condensation between the snowcover and the atmosphere occurs only in the surface layer. Melt, which is also generated primarily in the surface layer, will increase the liquid water content. Average snowcover liquid water content is updated each time-step.

Measurement heights required for turbulent transfer calculations are as discussed in the previous chapter. Because the first input for measurement heights is used to set the initial conditions for the model run the first time input with measurement heights $t_{z,start}$ must be the same as the time input with the first snowcover properties data. Subsequent update times must be greater than the start time.

Measurement heights for wind speed z_u or air temperature and humidity z_T may be different, or the same. These heights are updated by the model as the total snowcover depth changes. The depth of soil temperature measurement z_g is set constant for the model run. A default value of 0.5 m is set by the model if no value is input with the initial measurement heights.

The model can be updated for the addition of precipitation (rain or snow) at any time after the start of a run. The time of the precipitation event $t_{pp,start}$ must be equal to, or greater than, the start time of the model run. Precipitation depth z_{pp} and density ρ_{pp} are used to calculate the mass added to the snowcover and to adjust the total snowcover depth z_S and average density ρ_S. Compaction is not considered by the model. Precipitation temperature is usually assumed to be the average air temperature during the storm event, but because this parameter is used by the model to differentiate between rain and snow, care must be taken. Snowfall cannot have a temperature above T_{melt} and rain must have a temperature greater than T_{melt}. The model cannot make adjustments for precipitation events that are mixed rain and snow. These should be separated, and input as two separate events. Snowfall will increase both the mass and thickness of the snowcover. Rain will increase the mass, but not the thickness, until the liquid water retention threshold is reached. At that point the model will convert additional rain directly into runoff. The model also calculates advection, as discussed in the previous chapter, from the input precipitation mass and temperature data, using the appropriate heat capacity.

Snowmelt Model Input Data

Table 10.2 also presents a description of the basic input data required to run the snowmelt model. These data are a simplified form of the inputs required for calculating energy transfer, as discussed in the previous chapter. Only inputs required for determination of the energy and mass balance of the snowcover are required. Parameters that can be computed independent of the snowmelt model are modeled separately and the results used in the snowmelt model. All inputs are assumed by the model to be average values over the period of the time-step. Net solar radiation $R_{n,sol}$ is modeled or measured independent of the snowmelt model. As discussed in the previous section, there are a variety of methods to model and measure solar and net solar radiation. None of these depend on information about the thermal condition of the snowcover, which would be supplied by the snowmelt model. Exitant thermal radiation, however, is dependent on surface temperature, so the model calculates net thermal radiation from the input of thermal irradiance and modeled snow surface layer temperature. Air temperature, vapor pressure, and wind speed are combined with modeled snow surface temperature and calculated snow surface vapor pressure to calculate turbulent transfer at each time-step. Energy transfer between the snowcover and the soil is calculated from modeled snowcover properties and measured soil temperature. Air temperature, vapor pressure, wind speed, and soil temperature are assumed by the model to have been measured at the heights set in model initial conditions. The soil temperature measurement depth is constant for the model run, but the other measurement heights are updated by the model if the snow depth changes. Measured runoff from the snowcover is an optional input. If these data are available, the model will calculate the difference, or error in modeled runoff for each time-step.

Energy and Mass Balance Calculations

Once the initial snowcover and measurement height parameters are set, the thermal and mass condition of the snowcover is calculated. First the thickness of the lower snow layer is calculated:

$$z_{s,l} = z_S - z_{s,0} \tag{88}$$

Then specific mass of each layer is calculated:

$$m_{s,0} = z_{s,0}\, \rho_S \tag{89}$$

$$m_{s,l} = z_s\, \rho_S \tag{90}$$

$$m_S = m_{s,0} + m_{s,l} \tag{91}$$

where:

$m_{s,0}$, $m_{s,l}$ = specific mass of snow surface and lower layers (kg m^{-2}),
m_S = specific mass of entire snowcover (kg m^{-2})

Temperature of the snow surface layer $T_{s,0}$ and average temperature for the entire snowcover T_S were either set from input snow conditions or calculated at the end of the last model time-step. Temperature of the lower snow layer $T_{s,l}$ is set by:

$$T_{s,l} = T_S \frac{m_S}{m_{s,l}} - T_{s,0} \frac{m_{s,0}}{m_{s,l}} \tag{92}$$

The cold contents, or the amount of energy (J m^{-2}) required to bring each of the snow layers to the melting temperature is calculated:

$$cc_{s,0} = C_{p\_ice,0}\, m_{s,0}\, [T_{s,0} - T_{melt}] \tag{93}$$

$$cc_{s,l} = C_{p\_ice,l}\, m_{s,l}\, [T_{s,l} - T_{melt}] \tag{94}$$

$$cc_S = cc_{s,0} + cc_{s,l} \tag{95}$$

where:

$cc_{s,0}$, $cc_{s,l}$ = cold content for snow surface and lower layers ($J\,m^{-2}$),
cc_S = cold content for entire snowcover ($J\,m^{-2}$),
C_{p_ice} = specific heat of ice for snow layers ($J\,kg^{-1}K^{-1}$).

The specific heat of ice for each layer is calculated as a function of layer temperature, as discussed in the previous chapter. Note that because the temperature of the snow layers is constrained to be no greater than 0.0°C, the value of the layer cold contents $cc_{s,0}$ and $cc_{s,l}$ is always negative and cannot be greater than 0.0.

Once these calculations have been made the model reads the input data to calculate the energy budget of the snowcover. This calculation is based on the same equations presented in the section discussing energy exchange at the snow surface. Net radiation is calculated by:

$$R_n = R_{n,sol} + I_{lw} - (\varepsilon_s \, \sigma \, T_{s,0}^4) \tag{96}$$

$R_{n,sol}$ and I_{lw} are inputs; $T_{s,0}$ begins at the initial input value and is then calculated and updated at the end of each time-step by the model. Surface emissivity ε_s is set at a constant value of 0.99 by the model.

Turbulent transfer terms, H and $L_v E$, are calculated by the method presented in the previous chapter:

$$H = \frac{(T_a - T_{s,0})\, a_h \, k \, u_* \rho \, C_p}{\ln\left[\dfrac{z_T - d_0}{z_0}\right] - \psi_{sh}\left[\dfrac{z_T}{L}\right]} \tag{97}$$

$$L_v E = \frac{(q - q_{s,0})\, a_v \, k \, u_* \rho}{\ln\left[\dfrac{z_q - d_0}{z_0}\right] - \psi_{sv}\left[\dfrac{z_q}{L}\right]} L_v \tag{98}$$

The measurement heights, z_T and z_u, are set as initial conditions and then updated by the model; z_q is assumed by the present configuration of the model to be equal to z_T. The roughness length z_0 is set as a model constant at the beginning of the run. Air temperature T_a, wind speed u, and vapor pressure e_a, are model inputs. Snow surface layer temperature $T_{s,0}$ is calculated by the model at the end of each time-step; snow surface vapor pressure is calculated as a function of $T_{s,0}$. Specific humidity of the air q and of the surface q_s is calculated from air pressure P_a and vapor pressure of the air e_a and the snow surface $e_{s,0}$.

Energy transfer by conduction and diffusion between the soil and the lower layer of the snowcover is calculated using the method discussed in the previous chapter:

$$G = \frac{2 K_{es,l} \, K_{eg} \, (T_g - T_{s,l})}{K_{eg} \, z_{s,l} + K_{es,l} \, z_g} \tag{99}$$

where:

$K_{es,l}$ = effective thermal conductivity of lower snow layer ($J\,m^{-1}\,K^{-1}\,s^{-1}$),
K_{eg} = effective thermal conductivity of soil layer ($J\,m^{-1}\,K^{-1}\,s^{-1}$).

The effective thermal conductivity of the lower snow layer $K_{es,l}$ and of the soil layer K_{eg} account for both conduction and diffusion of water vapor, and are functions of density, temperature, and air pressure. They are calculated using the method presented in the previous chapter. Soil temperature T_g and measurement depth z_g which define the temperature and thickness of the soil layer are model inputs.

Energy transfer by conduction and diffusion between the snow surface layer and the lower snow layer is calculated in the same manner:

$$G_0 = \frac{2 K_{es,0} K_{es,l} \, (T_{s,l} - T_{s,0})}{K_{es,l} \, z_{s,0} + K_{es,0} z_{s,l}} \tag{100}$$

where $K_{es,0}$ is the effective thermal conductivity of snow surface layer ($J\,m^{-1}\,K^{-1}\,s^{-1}$) This calculation allows the transfer of energy from the surface layer to the rest of the snowcover.

Advected energy transfer to the surface layer is calculated only during time-steps when precipitation input has occurred. Advection is calculated using the approach presented in the previous chapter:

$$M = \frac{C_{p\_p} \, \rho_{pp} \, z_{pp} \, [T_{pp} - T_{s,0}]}{t_{step}} \tag{101}$$

Advection is converted from a total ($J\,m^{-2}$), to an average flux ($W\,m^{-2}$) for the time-step, by dividing by the length of the time-step in seconds t_{step}. The density, depth, and temperature of precipitation are model inputs. The temperature of the snow surface layer $T_{s,0}$ is updated by the model at each time-step. The specific heat of precipitation C_{p_p} is calculated as a function of precipitation temperature T_{pp}, using the methods presented in the previous chapter. If the precipitation temperature is greater than T_{melt}, the model assumes that rain has occurred and the specific heat of water is used in the calculation of M. Otherwise the model uses the specific heat of ice.

The surface energy exchange terms are summed to determine the net energy transfer to the surface snow layer:

$$\Delta Q_0 = R_n + H + L_v E + G_0 + M \tag{102}$$

and the total energy transfer to the snowcover:

$$\Delta Q = \Delta Q_0 + G \tag{103}$$

These are used to determine the energy available for melting or re-freezing in each layer:

$$Q_0 = (\Delta Q_0 \, t_{step}) + cc_{s,0} \tag{104}$$

$$Q_l = ((G - G_0)\, t_{step}) + cc_{s,l} \tag{105}$$

The sign of an energy transfer term denotes whether it is toward (+) or away from (–) a layer. Therefore, if the transfer of energy during a model time-step is from the surface layer to the lower layer, the sign of G_0 would be negative, because it is a flux away from the surface layer.

If Q_0 or Q_l is positive, melt is calculated and the liquid water content of the snowcover w_S is adjusted:

$$q_{melt,0} = \frac{Q_0}{L_{f,melt}} \tag{106}$$

$$w_S = w_S + q_{melt,0} \tag{107}$$

$$q_{melt,l} = \frac{Q_l}{L_{f,melt}} \tag{108}$$

$$w_S = w_S + q_{melt,l} \tag{109}$$

where:

$q_{melt,0}$ = snow surface layer melt (kg m^{-2}),
$q_{melt,l}$ = lower snow layer melt (kg m^{-2}),
$L_{f,melt}$ = latent heat of fusion at T_{melt} (3.336x10^5 J kg^{-1}).

The layer cold contents $cc_{s,0}$ or $cc_{s,l}$ are set to 0.0, and they become the adjusted $cc_{s,0}$ or cc_s.

If Q_0 or Q_l is negative, and liquid water is present, the energy required for re-freezing is calculated:

$$Q_{0,z} = L_{f,melt} \left[\frac{w_S}{z_S} z_{s,0} \right] \tag{110}$$

$$Q_{l,z} = L_{f,melt} \left[\frac{w_S}{z_S} z_{s,l} \right] \tag{111}$$

If the sum $[Q_0 + Q_{0,z}]$ or $[Q_l + Q_{l,z}]$ is negative:

$$w_S = w_S - \left[\frac{w_S}{z_S} z_{s,0} \right] \tag{112}$$

$$cc_{s,0} = Q_0 + Q_{0,z} \tag{113}$$

$$w_S = w_S - \left[\frac{w_S}{z_S} z_{s,l} \right] \tag{114}$$

$$cc_{s,l} = Q_0 + Q_{l,z} \tag{115}$$

If these sums equal 0.0 the same adjustment is made to the snowcover liquid water content, but $cc_{s,0}$ and $cc_{s,l}$ are set to 0.0. If the sums are positive liquid water content w_S is adjusted by:

$$w_S = w_S - \left[\frac{w_S}{z_S} z_{s,0} \right] - \frac{Q_0 + Q_{0,z}}{L_{f,melt}} \tag{116}$$

$$w_S = w_S - \left[\frac{w_S}{z_S} z_{s,l} \right] - \frac{Q_l + Q_{l,z}}{L_{f,melt}} \tag{117}$$

and layer cold contents $cc_{s,0}$ and $cc_{s,l}$ are also set to 0.0.

If melt occurs during a time-step the total thickness of the snowcover z_S and the thickness of the lower snow layer $z_{s,l}$ will be reduced:

$$q_{melt} = q_{melt,0} + q_{melt,l} \tag{118}$$

$$z_S = z_S - \frac{q_{melt}}{\rho_S} \tag{119}$$

$$z_{s,l} = z_S - z_{s,0} \tag{120}$$

Because no runoff has yet been predicted the specific mass of the entire snowcover has not changed. However average snowcover density is increased, and the specific masses of the snow surface and lower layers and the cold content of the entire snowcover adjusted:

$$\rho_S = \frac{m_S}{z_S} \tag{121}$$

$$m_{s,0} = \rho_S\, z_{s,0} \tag{122}$$

$$m_{s,l} = \rho_S\, z_{s,l} \tag{123}$$

$$cc_S = cc_{s,0} + cc_{s,l} \tag{124}$$

Evaporation or condensation between the snow surface layer and the atmosphere E was determined during the calculation of latent heat flux $L_v E$. Evaporation or condensation between the lower snow layer and the soil is calculated:

$$E_l = \rho D_e \left[\frac{q_g - q_{s,l}}{z_g} \right] \tag{125}$$

where:

E_l = evaporative flux between soil and lower layer (kg m^{-2} s^{-1}),
q_g, $q_{s,l}$ = specific humidity of soil and lower snow layer

Total mass of evaporative loss or gain is:

$$E_S = (E + E_l)\, t_{step} \tag{126}$$

where E_S is the evaporative loss or gain from snowcover (kg m^{-2}). If liquid water is present, it is preferentially evaporated in the model by the ratio of the latent heat of vaporization to sublimation (0.882). The snowcover liquid water content w_S after adjustment for melt or re-freezing, is set equal to $w_{S,old}$ and then adjusted for evaporation:

$$w_S = w_{S,old} + 0.882 E_S \tag{127}$$

The remaining evaporative loss, or all evaporation after liquid water has been depleted, is modeled as sublimated ice. This decreases total snowcover depth z_S and causes adjustment of average snowcover density and the snow layer specific masses:

$$z_S = z_S + 0.5 \left[\frac{E_S + (w_{S,old} - w_S)}{\rho_S} \right] \tag{128}$$

$$m_S = m_S + E_S \tag{129}$$

$$z_{s,l} = z_S - z_{s,0} \tag{130}$$

$$\rho_S = \frac{m_S}{z_S} \tag{131}$$

$$m_{s,0} = \rho_S\, z_{s,0} \tag{132}$$

$$m_{s,l} = \rho_S\, z_{s,l} \tag{133}$$

Half of the ice lost is assumed to be decreased depth. The remaining sublimated ice and all evaporated liquid water decrease the density and mass of the snowcover.

The remaining liquid water content, after all snowcover depth, density, and mass adjustments for melt, re-freezing, and evaporation or condensation, is checked to see if w_c is greater than the threshold retention proportion of the air fraction of the snowcover $w_{c,sat}$:

$$V_s = z_S \tag{134}$$

$$V_i = \frac{m_S - w_S}{\rho_{ice}} \tag{135}$$

$$V_a = V_s - V_i \tag{136}$$

TABLE 10.3. Output from Snowmelt Model

Energy Fluxes:	One output record is produced for every input record.
R_n	Net all-wave radiation ($W\,m^{-2}$).
H	Sensible heat transfer ($W\,m^{-2}$).
$L_v E$	Latent heat transfer ($W\,m^{-2}$).
G	Heat transfer by conduction and diffusion between the snow and soil ($W\,m^{-2}$).
M	Heat transfer by advection ($W\,m^{-2}$).
ΔQ	Sum of energy flux terms ($W\,m^{-2}$).
Mass Fluxes:	One output record is produced for every input record.
E	Evaporation/sublimation, or condensation ($kg\,m^{-2}$).
q_{melt}	Predicted snowmelt ($kg\,m^{-2}$).
q_{out}	Predicted runoff ($kg\,m^{-2}$).
$[q_{out,err}]$	Runoff error $q_{out} - q_{out,meas}$ ($kg\,m^{-2}$). (Output of this parameter occurs only if optional measured runoff $q_{out,meas}$ is included with the input data.)
Snow Properties:	One output record is produced for every input record.
cc_S	Cold content, or energy required to bring entire snow cover to T_{melt} ($J\,m^{-2}$).
z_S	Predicted total snowcover depth (m).
ρ_S	Predicted average density for the entire snowcover ($kg\,m^{-3}$).
m_S	Predicted specific mass for the entire snowcover ($kg\,m^{-2}$).
w_S	Predicted total liquid water content for the entire snowcover ($kg\,m^{-2}$).
$T_{s,0}$	Predicted average snow surface layer temperature (K).
$T_{s,l}$	Predicted average snow lower layer temperature (K).
T_S	Predicted average temperature for the entire snowcover (K).
Model Error:	Difference between predicted and measured snow property parameters at the time of snow properties update. Output record is produced only if snow properties update data are available.
$t_{s,start}$	Time of snow properties update, relative to start of model run (decimal hours).
$z_{S,err}$	Error in predicted total snow depth $z_S - z_{S,meas}$.
$\rho_{S,err}$	Error in predicted average density of the entire snowcover $\rho_S - \rho_{S,meas}$.
$m_{S,err}$	Error in predicted specific mass of the entire snowcover $m_S - m_{S,meas}$.
$w_{S,err}$	Error in predicted total liquid water content for the entire snowcover $w_S - w_{S,meas}$.
$T_{s,0,err}$	Error in predicted average snow surface layer temperature $T_{s,0} - T_{s,0,meas}$.
$T_{s,l,err}$	Error in predicted average snow lower layer temperature $T_{s,l} - T_{s,l,meas}$.
$T_{S,err}$	Error in predicted average temperature for the entire snowcover $T_S - T_{S,meas}$.

TABLE 10.4. Average Snowcover Characteristics
Emerald Lake Watershed Study, 1985-86 Snow Season

Date	z_S (m)	ρ_S (kg m^{-3})	SWE (m)	$T_{s,0}$ (°C)	T_S (°C)	w_c
Ridge Site						
86/01/17	1.98	411	0.814	-0.3	-1.4	0.0
86/02/04	2.45	365	0.895	-8.9	-3.3	0.0
86/04/13	6.00	548	3.290	-0.1	-0.1	0.0
86/05/06	5.90	520	3.170	0.0	-0.07	0.3
86/05/23	4.65	572	2.660	0.0	0.0	0.8
86/06/27	2.50	578	1.440	0.0	0.0	1.0
Lake Site						
86/01/18	1.65	461	0.761	-1.9	-2.1	0.0
86/02/06	2.30	365	0.839	-6.2	-6.1	0.0
86/03/05	3.20	461	1.476	-0.2	-1.0	0.0
86/05/02	4.05	593	2.400	0.0	0.0	0.4
86/05/21	3.57	554	1.980	0.0	0.0	0.9
86/06/27	2.03	590	1.200	0.0	0.0	1.0

TABLE 10.5. Snowmelt Model Test Run
Emerald Lake Watershed, 1986 Snow Season
Run: 86/04/14 - 86/05/06 (524 hrs)

Average Energy Flux (W m^{-2}):

Process	Flux
R_n	7.33
H	171.94
$L_v E$	-169.97
$H + L_v E$	1.66
G	0.30
M	0.09
ΔQ	12.69

Calculated Mass Flux (kg m^{-2}):

Process	Flux
$[\rho_{pp} \times z_{pp}]$	56.0
E_S	-116.6
E_l	1.1
q_{out}	0.0
Total	-59.5

Snowmelt Model Result:

Parm	Units	Start	End	Measured	Error
z_S	m	6.00	5.83	5.90	0.08
m_S	kg m^{-2}	3288.0	3229.0	3186.0	43.0
ρ_S	kg m^{-3}	548.0	554.0	540.0	14.0
w_S	kg m^{-2}	0.0	0.8	---	---
$T_{s,0}$	K	273.15	270.9	273.15	-2.25
$T_{s,l}$	K	273.05	273.10	273.08	0.02
T_S	K	273.05	273.10	273.08	0.02

$$w_{max} = V_a \; w_{c,sat} \; \rho_{w,melt} \tag{137}$$

where:

ρ_{ice} = density of ice, no air (917 kg m^{-3}),
$\rho_{w,melt}$ = density of water at 0.0 C (999.87 kg m^{-3}),
w_{max} = maximum water retention (kg m^{-2}),
V_a = volume air fraction of snowcover (m^3 m^{-2}).

The above equations are dimensionally correct because each of the above volume terms is a specific volume with units of meters.

If w_S is greater than w_{max} runoff is predicted and both the density, ρ_S, and specific masses $m_{s,0}$, $m_{s,l}$, and m_S are appropriately reduced:

$$q_{out} = w_S - w_{max} \tag{138}$$

$$m_S = m_S - q_{out} \tag{139}$$

$$\rho_S = \frac{m_S}{z_S} \tag{140}$$

$$m_{s,0} = z_{s,0} \, \rho_S \tag{141}$$

$$m_{s,l} = z_{s,l} \, \rho_S \tag{142}$$

$$w_S = w_{max} \tag{143}$$

If the snowcover cold content cc_S is equal to 0.0 the temperatures of both layers and the snowcover are set to T_{melt}. If not the snow layer temperatures are adjusted:

$$T_{s,0} = \frac{cc_{s,0}}{m_{s,0} \, C_{p\_ice,0}} + T_{melt} \tag{144}$$

$$T_{s,l} = \frac{cc_{s,l}}{m_{s,l} \, C_{p\_ice,l}} + T_{melt} \tag{145}$$

$$T_S = \frac{cc_S}{m_S \, C_{p\_ice,S}} + T_{melt} \tag{146}$$

Snowmelt Model Output

Table 10.3 below presents detailed description of the output from the snowmelt model. An output record is written for each input record. Runoff error is output only if measured runoff from the snowcover is included in the model inputs. Total snowcover cold content, depth, and specific mass are the sum of their layer values.

Multiple inputs of snowcover properties, measurement heights, and precipitation properties can be made. If additional inputs on snowcover properties or measurement heights are made, the model will calculate the difference or error between modeled and update parameters, and then update all affected parameters. In practice, however, it is unlikely that frequent update data will be available.

If update data for snowcover properties or measurement heights were input, the error for snowcover depth, density, specific mass, surface and layer temperatures, liquid water content, and measurement heights are written to an error file.

10.2. Preliminary Test of the Snowmelt Model

Ultimately, the snowmelt model presented here will lead to a model that will predict the magnitude, timing, and location of the generation of snowmelt runoff over a watershed. The model presented here is designed to improve our understanding of the interaction of energy transfer and snowmelt processes. As presented, the model is relatively simple, both in concept and in structure. It is easy to run and to modify, so that variations on the inputs and modeling assumptions can be evaluated. The methods used to calculate energy flux from measurements of meteorological and surface parameters are designed to give reliable results from data which is commonly available. The sensitivity of snowmelt calculations to errors and uncertainties in these inputs must be tested.

The simplifying assumptions about the internal heat and mass transfer processes within the snowcover have not been adequately tested. The snowmelt model will help with this process by allowing repeated calculations using a variety of inputs and different assumptions about the condition and response of the snowcover to energy flux.

The model is difficult to verify using the 1986 snowcover data. Data collection was done before the input requirements of the model were completely defined. A decision to sample more sites less frequently improved the understanding of the spatial distribution of the snowcover, but it made model verification less effective. Detailed information on snow depth, density, temperature, and liquid water content were measured or estimated repeatedly only six times during the 1986 snow season at the ridge and lake sites. This offered five time periods during which there would be an initial and a final measurement of snowcover properties. Unfortunately, these are fairly long time periods that leave uncertainty about changes to the snowcover that may have occurred between measurements. Table 10.4 presents measured snowcover conditions for both sites. Because of the input of significant precipitation during winter and early spring, it was appropriate to test the snowmelt model only during the last three intervals at the ridge site and the last two intervals at the lake site. These periods begin just prior to snowmelt at the ridge site and early in the snowmelt season at the lake site. Snow temperatures are uniform and close to isothermal, and densities are high, and do not change appreciably during the test period, though considerable mass is lost indicating melting conditions. The last column in the table presents an estimate of the liquid water saturation of the snowcover. In this representation a value of 1.0 would be equivalent to the liquid water retention threshold.

Few measurements of liquid water content in the snowcover were made during the 1986 snow season, and no estimate of the average value for snowcover was made. Initial runs of the snowmelt model indicate that it is sensitive to the magnitude of the maximum threshold set, which is used by the model to predict runoff. Indications are that the lower the threshold, the more realistic the runoff predictions. It would appear that the snowcover had a very low water retention threshold (<0.005), and was essentially saturated from mid-March on.

The large magnitude of the snowcover also presents a problem for verification of the model. It is estimated that density determinations are accurate to around 5–10%. Thus from the table above, a density of $593\,kg\,m^{-3}$ is not really that different from $554\,kg\,m^{-3}$. Yet the fact that the measurement indicates that the density decreased during the time period, has a marked effect on the relationship between measured and predicted mass loss, for a model run during this period.

The model was run successfully for the period between 86/04/13 and 86/05/06 at the ridge site primarily because this was prior to active melt, and there was little liquid water present. Though the results from this test are good, it does not mean that the model is without problems. This run of the model was made during a time when liquid water was minimal, and during which significant melt did not occur. Under these conditions, the model shows that the input data and the techniques for calculation of energy transfer are reliable. The calculation of mass flux within the snowcover and runoff from the snowcover are not tested by this run. The differences between calculated and measured parameters at the end of the model run are well within measurement accuracy, and are not significant. Liquid water content was not measured, so the model error is unknown. Table 10.5 presents the results of this run.

10.3. References

Aguado, E., Radiation balances of melting snow covers at an open site in the central Sierra Nevada, California, *Water Resour. Res., 21*, 1649-1654, 1985.

Anderson, E. A., Development and testing of snow pack energy balance equations, *Water Resour. Res., 4*, 19-37, 1968.

Anderson, E. A., A point energy and mass balance model of a snow cover, *NWS Tech. Rep. 19*, 150 pp., NOAA, Washington, DC, 1976.

Anderson, E. A., Streamflow simulation models for use on snow covered watersheds, in *Proc. Modeling Snow Cover Runoff*, edited by S. C. Colbeck and M. Ray, pp. 336-351, U.S. Army Cold Regions Res. Engrg. Lab., Hanover, NH, 1979.

Anderson, E. A. and N. Crawford, The synthesis of continuous snowmelt runoff hydrographs on a digital computer, *Tech. Rep. 36*, 103 pp., Dept. Civil Engrg., Stanford Univ., Stanford, CA, 1964.

Arnfield, A. J., Estimation of diffuse irradiance on sloping, obstructed surfaces: an error analysis, *Arch. Meteorol. Geophys. Bioklim., Ser. B, 30*, 303-320, 1982.

Bernard, M. and W. T. Wilson, A new technique for the determination of heat necessary to melt snow, *Eos, Trans. Amer. Geophys. Union, 22*, 178-181, 1941.

Braithwaite, R. J., On glacier energy balance, ablation, and air temperature, *J. Glaciol., 27*, 381-391, 1981.

Choudhury, B. J., C. S. Cheng, and A. T. C. Chang, Numerical simulation of the thermal structure of snow packs using an energy balance model: model description and parameter test, *Tech. Mem. 82044*, 30 pp., NASA Goddard Space Flight Ctr., Greenbelt, MD, 1980.

Colbeck, S. C., A theory of water percolation in snow, *J. Glaciol., 11*, 369-385, 1972.

Colbeck, S. C., Water flow through snow overlying an impermeable boundary, *Water Resour. Res., 10*, 119-123, 1974.

Colbeck, S. C., The capillary effects on water percolation in homogeneous snow, *J. Glaciol., 13*, 85-97, 1974.

Colbeck, S. C., A theory for water flow through a layered snowpack, *Water Resour. Res., 11*, 261-266, 1975.

Colbeck, S. C., Thermodynamic deformation of wet snow, *Rep. 76-44*, 9 pp., U.S. Army Cold Regions Res. Engrg. Lab., Hanover, NH, 1976.

Colbeck, S. C., Short-term forecasting of water run-off from snow and ice, *J. Glaciol., 19*, 571-588, 1977.

Colbeck, S. C., The compression of wet snow, *Rep. 78-10*, 23 pp., U.S. Army Cold Regions Res. Engrg. Lab., Hanover, NH, 1978.

Colbeck, S. C., The difficulties of measuring the water saturation and porosity of snow, *J. Glaciol., 20*, 189-201, 1978.

Colbeck, S. C., The physical aspects of water flow through snow, in *Advances in Hydroscience*, edited by V. T. Chow, vol. 11, pp. 165-206, Academic Press, New York, 1978.

Colbeck, S. C., On the use of tensiometers in snow hydrology, *J. Glaciol., 17*, 135-140, 1979.

Colbeck, S. C., Water flow through heterogeneous snow, *Cold Regions Sci. Technol., 1*, 37-45, 1979.

Colbeck, S. C. and E. A. Anderson, Permeability of a melting snow cover, *Water Resour. Res., 18*, 904-908, 1982.

Davies, J. A. and S. B. Idso, Estimating the surface radiation balance and its components, in *Modification of the Aerial Environments of Plants*, edited by J. F. Gerber and B. J. Barfield, ASAE Monogr. 2, pp. 183-210, 1979.

Davis, R. E., J. Dozier, E. R. LaChapelle, and R. Perla, Field and laboratory measurements of snow liquid water by dilution, *Water Resour. Res., 21*, 1415-1420, 1985.

Dozier, J., A clear-sky spectral solar radiation model for snow-covered mountainous terrain, *Water Resour. Res., 16*, 709-718, 1980.

Dozier, J. and D. Marks, Snow mapping and classification from Landsat Thematic Mapper data, *Ann. Glaciol., 9*, 97-103, 1987.

Dozier, J. and S. I. Outcalt, An approach toward energy balance simulation over rugged terrain, *Geogr. Anal., 11*, 65-85, 1979.

Dunne, T. and R. D. Black, Runoff processes during snowmelt, *Water Resour. Res., 7*, 1160-1172, 1971.

Dunne, T., A. G. Price, and S. C. Colbeck, The generation of runoff from subarctic snowpacks, *Water Resour. Res., 12*, 677-685, 1976.

Föhn, P. M., Short-term snowmelt and ablation derived from heat- and mass-balance measurements, *J. Glaciol., 12*, 275-289, 1973.

Granger, R. J. and D. H. Male, Melting of a prairie snowpack, *J. Appl. Meteorol., 17*, 1833-1842, 1978.

Harstveit, K., Measuring and modelling snowmelt in Dyrdalen, Western Norway, 1979 and 1980, *Nordic Hydrol., 12*, 235-246, 1981.

Hendrie, L. K. and A. G. Price, Energy balance and snowmelt in a deciduous forest, in *Proc. Modeling Snow Cover Runoff*, edited by S. C. Colbeck and M. Ray, pp. 211-221, U.S. Army Cold Regions Res. Engrg. Lab., Hanover, NH, 1979.

Kuhn, M., On the computation of heat transfer coefficients from energy-balance gradients on a glacier, *J. Glaciol., 22*, 263-272, 1979.

Kuusisto, E., Temperature index, energy balance - or something else?, in *Symposium on the Use of Hydrological Research Basins in Planning*, vol. 1, p. 9, Sonderheft Landeshydrologie, Bern, 1982.

La Casinière, A. C. de, Heat exchange over a melting snow surface, *J. Glaciol., 13*, 55-72, 1974.

Male, D. H. and R. J. Granger, Energy and mass fluxes at the snow surface in a prairie environment, in *Proc. Modeling Snow Cover Runoff*, edited by S. C. Colbeck and M. Ray, pp. 101-125, U.S. Army Cold Regions Res. Engrg. Lab., Hanover, NH, 1979.

Male, D. H. and R. J. Granger, Snow surface energy exchange, *Water Resour. Res.*, *17*, 609-627, 1981.

Male, D. H. and D. M. Gray, Problems in developing a physically based snowmelt model, *Can. J. Civil Engrg.*, *2*, 474-488, 1975.

Marks, D. and J. Dozier, A clear-sky longwave radiation model for remote alpine areas, *Arch. Meteorol. Geophys. Bioklim.*, *Ser. B*, *27*, 159-187, 1979.

Marks, D., R. Kattelmann, J. Dozier, and R. E. Davis, Monitoring snowcover properties and processes in a small alpine watershed, in *Proceedings of Sixth International Northern Research Basins Symposium/Workshop*, edited by H. S. Santeford, pp. 259-275, Mich. Technol. Univ., Houghton, MI, 1986.

McKay, D. C. and G. W. Thurtell, Measurements of the energy fluxes involved in the energy budget of a snow cover, *J. Appl. Meteorol.*, *17*, 339-349, 1978.

Morris, E. M., Sensitivity of the European Hydrological System snow models, in *Hydrological Aspects of Alpine and High-Mountain Areas*, edited by J. W. Glen, IAHS-AIHS Publ. 138, pp. 221-231, Intl. Assoc. Hydrol. Sci., Wallingford, UK, 1982.

Morris, E. M., Modelling of a seasonal snowcover, in *Snow Watch '85*, edited by G. Kukla, R. G. Barry, A. Hecht, and D. Wiesnet, Glaciol. Data report GD-18, pp. 225-240, World Data Ctr. Glaciol., Boulder, CO, 1986.

Munroe, D. S. and G. J. Young, An operational net shortwave radiation model for glacier basins, *Water Resour. Res.*, *18*, 220-230, 1982.

Obled, Ch. and H. Harder, A review of snow melt in the mountain environment, in *Proc. Modeling Snow Cover Runoff*, edited by S. C. Colbeck and M. Ray, pp. 179-204, U.S. Army Cold Regions Res. Engrg. Lab., Hanover, NH, 1979.

Obled, Ch. and B. Rosse, Mathematical models of a melting snowpack at an index plot, *J. Hydrol.*, *32*, 139-163, 1977.

Olyphant, G. A., Insolation topoclimates and potential ablation in alpine snow accumulation basins: Front Range, Colorado, *Water Resour. Res.*, *20*, 491-498, 1984.

Olyphant, G. A., Longwave radiation in mountainous areas and its influence on the energy balance of alpine snowfields, *Water Resour. Res.*, *22*, 62-66, 1986.

Olyphant, G. A., The components of incoming radiation within a mid-latitude alpine watershed during the snowmelt season, *Arctic Alpine Res.*, *18*, 163-169, 1986.

Outcalt, S. I., The development and application of a simple digital surface-climate simulator, *J. Appl. Meteorol.*, *11*, 629-636, 1972.

Price, A. G. and T. Dunne, Energy balance computations of snowmelt in a subarctic area, *Water Resour. Res.*, *12*, 686-694, 1976.

Pysklywec, D. W., K. S. Davar, and D. I. Bray, Snowmelt at an index plot, *Water Resour. Res.*, *4*, 937-946, 1968.

Siegel, R. and J. R. Howell, *Thermal Radiation Heat Transfer*, 2nd ed., 862 pp., McGraw-Hill, New York, 1981.

U.S. Army Corps of Engineers, *Snow Hydrology*, Rep. PB-151660, 437 pp., USACE, Portland, OR, 1956.

Wilson, W. T., Some factors relating the melting of snow to its causes, *Proc. Central Snow Conf.*, *1*, 33-41, 1941.

Wilson, W. T., An outline of the thermodynamics of snow-melt, *Eos, Trans. Amer. Geophys. Union*, *22*, 182-195, 1941.

Woo, M. and H. O. Slaymaker, Alpine streamflow response to variable snowpack thickness and extent, *Geogr. Annaler, Ser. A*, *57A*, 201-212, 1975.

Zuzel, J. F. and L. M. Cox, Relative importance of meteorological variables in snowmelt, *Water Resour. Res.*, *11*, 174-176, 1975.

TABLE 10.2. Snowmelt Model Input Requirements

Run Constants:	Values held constant for model run.
z_{el}	Site elevation (m).
t_{step}	Model run time-step (decimal hours).
$w_{c,sat}$	Threshold maximum liquid water content as a proportion of the air fraction of the snowcover (dimensionless). Suggested value $w_{c,sat} = 0.01$ or less.
$z_{s,0}$	Thickness of the snow surface layer (m). Suggested value $z_{s,0} = 0.25$ m.
z_0	Surface roughness length (m). Suggested value z_0 between 0.005 and 0.0001 m.
z_g	Soil Temperature measurement depth below soil surface (m). Suggested value $z_g = 0.5$ m.
Precipitation:	**Repeat input as needed during model run.**
$t_{pp,start}$	Time of precipitation, relative to start time of model run (decimal hours).
z_{pp}	Depth of precipitation (m).
ρ_{pp}	Precipitation density (kg m^{-3}). Rain should have a density of 1000 kg m^{-3}.
T_{pp}	Precipitation temperature (K). Used to separate rain from snow. T_{pp} for rain must be greater than T_{melt}.
Snow Properties:	**Adjusted at the end of each model time-step. First input defines initial conditions for model run. Can be updated.**
$t_{s,start}$	Time of snow properties update, relative to start time of model run (decimal hours). The initial input of $t_{s,start}$ is the start time of the model run.
z_S	Total snowcover depth as a height above the ground (m).
ρ_S	Average density for the entire snowcover (kg m^{-3}).
$T_{s,0}$	Average temperature of the snow surface layer (K).
T_S	Average temperature for the entire snowcover (K).
w_c	Average liquid water content for the entire snowcover as a proportion of the air fraction of the snowcover (dimensionless). Must be less than or equal to $w_{c,sat}$.
Measurement Hts:	**Adjusted for changes in z_S at end of each model time-step. First input defines initial conditions for model run. Can be updated.**
$t_{z,start}$	Time of measurement height update, relative to start time of model run (decimal hours). The initial input of $t_{z,start}$ must be equal to the initial input value of $t_{s,start}$.
z_u	Wind speed measurement height above snow surface (m). Can be equal to z_T.
z_T	Air temperature and humidity measurement height above snow surface (m). Can be equal to z_u.
Input Data:	**Required for each time-step of model run.**
$R_{n,sol}$	Net solar radiation (W m^{-2}).
I_{lw}	Incident thermal radiation (W m^{-2}).
T_a	Air temperature measured at z_T (K).
e_a	Vapor pressure measured at z_T (Pa).
u	Wind speed measured at z_u (m s^{-1}).
T_g	Soil temperature measured at z_g (K).
$[q_{out,meas}]$	Runoff measured from the bottom of the snowcover (kg s^{-1} or m^{-2} s^{-1}). This input is optional.